Title
Modeling and analysis of thin-film incline flow: bidensity suspensions and surface tension effects

Author
Wong, Jeffrey Taylor

Publication Date
2017

Peer reviewed|Thesis/dissertation

UNIVERSITY OF CALIFORNIA
Los Angeles

Modeling and analysis of thin-film incline flow: bidensity suspensions and surface tension effects

A dissertation submitted in partial satisfaction
of the requirements for the degree
Doctor of Philosophy in Mathematics

by

Jeffrey Wong

2017

ABSTRACT OF THE DISSERTATION

Modeling and analysis of thin-film incline flow:
bidensity suspensions and surface tension effects

by

Jeffrey Wong
Doctor of Philosophy in Mathematics
University of California, Los Angeles, 2017
Professor Andrea Bertozzi, Chair

For flow of suspensions down an incline, particles are driven by shear-induced migration towards the surface, leading to separation of particle and fluid phases or aggregation at the leading edge. Reduced models are interesting from a mathematical standpoint as they take the form of PDEs for the evolution of the fluid and particle phases of hyperbolic/parabolic type. By assuming a separation of time scales, one can reduce the model to two simpler components: an equilibrium equation for the particle distribution and a set of one-dimensional PDEs for the evolution of the film. This approach is used here explore several more complicated problems concerning gravity-driven flow on an incline. We study bidensity suspensions (i.e. with two particle species of different densities) and develop the corresponding equilibrium and dynamic theory. A system of hyperbolic conservation laws are derived and shock and rarefaction solutions are constructed to describe the separation of particle and fluid phases. Surface tension is also introduced into the model, which can lead to unusual behavior by allowing particles to aggregate to interior points in the fluid. We derive the thin-film system for the evolution of the fronts, develop a numerical method to handle the complicated fluxes and study solutions through simulations.

The dissertation of Jeffrey Wong is approved.

Michael K. Stenstrom

Joseph M. Teran

Marcus L. Roper

Andrea Bertozzi, Committee Chair

University of California, Los Angeles

2017

Table of Contents

List of Figures

Acknowledgments

Foremost, I am indebted to my advisor, whose guidance has been instrumental in the success my graduate studies and who always provided the right balance of challenge and encouragement. I am fortunate to have had the chance to work with many collaborators and mentors over the years. I would like to thank Sungyon Lee for sparking an interest in particle-laden flows, and for giving me the chance to become involved in this research to begin with. Marcus Roper, Li Wang, Aliki Mavromoustaki and Dirk Peschka offered valuable guidance and helped me to understand the subject and shape the research that would become this dissertation. I am grateful for the support of David Arnold, Claudia Falcon and Michael Lindstrom, who were a part of countless illuminating discussions that have provided new perspectives on this research and gave helpful suggestions on the dissertation.

Chapter 1 is a summary of background on suspension flow on an incline, primarily from the paper [MPP13]. Chapter 2 is original work. Chapter 3 is adapted from a manuscript submitted for publication [MWW16]. My contributions are the derivation of the model including diffusion from the normal component of gravity and the equilibrium theory. The original model in Section 3.1.1 was proposed by Aliki Mavromoustaki and Section 3.3 on the numerical method and Section 3.4 on simulations was written by Li Wang and is included for completeness; the simulations, comparison to experiments and discussion were a collaboration with Li Wang. Chapter 4 is a version of the published work [LWB15], my contribution to which is the equilibrium theory in Section 4.2 for bidensity suspensions. The bidensity model described in Section 4.1 was developed by Sungyon Lee. Chapter 5 is a version of the published work [WB16], in which I am first author.

This work was completed under the UCLA Dissertation Year Fellowship and was partially supported by National Science Foundation grants DMS-1312543 and DMS-1045536.

Vita

2011	B.S. (Mathematics), Harvey Mudd College.
2012-2013	Research Assistant, Mathematics Department, UCLA
2013-2016	Teaching Assistant, Mathematics Department, UCLA
2016-2017	Dissertation Year Fellowship, Mathematics Department, UCLA
June 2017	Ph.D. (Mathematics) expected, UCLA

Publications

Lee, Sungyon, Jeffrey T. Wong and Andrea L. Bertozzi. *Equilibrium theory of bidensity particle laden flows on an incline.* Mathematical Modeling and Numerical Simulation of Oil Pollution Problems, The Reacting Atmosphere Vol. 2, pp. 85-97, Mattias Ehrhardt, Ed., 2015.

Jeffrey T. Wong and Andrea L. Bertozzi, *A conservation law model for bidensity suspensions on an incline.* Physica D: Nonlinear Phenomena 330 (2016): 47-57.

Mavromoustaki, Aliki, Li Wang, Jeffrey T. Wong and Andrea L. Bertozzi. *Modeling and simulation of particle-laden flow with surface tension.* Submitted to Nonlinearity, Mar. 2016. Available at `ftp://ftp.math.ucla.edu/pub/camreport/cam15-71.pdf`

CHAPTER 1

Introduction

1.1 Viscous suspensions in shear

The dynamics of suspension flows have been the subject of extensive research. They exhibit a wide variety of fascinating phenomena, including separation of particle and fluid phases through sedimentation or re-entrainment. Understanding of suspensions is key to many industrial applications and physical problems - for example, modeling of geophysical phenomena [Fow90], blood flow [KG12] and in the design of separators for particle segregation [ASG17]. Because of the complexity of the particle and fluid interactions, suspensions are challenging to model. Simulating the individual particles in a particle-quickly becomes intractable, so it is desirable to find simpler continuum models that can capture key effects.

In particular, this continuum approach has be utilized to model viscous suspensions under shear. A primary feature of interest for such flows is shear induced migration, in which particle interactions give rise to migration behavior that causes particles to migrate towards areas of lower concentration or shear rate. The mechanism for this effect has been the subject of significant attention since the fundamental work of Leighton and Acrivos [LA87], who proposed a model (the 'diffusive flux model') that describes the migration as the result of particles colliding in the shear flow and being deflected from their streamlines. The model has been used to study shear-induced migration in simple geometries, such as in channel or Couette flow [PAB92].

The diffusive flux model, however, is of limited use outside of these geometries, as it makes considerable assumptions about the nature of the particle collisions and the shear

profile of the flow. The suspension balance model, proposed originally by Nott and Brady [NB94], proceeds by averaging the fluid and particle phases in a more general framework, overcoming some limitations of its predecessor. In simple geometries, the model reduces to one of comparable simplicity to the diffusive flux model, which has been employed in many studies of particle migration in suspension flow [MB99, MM06]. This has led to a better understanding of the rheology of dense suspensions [BPG11] and the correct mechanism for shear-induced migration [NGP11], and the approach remains a useful tool (for example, studying flow instabilities in a Hele-Shaw a cell [XKL16]).

Thin film and incline flow

Applications of these suspension models have primarily focused on steady-flow problems. Relatively little work has been done on the dynamics of moving fronts and free-surface problems. The dynamics of viscous thin films are well-studied with a rich mathematical theory and diverse behavior in a broad range of problems [CM09]. One prototypical problem for driven thin films is the flow of a viscous sheet down an incline (driven by gravity). The experiments of Zhou et. al. [ZDB05] drew attention to this incline problem for suspensions with negatively buoyant particles, for which one would expect the particles to settle to the substrate. They conducted an experiment in which a fixed volume of a uniformly mixed suspension was released down an incline and observed two distinct regimes (shown in Figure 1.1): up to a certain critical concentration ϕ_c, the particles and fluid separated into distinct fronts (with the fluid ahead of the particles), while above this concentration, the particles accumulated at a single particle-rich front (referred to hereafter as the 'settled' and 'ridged' regimes).

The observed bifurcation spurred the development of a lubrication model extending the classical thin film theory to account for migration of particles in the normal direction. This model yields a pair of hyperbolic conservation laws for the film height and particle concentration with shock solutions corresponding to the fronts. Cook et. al. [Coo08] studied such a model with the assumption that the particles are uniform over the depth of the fluid

and studied shock and singular shock solutions for the Riemann problem. The migration of particles through the depth of the fluid was first introdued to the model by Cook [CBH08], who used the balance of shear-induced migration and sedimentation to explain the settled and ridged regimes by identifying a critical concentration ϕ_c above which suspensions will be ridged. Murisic et. al. [MHH11] further developed this 'equilibrium theory', conducted additional experiments and found excellent agreement of the predicted critical concentration.

For a constant volume of a suspension on an incline, Ward et. al. [WWG09] conducted experiments, contrasting the evolution of the moving front with the result of Huppert for a clear fluid [Hup82] that the position of leading edge should scale with $t^{1/3}$. To investigate these dynamics, Murisic et. al. [MPP13] proposed a model that accounts for the non-uniform distribution of particles through the fluid depth but reduces to depth-integrated conservation laws analogous to those in classical lubrication theory. To obtain such equations, the key condition is to have a separation of time scales in the normal (fast) and tangential (slow) directions, which turns out to be the asymptotic limit

$$\epsilon^{1/2} \ll d/H \ll 1 \tag{1.1}$$

where H is the characteristic height of the film, L is the length scale along the incline and $\epsilon = H/L$ is the lubrication parameter. In the lubrication limit, the Stokes equations then reduce to a pair of separate problems: an ODE system governing the rapid equilibration of particles in the normal direction and an evolution equation for the film height h and depth-averaged concentration of particles. Through this approach, Murisic et. al. [MPP13] predicted the evolution of the particle and fluid fronts in the parameter regime where the scaling assumption (1.1) holds (for mixtures roughly emulating typical oil/sand mixtures). The equations are a pair of hyperbolic conservation laws with an interesting mathematical structure. The Riemann problem was solved in [MB14] and singular shock solutions for high concentrations (a novel feature, as the non-classical singular shocks do not appear often in physical applications) were studied in depth for the Riemann problem [WB14]. At high concentrations, solutions to the constant volume problem are rarefaction-singular shock solutions, as shown by Wang et. al. [WMB15].

1.2 Scope of this work

The work Murisic et. al. provides a method to reduce models for thin-film suspension flow into tractable sets of equations. A variety of effects can be incorporated into the model, so long as their inclusion is compatible with the equilibrium assumption. Here we explore gravity-driven flow of suspensions on an incline with several additional effects, adapting the framework of the original model.

In Chapter 2, we employ the more recent suspension balance model to derive equations for incline flow analogous to the older model, comparing the results of the equilibrium theory in each case and demonstrating that the two models exhibit qualitative agreement. In Chapter 3, we develop a thin-film model for suspensions with surface tension, solve the equilibrium problem for particle migration and the coupled system of PDEs for the downstream flow. In Chapter 4, we propose a diffusive flux model for bidensity suspensions (with two negatively buoyant particle species of different densities) and study the equilibrium problem. In Chapter 5, the conservation law system governing the downstream flow for bidensity suspensions is explored in detail, including the construction of shock solutions for the Riemann problem and shock-rarefaction solutions for constant volume initial conditions. Additionally, we perform a detailed analysis of the long-time behavior for the simpler monodisperse problem.

1.3 Diffusive flux model for free-surface incline flow

Here we summarize the model from Murisic et. al. [MPP13], which serves as the basis for the extensions we study in later chapters. The setup for the problem is shown in Figure 1.1. Consider an inclined plane with inclination angle α, and a fluid with free surface $h(x,t)$ flowing down the incline. The coordinates are (x,z) with x aligned down the incline and z aligned normal to the incline. The fluid has viscosity μ_ℓ and the suspension consists of negatively buoyant particles with density $\rho_p > \rho_\ell$ and uniform diameter d. In Chapter 4, we

will consider the addition of a second particle species with a different density. Throughout, subscripts ℓ and p will refer to liquid and particle quantities and no subscript will indicate a suspension quantity. The scalings are

$$(x, z) = L(\hat{x}, \epsilon\hat{z}), \quad (u, w) = U(\hat{u}, \epsilon\hat{w}), \quad t = \frac{L}{U}\hat{t}, \quad p = P\hat{p}$$

where $H = \epsilon L$, $T = L/U$ and the characteristic x-velocity and pressure are

$$U = \frac{H^2 \rho_\ell g \sin\alpha}{\mu_\ell}, \qquad P = \frac{\mu U}{H}, \tag{1.2}$$

chosen to balance viscous forces in the x-momentum equation with gravity. It will be useful to define the scaled effective density

$$\hat{\rho}(\phi) = \rho(\phi)/\rho_\ell = 1 + \rho_s \phi, \qquad \rho_s := \frac{\rho_p - \rho_\ell}{\rho_\ell} \tag{1.3}$$

and scaled viscosity $\hat{\mu} = \mu/\mu_\ell$, which is given by the Krieger-Dougherty relation

$$\hat{\mu}(\phi) = \left(1 - \frac{\phi}{\phi_{\max}}\right)^{-2} \tag{1.4}$$

where $\phi_{\max} \approx 0.61$ is the maximum packing fraction.

The flow is assumed to be in the Stokes regime (the Reynolds number Re $\ll 1$) and the particles are assumed to be large enough that Brownian diffusion can be neglected (the Péclet number Pe $\gg 1$). We assume, of course, that $\epsilon \ll 1$ and moreover that the equilibrium scaling assumption (1.1) holds.

Denoting the particle concentration by ϕ, the suspension is modeled as a quasi-Newtonian fluid, satisfying the Navier-Stokes momentum equation

$$\frac{D\mathbf{u}}{Dt} = -\nabla p + 2\nabla \cdot (\mu \mathbf{E}) + \rho \mathbf{g} \tag{1.5}$$

where $\mathbf{g}$ is the gravity vector, $\mathbf{E} = (\nabla\mathbf{u} + \nabla\mathbf{u}^T)/2$ is the strain rate tensor for the suspension. Note that μ and ρ depend on the concentration ϕ according to (1.3) and (1.4). The particle transport equation is

$$\frac{\partial \phi}{\partial t} + \nabla \cdot (\phi \mathbf{u}) = -\nabla \cdot \mathbf{J}. \tag{1.6}$$

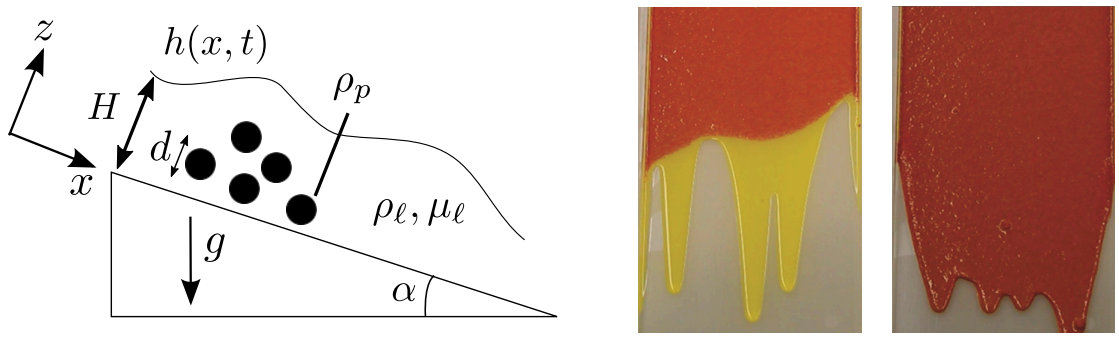

Figure 1.1: Left: schematic for the incline problem. Center/right: Experiments from [MLB14] showing the 'settled' regime where particles and fluid separate and 'ridged' regime where particles aggregate at a single moving front (an overhead view with red particles and yellow fluid).

where the particle flux $\mathbf{J}$ describes the motion of the particles relative to the fluid due to shear-induced migration and sedimentation, given by

$$\mathbf{J} = \underbrace{\phi f_h(\phi)\frac{d^2(\rho_p - \rho_\ell)}{18\mu_\ell}\mathbf{g}}_{\mathbf{J}_g} + \underbrace{a^2\phi\left(-K_c\nabla(\dot{\gamma}\phi) - K_v\dot{\gamma}\frac{\phi}{\mu}\nabla\mu\right)}_{\mathbf{J}_s} \tag{1.7}$$

Here $f_h(\phi) = \mu_\ell(1-\phi)/\mu(\phi)$ is the hindrance function, d is the particle radius, $K_c = 0.41$ and $K_v = 0.62$ are constants and $\dot{\gamma} = \sqrt{2\mathbf{E}:\mathbf{E}}$ is the shear rate. Because the particle phase moves relative to the fluid, the 'incompressibility' condition is (see [ASG17])

$$\nabla \cdot \mathbf{u} = -\nabla \cdot \mathbf{J}. \tag{1.8}$$

To leading order in the lubrication limit, this is the same as the incompressibility condition $\nabla \cdot \mathbf{u} = 0$ used in [MPP13]. Now define the depth-averaged concentration

$$\overline{\varphi}(x,t) = \frac{1}{h}\int_0^h \phi(x,z,t)\,\mathrm{d}z. \tag{1.9}$$

As derived by Murisic et. al. [MPP13], if (1.1) holds then there exist concentration and velocity profiles $\widetilde{\varphi}(s;\overline{\varphi})$ and $\widetilde{u}(s;\overline{\varphi})$ so that

$$\phi(x,z,t) = \widetilde{\varphi}(z/h;\overline{\varphi}), \qquad u(x,z,t) = h^2\widetilde{u}(z/h;\overline{\varphi}). \tag{1.10}$$

Under the asymptotic assumption (1.1), the particle transport equation to leading order is simply $J^{(z)} = 0$. This and the x-momentum equation (1.5) form a system of ODEs from which we can obtain the 'equilibrium solution' (1.10). Non-dimensionalized by the scales (1.2), they are

$$-K_c(|\hat{\mu}\hat{u}_{\hat{z}}|\phi)_{\hat{z}} - K_v\phi|\hat{u}_{\hat{z}}|\nabla\mu = -\frac{2\rho_s \cot\alpha}{9} f_h(\phi), \tag{1.11a}$$

$$(\hat{\mu}\hat{u}_{\hat{z}})_{\hat{z}} = -(1+\rho_s\phi) \tag{1.11b}$$

noting that the shear rate $\dot{\gamma} = |\mu u_z|$ to leading order. In Chapter 3, we will retain the pressure gradient p_x omitted in (1.11b) and derive a more general model that includes surface tension.

The basic conservation equations for the downstream flow take the form

$$0 = \frac{\partial h}{\partial t} + \frac{\partial}{\partial x}\left(\int_0^h u \,\mathrm{d}z\right), \tag{1.12a}$$

$$0 = \frac{\partial}{\partial t}(h\overline{\varphi}) + \frac{\partial}{\partial x}\left(\int_0^h \phi u \,\mathrm{d}z\right). \tag{1.12b}$$

Using the equilibrium result (1.10), we write the fluxes in terms of h and $\overline{\varphi}$ only by defining

$$f(\overline{\varphi}) = \int_0^1 \widetilde{u}(s;\overline{\varphi})\,\mathrm{d}s, \quad g(\overline{\varphi})\int_0^1 \widetilde{\varphi}(s;\overline{\varphi})\widetilde{u}(s;\overline{\varphi})\,\mathrm{d}s,$$

which puts the equations (non-dimensionalizing and dropping hats) in the simple form

$$0 = \frac{\partial h}{\partial t} + \frac{\partial}{\partial x}\left(h^3 f(\overline{\varphi})\right), \tag{1.13a}$$

$$0 = \frac{\partial}{\partial t}(h\overline{\varphi}) + \frac{\partial}{\partial x}\left(h^3 g(\overline{\varphi})\right). \tag{1.13b}$$

Solutions can therefore be obtained by first solving the equilibrium equations (1.11) to obtain $\widetilde{\varphi}$ and $\widetilde{u}$, determining $f(\overline{\varphi})$ and $g(\overline{\varphi})$ and then solving the conservation law system (1.13) viewing f, g as known scalar functions of $\overline{\varphi}$. The theory for the equilibrium system (1.11), completed in [MHH11], is therefore fundamental to study of the model. Rather than review it here we will first derive an analogous system using the suspension balance model [NB94] and contrast both approaches in Chapter 2. The conservation laws will be considered in Chapter 5.

CHAPTER 2

Suspension balance approach

The equilibrium behavior of the particles is crucial to understanding the dynamic equations. In this chapter we review the existing equilibrium theory using the diffusive flux model [MHH11] and compare to the corresponding theory using the more recent suspension balance model (abbreviated in this chapter as 'DFM' and 'SBM'), demonstrating that the two models produce similar results.

2.1 General model

While the original suspension balance model of Nott and Brady [NB94] is quite complicated, subsequent variants have been proposed that are simple enough to employ for our thin film problems (of comparable complexity to the diffusive flux model summarized in Section 1.3). Here we apply the model developed by Morris & Boulay [MB99, MM06] to the incline problem. Symbols not re-defined here are the same as in Section 1.3, and the same equilibrium assumption (1.10) is made. The governing equations for the suspension (for $\mathrm{Re} \ll 1$) are

$$\nabla \cdot \mathbf{u} = 0, \tag{2.1}$$

$$\nabla \cdot \Sigma + \rho(\phi)\mathbf{g} = 0 \tag{2.2}$$

and the particle transport equation

$$\frac{\partial \phi}{\partial t} + \mathbf{u} \cdot \nabla \phi = -\nabla \cdot \mathbf{J} \tag{2.3}$$

where the particle flux is given by (recall that $f_h = \mu_\ell(1-\phi)/\mu$ is the hindrance function)

$$\mathbf{J} = \frac{2a^2}{9\mu_\ell} f_h(\phi)(\nabla \cdot \Sigma_p + \phi \Delta\rho \mathbf{g}). \tag{2.4}$$

Note that the suspension is incompressible, in contrast to the condition (Eq. 1.8) for the DFM. To complete the model, we use the expressions for fluid and particle stress tensors Σ_f and Σ_p and the mixture stress tensor $\Sigma = \Sigma_f + \Sigma_p$ from Morris & Boulay [MB99] (alternating notation somewhat for consistency with the previous chapter). The viscous stress tensor for the suspension, $2\mu\mathbf{E} = \mu(\nabla\mathbf{u} + \nabla\mathbf{u}^T)$, is split into terms $2\mu_\ell\mathbf{E}$ (for the fluid phase) and $2(\mu - \mu_\ell)\mathbf{E}$ (for the particle phase), and there is an additional 'normal stress' σ_N in the particle phase. The expressions are

$$\Sigma_f = -p\mathbb{I} + 2\mu_\ell\mathbf{E},$$
$$\Sigma_p = \underbrace{-\mu_n(\phi)\dot{\gamma}\mathbf{Q}}_{\Sigma_N} + 2(\mu - \mu_\ell)\mathbf{E}$$

where $\mathbf{Q} = \begin{pmatrix} \lambda_1 & 0 & 0 \\ 0 & \lambda_2 & 0 \\ 0 & 0 & \lambda_3 \end{pmatrix}$ is the flow-aligned tensor (in flow, gradient, vorticity directions) with $\lambda_1 = 1, \lambda_2 = 0.8, \lambda_3 = 0.5$. The fluid viscosity μ_ℓ is constant and the effective 'normal' and suspension viscosities μ_n and μ are given (from [MM06]) by

$$\mu_n = K_n \frac{(\phi/\phi_{\max})^2}{(1 - \phi/\phi_{\max})^2}, \tag{2.5a}$$

$$\mu = 1 + \frac{5}{2}\frac{\phi}{(1 - \phi/\phi_{\max})} + K_s \frac{(\phi/\phi_{\max})^2}{(1 - \phi/\phi_{\max})^2}. \tag{2.5b}$$

with $K_n = 0.75$ and $K_s = 0.1$. The fact that the ratio μ_n/μ approaches a constant as $\phi \to \phi_{\max}$ is important and will lead to some differences in the incline problem between the diffusive flux and suspension balance models.

2.2 Thin-film equations

Consider flow down an incline in the coordinates defined in Section 1.3 with the scalings (1.2). Let $\mathbf{u} = (u, w)$ and $\mathbf{g} = g(\sin\alpha, \cos\alpha)$. The model equations, written out, are

$$-\nabla p + 2\mu_\ell \nabla \cdot (\mu\mathbf{E}) + \nabla \cdot \Sigma_N + \rho\mathbf{g} = 0, \tag{2.6}$$

$$\frac{\partial\phi}{\partial t} + \mathbf{u} \cdot \nabla\phi = -\frac{2a^2}{9\mu_\ell}\nabla \cdot \Big(f_h(\phi)\left(\nabla \cdot \Sigma_p + \phi\Delta\rho\mathbf{g}\right)\Big). \tag{2.7}$$

along with incompressibility, $\nabla \cdot \mathbf{u} = 0$. Non-dimensionalizing (2.6) with the scales (1.2) with the shear rate $\dot{\gamma} \sim U/H$ leads to (recall that $\epsilon = H/L \ll 1$ is the lubrication parameter)

$$(\mu_s \hat{u}_{\hat{z}})_{\hat{z}} + \epsilon(-\hat{p} + \hat{\Sigma}_N^{xx})_{\hat{x}} + \hat{\rho} = O(\epsilon^2), \tag{2.8}$$

$$(-\hat{p} + \hat{\Sigma}_N^{zz})_{\hat{z}} - \hat{\rho} \cot \alpha = O(\epsilon). \tag{2.9}$$

Applying the normal stress boundary condition at the top interface ($z = h$), the pressure is

$$p = \hat{\Sigma}_N^{zz} + \cot \alpha \int_z^h \hat{\rho} \, \mathrm{d}z'$$

so (2.8) can be written as

$$(\mu_s \hat{u}_{\hat{z}})_{\hat{z}} + \hat{\rho} = \epsilon(\hat{\Sigma}_N^{zz} - \hat{\Sigma}_N^{xx}) + \epsilon \cot \alpha \, \partial_{\hat{x}} \left(\int_z^h \hat{\rho} \, \mathrm{d}z' \right) + O(\epsilon^2)$$

i.e. the hydrostatic pressure term typical in lubrication theory and the normal stress differences typical in the SBM (see e.g. [MB99]) both appear at order $O(\epsilon)$.

For the particle transport equation (2.7), replacing $\nabla \cdot \Sigma_p$ by $-\rho \mathbf{g} - \nabla \cdot \Sigma_f$ gives

$$\frac{\partial \phi}{\partial t} + \mathbf{u} \cdot \nabla \phi = \frac{2a^2}{9\mu_\ell} \nabla \cdot \Big(f_h \left(-\nabla p + \mu_\ell \nabla^2 \mathbf{u} + \rho_\ell \mathbf{g} \right) \Big).$$

Scaling and omitting some stress terms that are higher order in ϵ:

$$\begin{aligned} U(\phi_{\hat{t}} + \hat{u}\phi_{\hat{x}} + \hat{w}\phi_{\hat{z}}) = {} & \frac{2a^2}{9\mu_\ell} \partial_{\hat{x}} \left(f_h \left(-\frac{P}{L} \hat{p}_{\hat{x}} + \frac{\mu_\ell U}{\epsilon^2 L^2} \hat{u}_{\hat{z}\hat{z}} + \rho_\ell g \sin \alpha \right) \right) \\ & + \frac{2a^2}{9\mu_\ell \epsilon} \partial_{\hat{z}} \left(f_h \left(-\frac{P}{\epsilon L} \hat{p}_{\hat{z}} + \frac{\mu_\ell U}{\epsilon L^2} \hat{w}_{\hat{z}\hat{z}} - \rho_\ell g \cos \alpha \right) \right) + \cdots . \end{aligned} \tag{2.10}$$

Now substitute for P and U using the scalings (1.2):

$$\frac{9a^2}{2H^2} \left(\phi_{\hat{t}} + \hat{u}\phi_{\hat{x}} + \hat{w}\phi_{\hat{z}} \right) = \partial_{\hat{x}} \Big(f_h \left(-\epsilon \hat{p}_{\hat{x}} + \hat{u}_{\hat{z}\hat{z}} + 1 \right) \Big) + \frac{1}{\epsilon} \partial_{\hat{z}} \Big(f_h \left(-\hat{p}_{\hat{z}} + \epsilon \hat{w}_{\hat{z}\hat{z}} - \cot \alpha \right) \Big).$$

With the equilibrium assumption (1.1) the leading-order balance at $O(\epsilon^{-1})$ is

$$-\hat{p}_{\hat{z}} = \cot \alpha. \tag{2.11}$$

The equation at $O(1)$, leaving in the next highest order term for now, is

$$\phi_{\hat{t}} + \hat{u}\phi_{\hat{x}} + \hat{w}\phi_{\hat{z}} = \frac{2a^2}{9H^2} \Big(\partial_{\hat{x}} x (f_h [\hat{u}_{\hat{z}\hat{z}} + 1]) + \partial_z (f_h \hat{w}_{\hat{z}\hat{z}}) \Big).$$

The leading order balances (2.11) along with (2.9) and (2.8) provide ODEs for $\hat{u}$ and ϕ describing the balance between stress and gravity for the suspension and particle phases:

$$(\mu_s(\phi)\hat{u}_{\hat{z}})_{\hat{z}} = -(1+\rho_s\phi), \tag{2.12a}$$

$$(\mu_n(\phi)|\hat{u}_{\hat{z}}|)_{\hat{z}} = -\frac{\rho_s \cot\alpha}{\lambda_2}\phi, \tag{2.12b}$$

subject to the constraints $\int_0^h \phi \,\mathrm{d}z = \overline{\varphi}$ and $\hat{u}_{\hat{z}}(\hat{z}=h) = 0$. From incompressibility of the suspension (Eq. (2.1) in the general model) and the kinematic condition,

$$\frac{\partial h}{\partial t} + \frac{\partial}{\partial x}\left(\int_0^h u \,\mathrm{d}z\right) = 0.$$

From the particle transport equation (2.3) and the kinematic condition,

$$\frac{\partial}{\partial t}(h\overline{\varphi}) + \frac{\partial}{\partial x}\left(\int_0^h \phi u \,\mathrm{d}z\right) = -\frac{\partial}{\partial x}\left(\int_0^h J^{(x)} \,\mathrm{d}z\right)$$

which differs from the DFM because the suspension is exactly incompressible here; however, the term on the right hand side vanishes to leading order, so the difference is irrelevant in the thin-film limit. One then obtains the conservation PDEs in the same way as in Section 1.3, and they have the same form as in (1.13):

$$\begin{aligned} 0 &= \frac{\partial h}{\partial t} + \frac{\partial}{\partial x}\left(h^3 f(\overline{\varphi})\right) \\ 0 &= \frac{\partial}{\partial t}(h\overline{\varphi}) + \frac{\partial}{\partial x}\left(h^3 g(\overline{\varphi})\right). \end{aligned}$$

where

$$f(\overline{\varphi}) = \int_0^1 \widetilde{u}(s;\overline{\varphi}) \,\mathrm{d}s, \quad g(\overline{\varphi}) \int_0^1 \widetilde{\varphi}(s;\overline{\varphi})\widetilde{u}(s;\overline{\varphi}) \,\mathrm{d}s.$$

The only difference between the conservation laws between the models, therefore, is that the values of the fluxes are determined by different equilibrium equations. With both models derived for the incline problem, we now proceed to detailing the process for obtaining the equilibrium solution $(\widetilde{\varphi}, \widetilde{u})$ and study the properties of the solutions.

2.3 Equilibrium theory

To fully decouple the equations between the x and z directions, we proceed as in Murisic et. al. [MPP13], now generalized to accommodate both the DFM and SBM approaches and

review some basic notation and results that will be used in later chapters. Define a scaled height variable $s = z/h$ and scaled velocity and shear stress

$$\widetilde{u}(s) = h^{-2}u(x, sh, t), \quad \sigma(s) = \mu\widetilde{u}'.$$

Recall that at a fixed-x cross section, the suspension has an average concentration

$$\overline{\varphi}(x,t) = \frac{1}{h}\int_0^h \phi(x,z,t)\,\mathrm{d}z$$

and that we seek a function $\phi(s, \overline{\varphi})$ satisfying (1.10):

$$\phi(x,z,t) = \widetilde{\varphi}(z/h; \overline{\varphi}(x,t)).$$

Hereafter, x and t will be assumed to be fixed and (for the most part) will be left out entirely of the notation; from this perspective the average concentration $\overline{\varphi} = \frac{1}{h}\int_0^h \phi\,\mathrm{d}z$ is regarded as a constant. Because only the z-direction is being considered, it is convenient to simply write ϕ instead of $\widetilde{\varphi}$ for the (equilibrium) concentration profile, as the distinction between $\widetilde{\varphi}(z)$ and $\phi(x,z,t)$ is not needed.

For the equilibrium ODEs of either model (Eq. 1.11 for the DFM and (2.12) for the SBM) the system takes the form (writing $' = d/ds$)

$$\sigma' = -(1 + \rho_s\phi) \tag{2.14a}$$

$$\phi' = \begin{cases} \frac{M(\phi, |\sigma|')}{\sigma A(\phi)} & 0 < \phi < \phi_{\max} \\ 0 & \phi = 0 \text{ or } \phi_{\max} \end{cases} \tag{2.14b}$$

for functions M and A to be specified, subject to the constraints

$$\sigma(1) = 0, \qquad \int_0^1 \phi\,\mathrm{d}s = \overline{\varphi}. \tag{2.15}$$

The condition $\sigma(1) = 0$ is the tangential stress boundary condition. Observe that the boundary conditions and (2.14a) imply that $\sigma \geq 0$, so $|\sigma|$ (in the terms depending on the total shear rate $|\dot{\gamma}|$) may be replaced by σ and M may be regarded as a function of ϕ only

by using (2.14a). When we consider the model with surface tension in Chapter 3, this will not be true. For the DFM, the functions M and A are (solving for $d\phi/ds$ in Eq. 1.11a)

$$M(\phi) = -B(1-\phi) + \phi(1+\rho_s\phi), \quad A(\phi) = 1 + \frac{c_v\phi}{2\mu}\frac{\mathrm{d}\mu}{\mathrm{d}\phi}, \qquad B := \frac{2\rho_s \cot\alpha}{9K_c} \tag{2.16}$$

with $c_v := 2(K_v/K_c - 1)$. See [MHH11] for details. For the SBM, they are

$$M(\phi) = -B\phi + \frac{\mu_n}{\mu}(1+\rho_s\phi), \quad A(\phi) = (\mu_n/\mu)', \qquad B := \frac{\rho_s \cot\alpha}{\lambda_2}. \tag{2.17}$$

This is obtained by writing (2.12a) and (2.12b), respectively, as

$$\sigma_s = -(1+\rho_s\phi),$$
$$\left(\frac{\mu_n(\phi)}{\mu_s(\phi)}\sigma\right)_s = -\frac{\rho_s \cot\alpha}{\lambda_2}\phi$$

and then differentiating the latter equation to solve for ϕ'. One can think of B as a constant representing the relative strength of buoyancy to shear-induced migration (as observed in [MPP13]) and M as measuring the net migration flux in the $+z$ direction, with $M > 0$ if shear-induced migration is stronger than settling and $M < 0$ if the opposite is true. The key feature of M is that for negatively buoyant particles, M may change sign at a 'critical concentration'. Following [MHH11], this is formally defined as follows:

Definition 2.1. The *critical concentration* ϕ_c is the unique root of $M(\phi)$ in $(0, \phi_{\max})$ if it exists (assumed to be unique). If $M > 0$ then ϕ_c is defined to be zero and if $M < 0$ then ϕ_c is defined to be $\phi_{\max}$.

For (2.14), $\phi \equiv \phi_c$ is always a solution (including the degenerate cases), with $\sigma = (1+\rho_s\phi_c)(1-s)$. The critical concentration gives a precise definition of the settled and ridged regimes:

Definition 2.2. A monotonic solution to (2.14) is called 'settled' if there exists $s_0 < 1$ such that $\phi(s) = 0$ for $s > s_0$ and 'ridged' if $\phi > 0$ for all $s \in [0,1]$.

A 'solution' refers here to a piecewise C^1 solution (which may not be differentiable because of the jump in ϕ' at $\phi_{\max}$). As shown in [WB14], solutions exist (allowing for a cusp between piecewise segments satisfying the ODE) and are monotonic in $\overline{\varphi}$:

Lemma 2.1 (from [WB14]). *Piecewise C^1 solutions $\phi(s;\overline{\varphi})$ to (2.14) exist for all $\overline{\varphi} \in [0, \phi_{max}]$ and are monotonically increasing in $\overline{\varphi}$. The solutions are settled when $\overline{\varphi} < \phi_c$, ridged when $\overline{\varphi} > \phi_c$ and constant when $\overline{\varphi} = \phi_c$.*

Note that although the proof (not reproduced here) uses the DFM version of the ODE system, it applies without modification to any system of the form (2.14) when M is only a function ϕ, so the lemma is true for the SBM as well by the same argument.

2.4 Comparison of models

For completeness, we also consider a modification of the SBM for dense suspensions due to Boyer et. al. [BPG11], which replaces the viscosities (2.5) from earlier work with an improved model that agrees well with experimental data at very high concentrations:

$$\mu_n^B = \frac{(\phi/\phi_{\max})^2}{(1-\phi/\phi_{\max})^2},$$
$$\mu_s^B = 1 + \frac{5}{2}\frac{\phi}{(1-\phi/\phi_{\max})} + f_c(\phi)\frac{(\phi/\phi_{\max})^2}{(1-\phi/\phi_{\max})^2} \tag{2.18}$$

where $I_0 = 0.005$, $f_1 = 0.32$, $f_2 = 0.7$ are empirical and $f_c(\phi) = f_1 + (f_2 - f_1)\left(1 + \frac{I_0}{(\phi_{\max}-\phi)^2}\right)$.

For typical parameters, the critical concentration $\phi_c(\alpha)$ (as a function of angle) is shown for the three models in Figure 2.1a. The curves are similar enough that they should all be consistent with the experimental data collected in [MHH11] to justify use of the DFM in the incline problem. Using μ_n, μ from (2.5) gives satisfactory results (except for very small angles), while (2.18) looks a bit strange for small angles but is a closer fit in magnitude. The solutions $\phi(s;\overline{\varphi})$ are also similar between the models. Figure 2.1b shows these profiles $\phi(s;\overline{\varphi})$ at an angle $\alpha = 30\,\text{deg}$ for each model.

The most notable qualitative difference, visible in Figure 2.1b, is that the SBM profiles allow $\phi = \phi_{\max}$ at $s < 1$ when $\overline{\varphi}$ is near $\phi_{\max}$. This is due to the fact that $A \to \infty$ as $\phi \to \phi_{\max}$ in the DFM but A approaches a finite constant for the SBM and is the primary

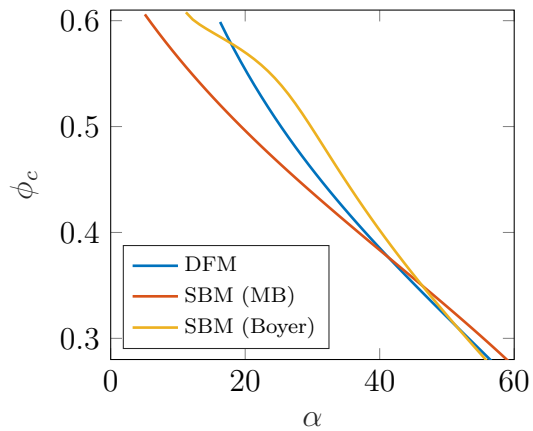

(a) Critical concentration $\phi_c(\alpha)$ vs. angle.

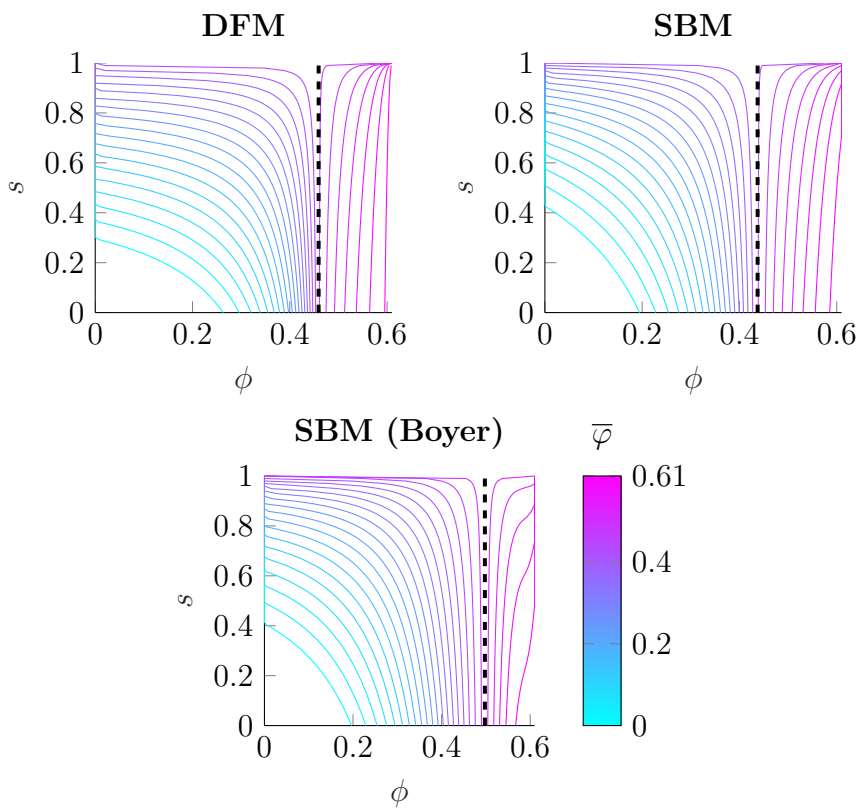

(b) For $\alpha = 30\,\text{deg}$, concentration $\phi(s;\overline{\varphi})$ (with $\overline{\varphi}$ from 0 to $\phi_{\max}$ from blue to purple).

Figure 2.1: Comparison between the diffusive flux (DFM) and suspension balance (SBM) models with viscosities from Morris (2.5) and Boyer (2.18).

difference between the two ODE systems at high concentrations. The behavior is either

$$A \sim c_v \left(1 - \frac{\phi}{\phi_{\max}}\right)^{-1}, \qquad \phi \to \phi_{\max}$$

or (using the expressions for μ, μ_n from Eq. 2.5)

$$A \sim \frac{K_n}{K_s} - \frac{5}{2} K_s \phi_{\max} \left(1 - \frac{\phi}{\phi_{\max}}\right)$$

so $A \to K_n/K_s = 7.5$ as $\phi \to \phi_{\max}$. In the first case, $\phi' \sim C(\phi_{\max} - \phi)$ near $\phi_{\max}$ if the other terms are bounded away from zero, preventing ϕ from reaching $\phi_{\max}$ unless we also have $\sigma \to 0$, which only occurs at $s = 1$. There is no such restriction in the second case, so there is nothing preventing solutions from reaching $\phi_{\max}(s)$ at a point $s_0 < 1$ (the solution is then continued with $\phi \equiv \phi_{\max}$ for $s_0 < s \leq 1$.). The formation of this packed layer affects the behavior of the fluxes used in the dynamic problem in the limit $\overline{\varphi} \to \phi_{\max}$, which is detailed in the Section 6.1 of the Appendix and is utilized in Chapter 5.

2.5 Discussion

The qualitative similarity except at very large concentrations suggests that the simpler diffusive flux model is adequate for a qualitative study of the incline problem. Because the equations for incline flow have very similar structure between the two models, they are mostly interchangeable from a mathematical perpsective. Although we use the DFM to study the addition of surface tension in Chapter 3, the suspension balance approach yields similar equations (the derivation of which supplied in the Appendix). In studying the dynamic problem for monodisperse suspensions, we will consider both models, making use of the results in this chapter. However, there is relatively little known about modeling bidensity suspensions with the SBM, so we use only the DFM for the bidensity problem of Chapter 4.

CHAPTER 3

Model with surface tension

While previous models have been successful in capturing the dynamics of the bulk flow for suspensions on an incline, they do not provide a description of the detailed structure of the fluid front. Near the front, surface tension can become a dominant effect, leading to the growth of a capillary ridge and fingering instabilities [Hup82, BB97]. For a pure viscous fluid, retaining the effects of surface tension and spreading due to the normal component of gravity, one obtains an equation for the film height $h(x,t)$ of the form

$$h_t + q(h)_x = -(f(h)h_{xxx})_x + (g(h)h_x)_x$$

In particular, $f, g \sim h^3$ as $h \to 0$ for the standard thin film equation with no slip. Equations of this type possess a rich mathematical theory and are challenging to solve numerically due to the fourth-order degenerate diffusion term [BF90]. In recent years, many extensions to complex fluid flow have been studied, models of which manifest as a similar equation for the film height coupled to some transport for the second phase (for example, surfactant-driven flow [CM09], in which a surface concentration of particles is tracked). In the case of a uniform equilibrium profile, the model for viscous suspensions was studied through numerical simulations in [MB11] and the linear stability of traveling wave solutions was studied in [CAB09].

For a non-uniform equilibrium profile, as we have studied in the previous chapters, one obtains a similar kind of system to prior work, but with a more complicated coupling between the fluid and particle transport equations. Here we introduce a model for particle-laden flow with surface tension that extends the model of Murisic et. al. [MPP13]. As we will demonstrate, there are subtle issues in constructing the model, so we focus on the one

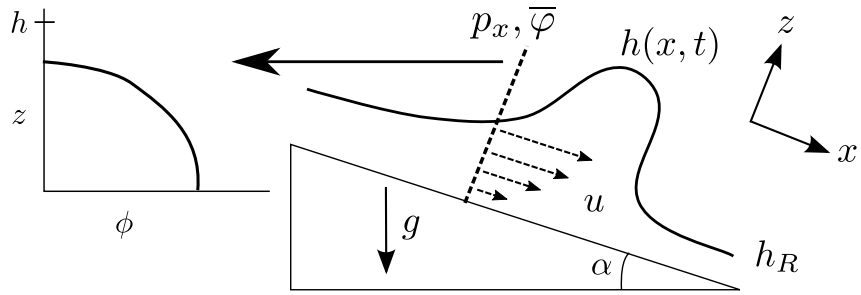

Figure 3.1: Model with added pressure gradient under equilibrium assumption; at each vertical slice x (dashed line), the particle distribution is determined by the pressure gradient $p_x(x,t)$ and total concentration $\overline{\varphi}(x,t)$.

dimensional case where the span-wise variation is neglected. Even in one dimension, the addition of surface tension and the presence of particles will significantly change the type of the model due to the complicated non-linear dependence of the fluid and particle fluxes on the pressure gradient. The equilibrium theory and numerical simulations developed here serve a foundation for future work in analysis of the PDE system and understanding the effect of particles on the fingering instability of the fronts. This chapter is a version of a collaboration submitted for publication [MWW16] (see Acknowledgments).

3.1 Model with surface tension

Here we derive the depth-integrated conservation laws for the flow, accounting for surface tension and the normal component of gravity. The starting point is the same as in the model of Murisic et. al. without surface tension (see Section 1.3), employing the same model for the suspension and particle transport along with the scalings (1.2) to non-dimensionalize the equations. We only consider the diffusive flux model here; the suspension balance approach yields equations of the same form (see Appendix, Section 6.3).

A schematic of the general setup is shown in Figure 3.1; there is now a pressure gradient p_x as well as integrated concentration $\overline{\varphi}$ to consider in the equilibrium problem.

For considering the effect of surface tension, define the capillary number $\mathrm{Ca} := \mu U/\gamma_s$ where γ_s is the surface tension of the fluid along with the scaled surface tension coefficient

$$\beta = \epsilon^3 \mathrm{Ca}^{-1}.$$

It will be assumed that γ_s is constant (independent of surface particle concentration); at least for the typical materials used in our experiments, the effect of particles on γ_s is small and can be safely neglected [MWW16]. Inclusion of contact line dynamics are beyond the scope of this work; here we assume a downstream precursor layer with height h_R as is often done for thin films [BB97]. For simplicity, we will also typically use a uniform (non-zero) concentration throughout the domain.

The boundary conditions in the lubrication limit, omitting small terms, are as follows:

$$\mathbf{u} = 0 \text{ at } z = 0 \tag{3.1a}$$

$$\mathbf{J} \cdot \mathbf{n} = 0 \text{ at } z = 0, h \tag{3.1b}$$

$$\mu u_z = 0 \text{ at } z = h \tag{3.1c}$$

$$p = p_a - \gamma_s \kappa \text{ at } z = h \tag{3.1d}$$

$$h_t = -u h_x + w \text{ at } z = h \tag{3.1e}$$

corresponding, respectively, to no-slip at the incline surface, no-flux for the particles at both surfaces, tangential/normal stress balances at the free surface and the kinematic condition. Here p_a is atmospheric pressure, $\kappa = h_{xx}/(1 + h_x^2)^{3/2}$ is the curvature and the normal vector is $\mathbf{n} = (0, -1)$ at $z = 0$ and $\mathbf{n} = (-h_x, 1)$ at $z = h$. To leading order, $\kappa \sim h_{xx}$ and $\mathbf{n} \sim (0, 1)$.

3.1.1 Thin-film equations

Particle equilibrium

Non-dimensionalizing using the scales (1.2) (using hats for non-dimensional variables) and omitting higher order terms in ϵ, the momentum equations (1.5) become

$$(\hat{\mu}\hat{u}_{\hat{z}})_{\hat{z}} = \epsilon\hat{p}_{\hat{x}} - \hat{\rho} + O(\epsilon^2) \tag{3.2a}$$

$$\hat{p}_{\hat{z}} = -\hat{\rho}\cot\alpha + O(\epsilon) \tag{3.2b}$$

which immediately yields the pressure

$$\hat{p} = p_a - \epsilon^2 \mathrm{Ca}^{-1}\hat{\kappa} + \cot\alpha \int_{\hat{z}}^{\hat{h}} \hat{\rho}\,\mathrm{d}z. \tag{3.3}$$

Hereafter, we drop the hats; quantities are assumed to be non-dimensional. The goal now is to derive thin-film equations (without z) for the flow given that we can obtain the equilibrium profile at each (x,t) (see Figure 3.1). For now we assume that (1.10) holds; this is certainly true if the $\epsilon\hat{p}_{\hat{x}}$ term is omitted in the momentum equation (3.2). The functions $\widetilde{\varphi}$ and $\widetilde{u}$ can now be integrated appropriately to remove the z-dependence. Note that if surface tension is considered then (1.10) must be modified to include the pressure gradient, i.e. $\phi = \widetilde{\varphi}(z/h; \overline{\varphi}, \hat{p}_{\hat{x}})$. This complication will be addressed shortly in Section 3.1.2; the integration process is the same regardless. Integrating the 'incompressibility' condition (1.8) and particle transport equation (1.6) in z, applying the kinematic condition and the no-flux boundary condition yields

$$\frac{\partial}{\partial t}(h\overline{\varphi}) + \frac{\partial}{\partial x}\left(\int_0^h \phi u\,\mathrm{d}z\right) = -\frac{\partial}{\partial x}\left(\int_0^h J^{(x)}\,\mathrm{d}z\right) \tag{3.4a}$$

$$\frac{\partial h}{\partial t} + \frac{\partial}{\partial x}\left(\int_0^h u\,\mathrm{d}z\right) = -\frac{\partial}{\partial x}\left(\int_0^h J^{(x)}\,\mathrm{d}z\right). \tag{3.4b}$$

Depth-integration

It remains to complete the integration to obtain useful forms for the fluxes. We will denote functions like $\widetilde{\varphi}$ that depend on $(s, \overline{\varphi})$ with a tilde. For convenience, given $\phi(x,z,t)$ or $\widetilde{\varphi}(s)$,

define the operators

$$K[g] = \int_0^z \frac{1}{\mu(\phi)} g(z_1)\,\mathrm{d}z_1, \qquad \widetilde{K}[\tilde{g}] = \int_0^s \frac{1}{\mu(\widetilde{\varphi})} \tilde{g}(s_1)\,\mathrm{d}s_1$$

for functions g of z or $\tilde{g}$ of s (with other variables held fixed). The x-derivative of $\int \phi\,\mathrm{d}z$ will be necessary in terms of the equilibrium distribution $\widetilde{\varphi}$. Using subscripts to denote partial derivatives,

$$\begin{aligned}
\frac{\partial}{\partial x}\left(\int_z^h \phi\,\mathrm{d}z'\right) &= \frac{\partial}{\partial x}\left(\int_z^h \widetilde{\varphi}(z_1/h, \overline{\varphi})\,\mathrm{d}z_1\right) \\
&= h_x \widetilde{\varphi}\Big|_{z=h} + \int_z^h \left(-\frac{z_1}{h^2} h_x \widetilde{\varphi}_s + \widetilde{\varphi}_{\overline{\varphi}} \overline{\varphi}_x\right)\,\mathrm{d}z_1 \\
&= h_x \left(s\widetilde{\varphi} + \int_s^1 \widetilde{\varphi}(s_1; \overline{\varphi})\,\mathrm{d}s_1\right) + h\overline{\varphi}_x \int_s^1 \widetilde{\varphi}_{\overline{\varphi}}(s_1; \overline{\varphi})\,\mathrm{d}s_1. \qquad (3.5)
\end{aligned}$$

Integrating the x-momentum equation (3.2) twice and applying the stress boundary conditions gives

$$u = -K\left[\int_z^h \hat{\rho}\,\mathrm{d}z'\right] + (\beta\kappa_x - \epsilon\cot\alpha h_x)K[h-z] - \epsilon\rho_s \cot\alpha K\left[\int_z^h \frac{\partial}{\partial x}\left(\int_{z'}^h \phi\,\mathrm{d}z''\right)\,\mathrm{d}z'\right].$$

To scale out h, define the following 'equilibrium' integrals $\tilde{I}_i(s; \overline{\varphi})$ by

$$\tilde{I}_0 = \widetilde{K}\left[\int_s^1 (1 + \rho_s \widetilde{\varphi}(s_1; \overline{\varphi}))\,\mathrm{d}s_1\right] \qquad (3.6a)$$

$$\tilde{I}_1 = \widetilde{K}[1-s] \qquad (3.6b)$$

$$\tilde{I}_2 = \rho_s \widetilde{K}\left[\int_s^1 \left(s_1\widetilde{\varphi} + \int_{s_1}^1 \widetilde{\varphi}(s_2; \overline{\varphi})\,\mathrm{d}s_2\right)\,\mathrm{d}s_1\right] \qquad (3.6c)$$

$$\tilde{I}_3 = \rho_s \widetilde{K}\left[\int_s^1 \int_{s_1}^1 \widetilde{\varphi}_{\overline{\varphi}}(s_2, \overline{\varphi})\,\mathrm{d}s_2\,\mathrm{d}s_1\right]. \qquad (3.6d)$$

Changing variables to $s = z/h$ and applying (3.5) gives

$$u = -h^2\tilde{I}_0 + (\beta\kappa_x)h^2\tilde{I}_1 - \epsilon\cot\alpha\left(h^2 h_x(\tilde{I}_1 + \tilde{I}_2) + h^3\overline{\varphi}_{\hat{x}}\tilde{I}_3\right)$$

Now define the (scaled) 'fluxes'

$$f_i(\overline{\varphi}) = \int_0^1 \tilde{I}_i\,\mathrm{d}s, \quad \text{for } i = 0,1,3 \quad \text{and } f_2(\overline{\varphi}) = \int_0^1 \tilde{I}_1 + \tilde{I}_2\,\mathrm{d}s - \overline{\varphi}\tilde{f}_3 \qquad (3.7a)$$

$$g_i(\overline{\varphi}) = \int_0^1 \widetilde{\varphi}\tilde{I}_i\,\mathrm{d}s, \quad \text{for } i = 0,1,3 \quad \text{and } g_2(\overline{\varphi}) = \int_0^1 \widetilde{\varphi}(\tilde{I}_1 + \tilde{I}_2)\,\mathrm{d}s - \overline{\varphi}\tilde{g}_3. \qquad (3.7b)$$

The conservation equations (1.12) for h and the integrated density $\psi = h\overline{\varphi}$, written in terms of the fluxes (3.7), become the pair of PDEs

$$h_t + (h^3 f_0)_x = -\beta(h^3 f_1 h_{xxx})_x + \epsilon \cot\alpha \left(h^3(f_2 h_x + f_3 \psi_x)\right)_x \tag{3.8a}$$

$$\psi_t + (h^3 g_0)_x = -\beta(h^3 g_1 h_{xxx})_x + \epsilon \cot\alpha \left(h^3(g_2 h_x + g_3 \psi_x)\right)_x . \tag{3.8b}$$

With downstream gravity

Note that if the downstream flux due to gravity $\mathbf{J}_g$ is retained in the basic conservation equation (3.4) then one has the modified system

$$0 = \frac{\partial h}{\partial t} + \frac{\partial}{\partial x}\left(\int_0^h u + \frac{a^2}{H^2}\frac{2\beta}{9}\phi f_h(\phi)\,\mathrm{d}z\right) \tag{3.9a}$$

$$0 = \frac{\partial}{\partial t}(h\overline{\varphi}) + \frac{\partial}{\partial x}\left(\int_0^h \phi u + \frac{a^2}{H^2}\frac{2\beta}{9}\phi f_h(\phi)\,\mathrm{d}z\right) \tag{3.9b}$$

which retains the effect of gravity moving particles relative to the fluid (this will always be the next largest term past leading order in the above, since the first correction term to u is $O(\epsilon)$ and $\epsilon \ll a^2/H^2$). The left hand side of the PDE system (3.8) is then

$$h_t + \frac{\partial}{\partial x}\left(h^3 f_0 + \frac{a^2}{H^2} h g_{grav}\right) = \cdots$$

$$(h\overline{\varphi})_t + \frac{\partial}{\partial x}\left(h^3 g_0 + \frac{a^2}{H^2} h g_{grav}\right) = \cdots$$

where $g_{grav}(\overline{\varphi}) = \frac{2\beta}{9}\int_0^1 \widetilde{\varphi} f_h(\widetilde{\varphi})\,\mathrm{d}s$.

The first term of the flux in (3.9) scales like $h^3/3$ while the second scales with h, so the gravity term will always become large as $h \to 0$. However, we have assumed $a/H \ll h$ for the continuum approximation to be valid, which is (typically) enough to ensure that the gravity term is small when $\beta = O(1)$ and ϕ is not too small or large. For ϕ near 0 or $\phi_{\max}$, the balance might change; see Appendix, Section 6.1.

3.1.2 Complications from the pressure term

The simple equilibrium assumption, that $\widetilde{\varphi}$ depends only on the depth-averaged $\overline{\varphi}$, holds only if the effect of the pressure gradient $\epsilon\hat{p}_{\hat{x}}$ is ignored. There are two neglected contributions

in (3.3): the effect of surface tension and of the normal component of gravity. We must consider whether

$$\epsilon^3 \mathrm{Ca}^{-1} h_{\hat{x}\hat{x}\hat{x}} \sim O(1) \text{ or } o(1)$$

and whether

$$\epsilon \cot \alpha \hat{\rho}_{\hat{x}} \sim O(1) \text{ or } o(1)$$

(the limits of strong/weak surface tension and strong/weak gravity, respectively). To be able to decouple the z-dynamics, we would need to have

$$\phi(x, z, t) = \widetilde{\varphi}(z/h; \overline{\varphi}(x, t); \hat{p}_{\hat{x}}(x, t)). \tag{3.10}$$

where $\hat{p}_{\hat{x}}$ is independent of z (to leading order in ϵ). If not, and we retain the higher-order terms in the PDE (e.g. the gravity term), then we must assume $\phi \approx \widetilde{\varphi}(z/h, \overline{\varphi})$. The cases are as follows:

- As previously discussed, if both are weak, then the equilibrium assumption (1.10) holds to leading order in ϵ since then $\epsilon \hat{p}_{\hat{x}}$ is a small term in the x-momentum balance.

- If surface tension is strong and gravity is weak, then $\hat{p}_{\hat{x}} \approx \beta \hat{h}_{\hat{x}\hat{x}\hat{x}}$ is a function of (x, t) only to leading order and we can modify the equilibrium assumption to Eq. 3.10. The momentum balance is still an ODE in z for fixed (x, t) that yields and equilibrium profile $\widetilde{\varphi}$ (discussed in detail in the next chapter); none of the equilibrium integrals I_i need to be modified.

- If surface tension is weak and gravity is strong, then the $z-$ and $x-$ dynamics are now coupled through $\hat{p}_{\hat{x}}$, which depends on z and x, so (3.2) is no longer solvable as an ODE in z. Thus it is not possible to integrate out z entirely; the fluxes f_i, g_i would also depend on z. One can, however, assume (1.10) on faith (i.e. assume $\widetilde{\varphi} \approx \widetilde{\varphi}(z/h, \overline{\varphi})$). This is essentially assuming that the (hydrostatic) pressure variation only weakly affects the particle distribution, but leaving in the effect of that pressure on the integrated system.

- If both are strong, there is another problem in that differentiating $\widetilde{\varphi}$ in (3.10) with respect to x leads to variations $\hat{p}_{\hat{x}\hat{x}} \sim h_{xxxx}$, leading to unpleasant fluxes that scale with the fourth derivative of h. As in the previous case, we can assume (3.10) and that the $\hat{p}_{\hat{x}}$ variation in $\widetilde{\varphi}$ can be neglected in this part of the derivation to arrive at the PDE system for simplicity.

As can be seen here, the addition of gravity is not always compatible with the equilibrium assumption. In the last two cases, we will revert back to the simpler equilibrium (1.10) as a first approximation. A more refined model that can allow for coupling between the $z-$ and $x-$ dynamics is left to future work.

3.1.3 In two dimensions

The extension to two dimensions - accounting for the transverse flow on the incline - is mostly straightforward if the x and y length scales are taken to be the same. The main subtlety is that the shear stress $\dot{\gamma}$ is no longer simply $|u_z|$ as it contains contributions also from the y-direction.

In the lubrication model, no boundary conditions are imposed in the y-direction; in practice, no-flux boundary conditions are usually applied to the resulting PDEs to represent the effect of the bounding walls. The coordinates scales are

$$(x, y, z) = L(\hat{x}, \hat{y}, \epsilon\hat{z}), \quad (u, v, w) = U(\hat{u}, \hat{v}, \epsilon\hat{w}). \tag{3.11}$$

The mean curvature is now $\kappa \sim \nabla^2 h$. The y-momentum equation is

$$(\mu_s \hat{v}_{\hat{z}})_{\hat{z}} = \hat{p}_{\hat{y}} \tag{3.12}$$

where the pressure is given by (3.3) as before. The integration process to obtain $\hat{v}$ is therefore the same as the one used to derive $\hat{u}$ in section 1.3, but without the $\hat{\rho}$ term in the momentum equation. It is then immediate that the resulting PDEs for $h(x, y, t)$ and $\psi = h\phi$ are

$$h_t + (h^3 f_0)_x = -\beta\nabla \cdot (h^3 f_1 \nabla\nabla^2 h) + \epsilon \cot\alpha \nabla \cdot \big(h^3(f_2 \nabla h + f_3 \nabla\psi)\big) \tag{3.13a}$$

$$\psi_t + (h^3 g_0)_x = -\beta\nabla \cdot (h^3 g_1 \nabla\nabla^2 h) + \epsilon \cot\alpha \nabla \cdot \big(h^3(g_2 \nabla h + g_3 \nabla\psi)\big) \tag{3.13b}$$

with the fluxes given in (3.7). The particle equilibrium equation, however, differs slightly because the total shear rate is instead given by

$$\dot{\gamma} = \sqrt{2\mathbf{E} : \mathbf{E}} = \sqrt{|u_z|^2 + |v_z|^2} = \sqrt{|u_z|^2 + (p_y/\mu)^2} \tag{3.14}$$

to leading order. Since p_y (like p_x) is constant in z to leading order, we still have a system of ODEs in z as in the previous section, with a solution now parameterized by $(\overline{\varphi}, p_x, p_y)$. The particle equilibrium equation $J^{(z)} = 0$ is (1.11a) with $\dot{\gamma}$ as above rather than $|\mu u_z|$. The effect of the additional p_y^2 term on particle equilibrium will be briefly explored in the next section; the additional complexity makes the equations rather cumbersome and is beyond the scope of this work.

As a final note on the two-dimensional model, the validity of (3.14) warrants some discussion. Note that the principal direction of migration is in the z-direction for shear-induced migration due to either component. There are serious modeling concerns that arise in multi-directional flows where this is not true (e.g. in curvilinear flows; see [KBL96]; adapting the model for complex flows was the subject of considerable debate and is still a difficult problem [MM06]). Essentially, this extended model assumes the migration will be the same as in a uni-directional shear flow with velocity $\mathbf{u} = u(z)\hat{x} + v(z)\hat{y}$ rather than $\mathbf{u} = u(z)\hat{x}$. With different scalings for x and y in (3.11), the model might take a different form. Study of the two dimensional equations is an interesting avenue for future research, but is beyond the scope of this work.

3.2 Equilibrium theory

As shown in the derivation of the model, the applied pressure gradient $p_x(x, t)$ to the system does not depend on z when only surface tension contributes to the pressure. It therefore manifests in the ODEs as a constant, allowing us to study the equilibrium problem in isolation.

Denote this constant by p_x; the ODE system is then

$$\sigma' = p_x - (1 + \beta\phi) \tag{3.15a}$$

$$\phi' = \begin{cases} \frac{M(\phi, |\sigma|')}{\sigma A(\phi)} & 0 < \phi < \phi_{\max} \\ 0 & \phi = 0 \text{ or } \phi_{\max} \end{cases} \tag{3.15b}$$

with boundary conditions $\int_0^1 \phi \, \mathrm{d}s = \overline{\varphi}, \sigma(1) = 0$,

$$M = -B(1 - \phi) - \phi|\sigma|'$$

and the other parameters as in prior work (see [MPP13] or Section 2.3). As before, $\phi \equiv \phi_c$ and $\sigma = (p_x - 1 - \beta\phi_c)(1 - s)$ is always a solution of (3.15). The critical concentration is almost the same:

Definition 3.1. The *critical concentration* $\phi_c(p_x)$ for (3.15) is the unique value $\phi_c \in (0, \phi_{\max})$ solving

$$M(\phi_c, p_x - (1 + \beta\phi_c)) = 0$$

when it exists and $\phi_{\max}$ otherwise.

Surprisingly, the added constant greatly complicates the system. In contrast to the equations without surface tension in Section 1.3 or Chapter 2, σ is no longer single-signed - depending on p_x it may cross zero in the interior of the domain. Hence we cannot replace $|\sigma|'$ using (3.15a) and $|\sigma|'$ is not even well-defined when $\sigma = 0$. To simplify matters, we choose to regularize the total shear rate $|\sigma|$ by adding a small value:

$$|\sigma| \approx \sqrt{\sigma^2 + \delta_s^2} \tag{3.16}$$

where δ_s is taken (arbitrarily) to be about 10^{-3}; so long as it is small the value does not matter much. Note that the σ in (3.15a) is the viscous shear stress μu_z while the $|\sigma|$ is the total shear rate $\dot{\gamma}$ in the particle migration model; we are regularizing the latter but not changing the former so the σ in (3.15a) is left untouched. While δ_s is added primarily for mathematical convenience, it has some physical basis and has been used in past work [RL08, MM06]. The

continuum model breaks down within an $O(a)$ distance of the free surface (where a is the particle diameter), and there is typically a small non-local contribution to the stress there (so $\sigma(1) \neq 0$). The correct way to model this subtlety remains unexplored and is an avenue for future work. In the two dimensional model, including the transverse pressure gradient p_y (see section 3.1.3) can also provide this small regularization.

3.2.1 Types of solutions

There are now additional types of piecewise-smooth solutions, depending on p_x. Define the following useful values:

$$
\begin{aligned}
p_x^{(1)} &= -\frac{B(1-\phi_{\max})}{\phi_{\max}} + 1 + \beta\phi_{\max} \\
p_x^{(2)} &= 1 + \beta\phi_{\max} \\
p_x^{(3)} &= \min\left\{\frac{B(1-\phi_{\max})}{\phi_{\max}} + 1 + \beta\phi_{\max},\, 1 - B + 2\sqrt{B\beta}\right\}.
\end{aligned}
$$

Then $\phi_c(p_x) < \phi_{\max}$ for $p_x \notin (p_x^{(1)}, p_x^{(3)})$ and $\phi_c = \phi_{\max}$ otherwise. The $(p_x, \overline{\varphi})$ plane (with $\overline{\varphi} \in [0, \phi_{\max}]$) can be partitioned into regions, shown in Figure 3.2, defined as follows:

$$
\begin{aligned}
\Omega_R^+ &= \{\overline{\varphi} > \phi_c\} \cap \{p_x > p_x^{(3)}\}, \\
\Omega_R^- &= \{\overline{\varphi} > \phi_c\} \cap \{p_x < 1\}, \\
\Omega^* &= \{\alpha > \phi_c\} \cap \{1 < p_x < p_x^{(1)}\} \\
\Omega_S &= \{\overline{\varphi} < \phi_c\} \cap \{p_x > p_x^{(3)} \text{ or } p_x < p_x^{(1)}\}, \\
\Omega_P &= \{1 + \beta\overline{\varphi} > p_x > 1\}
\end{aligned}
$$

Also define the boundary segment

$$\Gamma = \partial\Omega_R^- \cap \partial\Omega_P.$$

A unique, monotonic ridged solution exists in Ω_R^+ and in $\Omega_R^- \cap \{p_x < 1\}$, while a unique monotonic settled solution exists in Ω_S. It follows immediately from the equation for σ' and the boundary condition $\sigma(1) = 0$ that σ is single-signed in these regions (positive when $p_x < 1$ and negative when $p_x > p_x^{(2)}$).

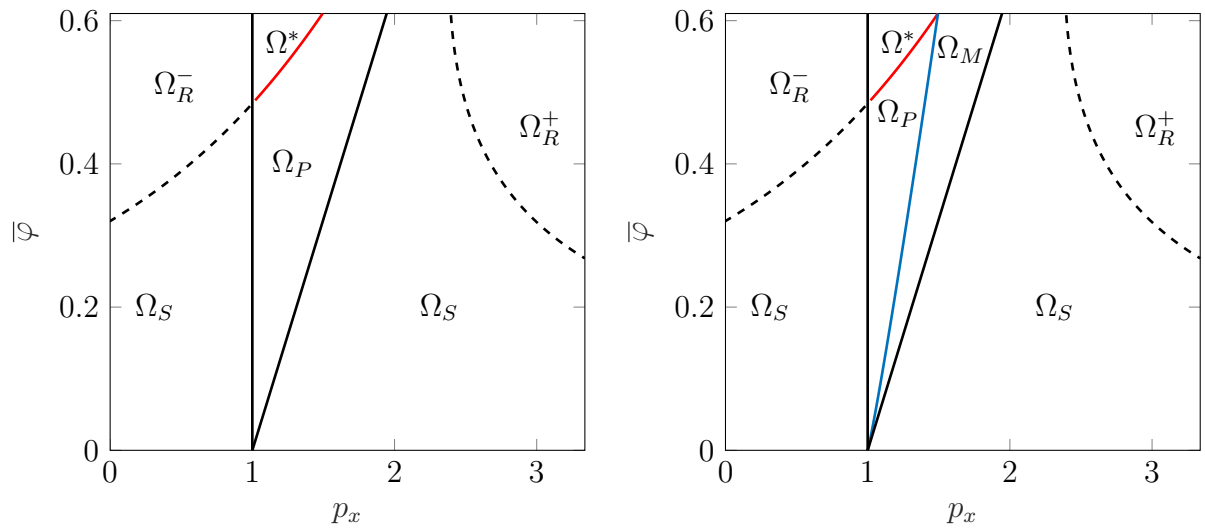

Figure 3.2: Phase diagram for $p_x \neq 0$ and $\alpha = 50\,\text{deg}$ for the problem (3.15) with (left) and without (right) regularized shear stress (3.16); the red line indicates the segment across which the solutions $\phi(s; \overline{\varphi}, p_x)$ are discontinuous. Solutions are ridged in $\Omega_R^\pm$, settled in $\Omega_S^\pm$, peaked in Ω_P and packed in Ω_M (see Definition 3.2).

In the other regions, the behavior is more complicated. Solution profiles (fixing p_x) are shown in Figure 3.3 corresponding to the regions. In addition to the monotonic settled/ridged solutions (Def. 2.2), define two new types of solutions:

Definition 3.2. A piecewise C^1 solution to (3.15) is *peaked* if there are s^*, s_0 with $0 < s^* < s_0 < 1$ such that $\sigma(s^*) = 0$ for some $s^* \in (0, 1)$ and ϕ has a unique maximum at s^*. A *packed* solution to (3.15) is the same except that $\phi = \phi_{\max}$ for $s \in [0, s^*]$.

Peaked solutions have particles accumulating where the shear rate is zero, somewhere in the middle of the fluid; packed solutions are similar but particles form a settled bed of particles (at the maximum packing fraction) below this point.

Note that a peaked solution can be turned into a packed solution by simply setting $\phi = \phi_{\max}$ for $s < s^*$, which means we need to choose solutions judiciously. The goal is to find family of solutions $\phi(s; \overline{\varphi}, p_x)$ that varies continuously with its parameters. This turns out to be impossible; the best that can be done is the following:

Claim 3.1 (Existence, continuity of solutions)**.** *A family of solutions $\phi(s;\phi,p_x)$ can be selected in the entire $(p_x,\overline{\varphi})$ plane that varies continuously except across Γ; the choice is unique and any other selection would be discontinuous across $\{p_x=1\}$. If $\delta_s>0$ then all solutions in Ω_p are peaked (and $\phi(s;\overline{\varphi},p_x)<\phi_{max}$). If $\delta_s=0$ then in Ω_p, there is a curve $\phi_p(p_x)$ such that solutions are peaked when $\overline{\varphi}>\phi_p(p_x)$ and packed when $\overline{\varphi}<\phi_p(p_x)$.*

When $(p_x,\overline{\varphi})\in\Omega_P$, it is easy to see the sign of σ must change at some interior point s^*, which allows for peaked solutions. The maximum of ϕ will be very close to $\phi_{\max}$ for the regularized problem (but always less than $\phi_{\max}$) so there are no packed solutions. Otherwise, $\sigma(s^*)=0$ which forces $\lim_{s\to s^*}\phi\to\phi_{\max}$ and allows for either peaked or packed solutions. Only one is correct in the limit $\delta_s\to 0$, providing a way to choose between the two. Within Ω_P there is a curve $\phi_p(p_x)$ such that solutions chosen this way are packed $\overline{\varphi}<\phi_p$ (in a region Ω_M) and are peaked otherwise (this is stated without proof, which would most likely be tedious and uninteresting). The modified phase diagram for $\delta_s=0$ is shown in Figure 3.2.

In Ω^* the situation is similar but there are additionally the usual 'ridged solutions'. Because peaked solutions are not monotonic in $\overline{\varphi}$ (the total concentration), there may also be multiple solutions satisfying $\int_0^1\phi\,\mathrm{d}s=\overline{\varphi}$. In fact, very close to the boundary $\{\overline{\varphi}=\phi_c, 1<p_x<p_x^{(1)}\}$, there are three solutions for each $\overline{\varphi}$ and p_x (two sign-changing, one ridged. This suggests the model includes a sort of hysteresis where there are multiple particle equilibria; it is, however, most likely a technicality rather than a meaningful physical effect.

To verify that peaked solutions are necessary, we consider the transition across $p_x=1$. In order to make this transition continuous (in $\phi(s;\overline{\varphi},p_x)$) it is necessary to select the peaked solution. If $p_x<1$ and $\overline{\varphi}<\phi_c$ then we are in Ω_S and solutions have $\phi<\phi_c$. Hence a solution just to the right of $p_x=1$ must also be uniformly close to $\phi=\phi_c$, which excludes the packed solutions having $\phi=\phi_{\max}$ near $s=0$ and leaves only the peaked solutions. On the other hand, across $p_x=1$ with $\overline{\varphi}>\phi_c$, one must choose the ridged solutions or forgo continuity and choose packed solutions instead. These continuity concerns constrain the selection as described in the claim.

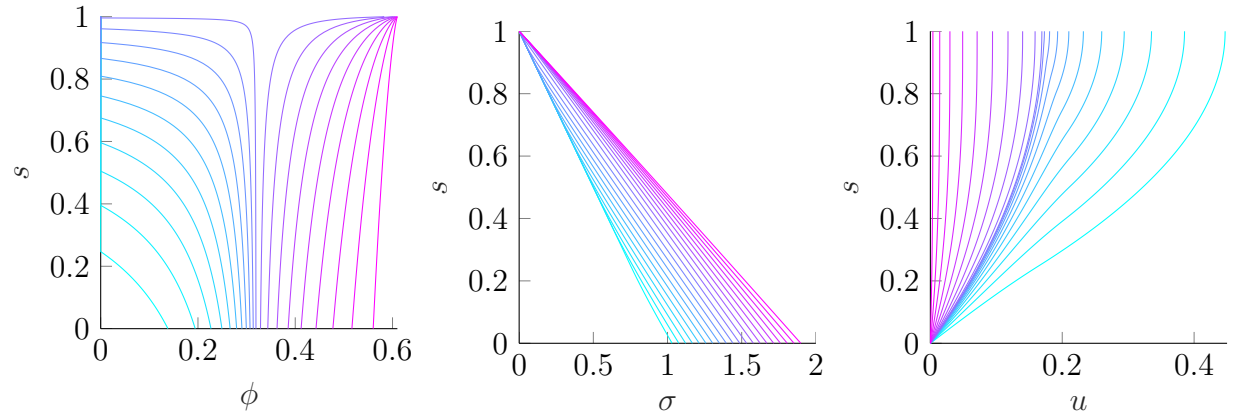

(a) settled/ridged solutions, $p_x = 0$

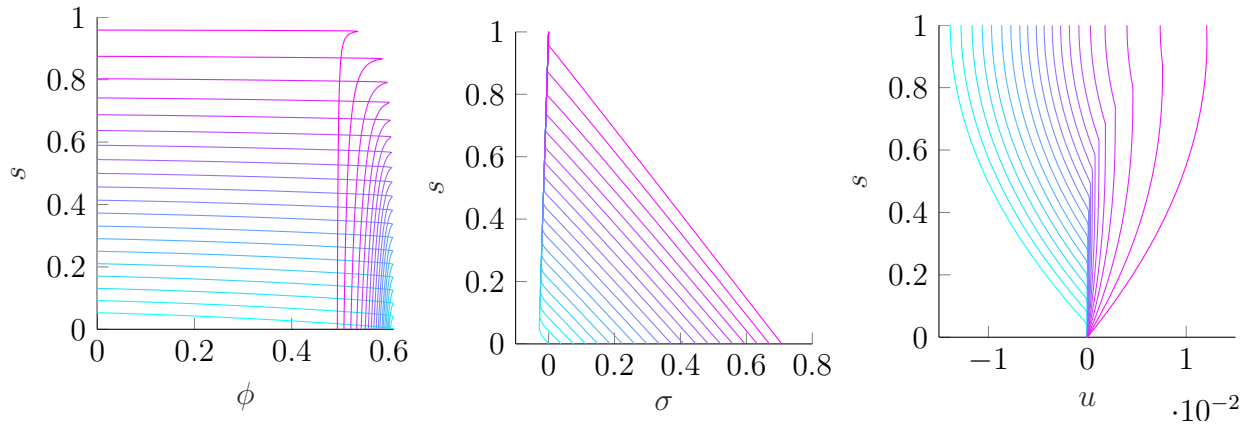

(b) peaked solutions for $p_x = 1.3$ ($\overline{\varphi}$ from 0 to ϕ_c)

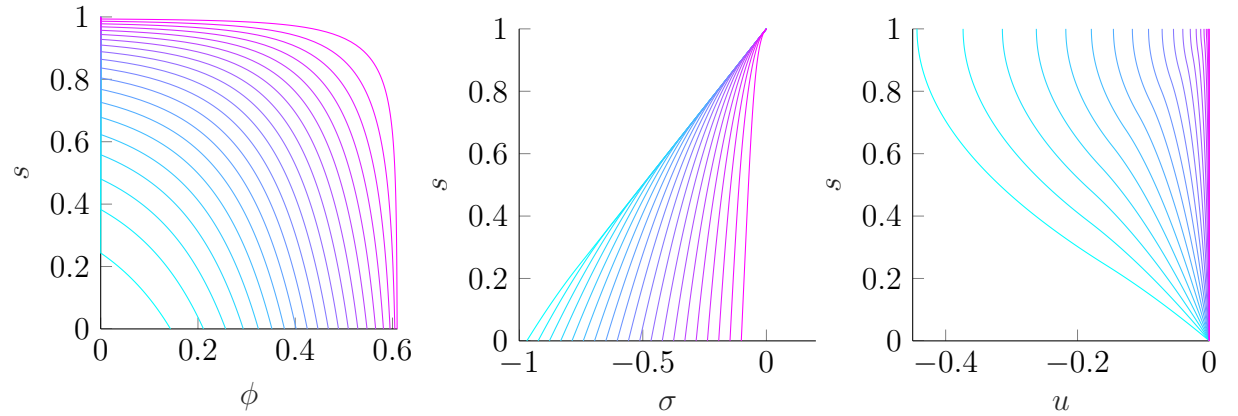

(c) settled solutions, $p_x = 0$ ($\phi_c = \phi_{\max}$)

Figure 3.3: From left to right: Particle equilibrium profiles ϕ, shear stress σ and velocity u as $\overline{\varphi}$ is varied from 0 to $\phi_{\max}$ for certain values of p_x. These correspond to vertical slices of the phase diagram in Figure 3.2.

Dilute limit (near $p_x = 1$)

Examining the dilute limit for $p_x \neq 0$ reveals some of the difficulties that arise near $p_x = 1$; the usual (asymptotic) estimates from the previous section break down here. Rather than exhaust all possibilities we focus on one illustrative case. The dilute limit for p_x not close to 1 can be found in [MWW16]. Let $\delta = p_x - 1$ and assume that $\delta < 0$; we examine the limit $\delta \to 0^-$. As before, impose the constraint $\overline{\varphi} = \epsilon$ with $\epsilon \ll 1$. Suppose also that ϕ_c exists and that

$$|\delta| < \frac{2\beta\overline{\varphi}}{\phi_c^2}$$

which is the condition that the linear solution in the dilute limit (derived by [MPP13] and detailed in the Appendix, Section 6.1 starting with Eq. 6.1),

$$\phi = B(T - s)_+ + O(\epsilon), \qquad T := \sqrt{\frac{2\epsilon}{B}}$$

followed backwards from $s = T$, reaches ϕ_c before hitting $s = 0$. Near T the solution is still linear. We modify the solution by adding a new region near $s = 0$:

$$\phi(s) = \begin{cases} p(s) & 0 < s < T_0, \\ \frac{B}{|\delta|}(T - s)_+ & s > T_0 \end{cases} \tag{3.17}$$

where p is assumed to satisfy $p(s) = \phi_c + O(\delta)$ for $s < T_0$. Numerical solutions for $\delta \to 0^-$ are shown in Figure 3.4. Patching the two segments together where they both equal ϕ_c to leading order and enforcing $\int \phi \, \mathrm{d}s = \epsilon$ gives

$$T = \frac{\epsilon}{\phi_c} + B_1|\delta|, \quad T_0 = \frac{\epsilon}{\phi_c} - \frac{B\phi_c|\delta|}{2} \tag{3.18}$$

where $B_1 = \phi_c(1/B - B/2)$; note also that the linear region has a width of $T - T_0 = |\delta|\phi_c/B$. The key point to observe is that $T = O(\epsilon + |\delta|)$ rather than $T = O(|\delta|^{1/2}\epsilon^{1/2})$ as in the normal dilute solution. After a lengthy computation (see Appendix, Sec. 6.4), we find that the particle flux G satisfies

$$G = O(\overline{\varphi}(1 + |\delta|)^3) \tag{3.19}$$

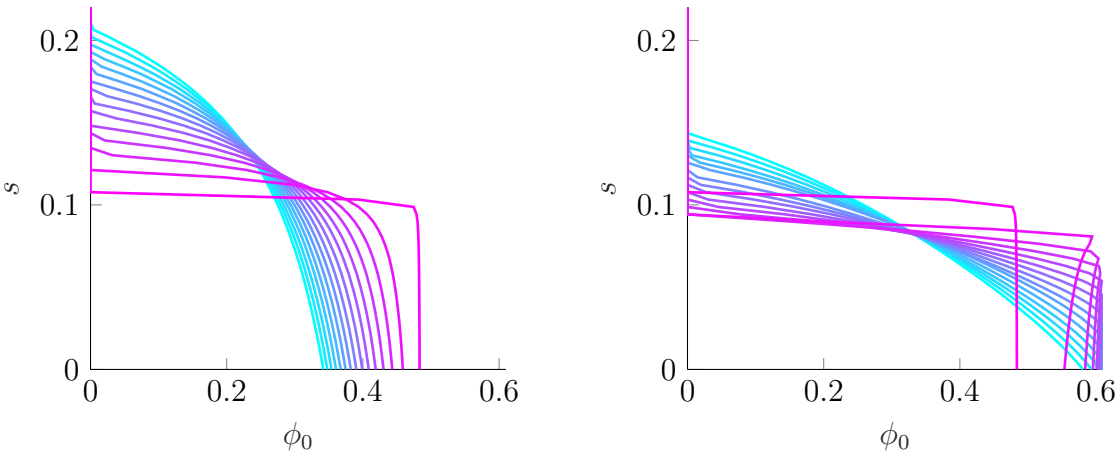

(a) $\delta \to 0^-$ limit ($\delta = 0.7$ to $\delta = 1$)

(b) $\delta \to 0^+$ limit ($\delta = 1.2$ to $\delta = 1$)

Figure 3.4: With $\overline{\varphi} = 0.05$ fixed, dilute solutions as $\delta \to 0$ (with $\delta = P - 1$) from below (left) and from above (right). The colors from blue to purple indicate δ increasing from 0.7 to 1 in (a) and decreasing from 1.2 to 1 in (b). The critical concentration is $\phi_c(P = 1) = 0.484$. Solutions approach ϕ_c near $s = 0$ as $\delta \to 0$.

rather than $G \sim C\overline{\varphi}^{3/2}|\delta|^{1/2}\delta$ and $G = O((\overline{\varphi}|\delta|)^{3/2})$ when δ is not close to 1. This is essentially due to the fact that $\max \phi \to \phi_c$ rather than $\max \phi \to 0$ as $\overline{\varphi} \to 0$.

The limit $\delta \to 0^+$ is more complicated because $\overline{\varphi}$ is large enough to make σ non-monotonic (see Figure 3.4). The profile will look like (3.17) but p may start near ϕ_c but then suddenly approach $\phi_{\max}$ where $\sigma = 0$, forming a peaked solution. We expect the same type of dependence on $\overline{\varphi}$ and δ, but the analytical details are not pursued here.

3.2.2 Effect of surface tension on fluxes

The fluxes f_i, g_i obtained from this model depend on p_x but remain bounded. To see this, it is useful to compute $f(\overline{\varphi}, p_x) \sim f_\infty(\overline{\varphi}) + \cdots$ in the limit $|p_x| \to \infty$. This is the limit ($|p_x - 1| \gg \beta\phi_{\max}$) where buoyancy is small relative to the applied pressure gradient. Since

ϕ is bounded, for large p_x the ODEs become

$$\sigma' = p_x - 1 - \beta\phi \tag{3.20}$$

$$\phi' = \frac{-B(1-\phi) - \phi\sigma'}{A(\phi)\sigma} \approx \phi - \frac{p_x - 1 - \beta\phi}{A(\phi)\sigma} \tag{3.21}$$

with $\int_0^1 \phi \, \mathrm{d}s = \overline{\varphi}$. Then σ has the approximate solution $(p_x - 1)(1 - s)$ so

$$\phi' \approx \frac{\phi}{A(\phi)(1-s)}.$$

Integrating then yields (using the DFM expression for $A(\phi)$) an exact solution

$$\frac{\phi}{(\phi_{\max} - \phi)^{c_v}} = C(1-s)$$

which is the same solution one would obtain for neutrally buoyant particles (essentially, the p_x term is causing any gravity term to be relatively small). Regardless of the exact solution, there is some $\phi_\infty(s)$ solving the ODE in the $|p_x| \to \infty$ limit. One therefore has

$$u_\infty \sim (p_x - 1)I_1 + I_0$$

recalling that (in this case) $I_1 \sim \int_0^s \mu(\phi_\infty(s'))^{-1}(1-s') \, \mathrm{d}s'$ and $I_0 \sim \int_0^s \mu^{-1}(1 + \beta\phi_\infty) \, \mathrm{d}s'$. Thus f_0 and the other fluxes approach a (bounded) function $f_\infty(\overline{\varphi})$ as $|p_x| \to \infty$ (visible in Figure 3.5b). In general, the fluxes have a significant dependence on p_x; they tend to increase as $|p_x| \to \infty$ (which makes sense as the diminishing effect of gravity leads to more particles away from the substrate where u is small). The fluxes also have a discontinuity due to the discontinuity of the solutions (as previously discussed); the effect of p_x is shown for $p_x < 1$ and $p_x \to \infty$ separately (where they are continuous) in Figure 3.5b.

Discussion

The added pressure gradient allows for solutions to have particle accumulation at arbitrary points in the interior of the fluid, rather than just at the surface (due to shear-induced migration) or the substrate (due to settling). It is not clear from this preliminary study whether the technicalities of the model - namely, the lack of uniqueness of solutions and

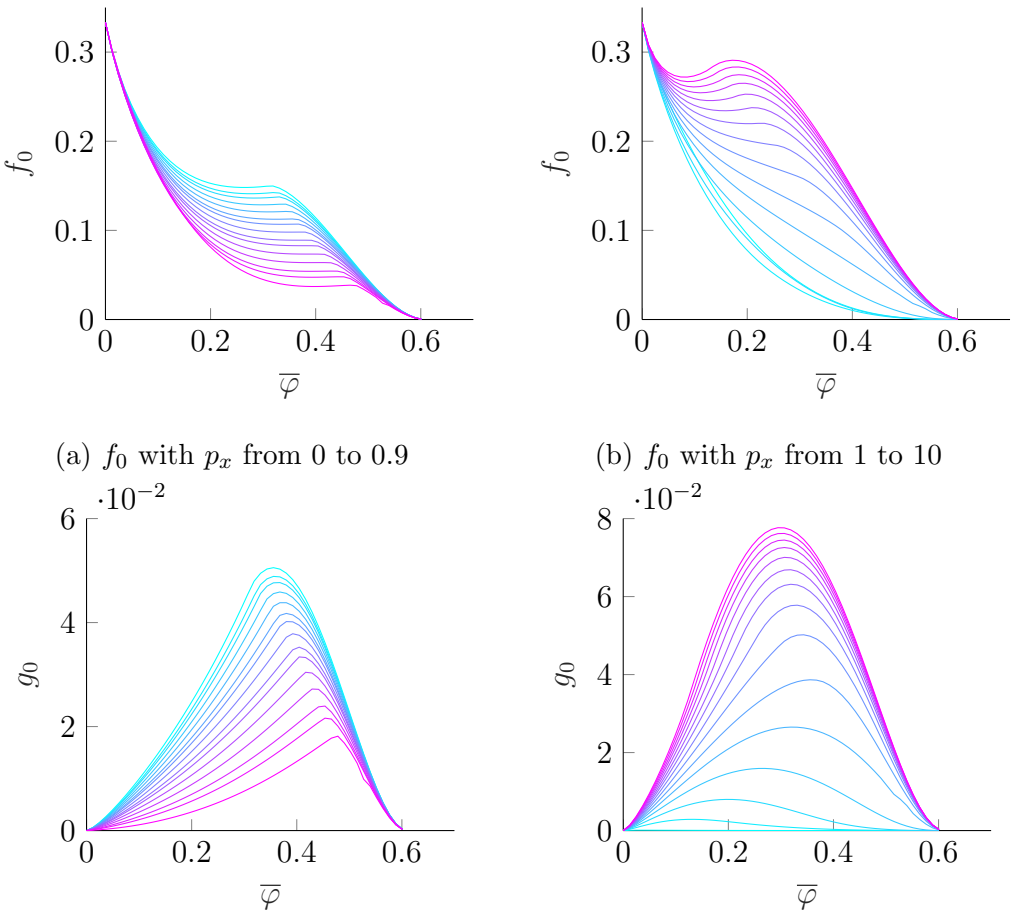

(a) f_0 with p_x from 0 to 0.9

(b) f_0 with p_x from 1 to 10

(c) g_0 with p_x from 0 to 0.9

(d) g_0 with p_x from 1 to 10

Figure 3.5: Fluxes f_0, g_0 defined in (3.7) for the equilibrium with added pressure gradient p_x (Eq. 3.15) in the two regimes $p_x < 1$ and $p_x > 1$ (the fluxes are discontinuous across $p_x = 1$).

discontinuities - are artifacts or of real significance. It is plausible to have discontinuities as a consequence of the equilibrium assumption: the 'equilibrium' profiles $\widetilde{\varphi}(s)$ are actually steady states of some complicated migration process. Hence non-uniqueness may be indicative of multiple possible steady states - or it may suggest that the model should be modified in the delicate regime where the pressure gradient and density terms balance. At the very least, this shows how the equilibrium assumption may be too severe (as it cannot account for the stability of steady states if there are more than one), and it would be interesting in future work to relax this assumption to better understand the dynamics.

3.3 Numerical scheme

Hereafter, we consider the system (3.8) without the second-order terms; the effect of these terms is left for future work. In this section, we explain in detail the numerical scheme for solving the system. Omitting hats and recalling that $p_x = -\beta h_{xxx}$, the system reads

$$h_t + \left(h^3 f\right)_x = -\beta \left(h^3 f_1 h_{xxx}\right)_x, \tag{3.22a}$$

$$\psi_t + \left(h^3 g\right)_x = -\beta \left(h^3 g_1 h_{xxx}\right)_x. \tag{3.22b}$$

with $\psi = h\overline{\varphi}$. Note that fluxes $f(\overline{\varphi}, p_x)$ and $g(\overline{\varphi}, p_x)$ depend on p_x, thus the left hand side of (3.22a) (3.22b) is no longer a simple hyperbolic system, which makes its discretization ambiguous. To overcome this difficulty, we rewrite the system (3.22a) and (3.22b) as

$$h_t + (h^3 f(\overline{\varphi}, 0))_x = -\beta(h^3 \tilde{f}_1 h_{xxx})_x \tag{3.23a}$$

$$\psi_t + (h^3 g(\overline{\varphi}, 0))_x = -\beta(h^3 \tilde{g}_1 h_{xxx})_x \tag{3.23b}$$

where

$$\tilde{f}_1 = f_1 + \frac{f(\overline{\varphi}, 0) - f(\overline{\varphi}, p_x)}{p_x}, \qquad \tilde{g}_1 = g_1 + \frac{g(\overline{\varphi}, 0) - g(\overline{\varphi}, p_x)}{p_x}. \tag{3.24}$$

Then the left hand side of (3.23a) (3.23b) reduces to the original model without surface tension, which has been shown to be hyperbolic [WB14]. The modified fluxes $\tilde{f}_1$ and $\tilde{g}_1$ are well-defined and bounded as $p_x \to 0$ due to the linear dependence of the equilibrium equation (3.15) on p_x. In addition, these fluxes remain non-negative. The main difficulty comes from the explicit treatment of the fourth order diffusion, which may pose a constraint on time step $\Delta t \sim \Delta x^4$, whereas implicit treatment needs a large effort in inverting a nonlinear system. We propose here a semi-implicit discretization with an explicit discretization of the nonlinear part and implicit for the linear fourth order diffusion. This idea has been employed in the lubrication type equations [WB03, MB11, BJL11], but with the addition of particle volume evolution (3.22b) new difficulties arise, as we will explain below.

Let Δx be the mesh size and Δt^k be the adpative time step at kth step. Denote $h_j^k = h(x_j, t^k)$, $(f_i)_j^k = f_i(x_j, t^k)$, and $(\overline{\varphi})_j^k = \overline{\varphi}(x_j, t^k)$, where $x_j = j\Delta x$ and $t^k = \sum_{l=0}^{k-1} \Delta t^k$. First,

we discretize the fluid flow (3.23a) as

$$\frac{h_j^{k+1}-h_j^k}{\Delta t^k}+\frac{(h^3 f(\overline{\varphi},0))_j^k-(h^3 f(\overline{\varphi},0))_{j-1}^k}{\Delta x}= \\ -\frac{\beta}{\Delta x^4}\left\{\frac{(h^3\tilde{f}_1)_j^k+(h^3\tilde{f}_1)_{j+1}^k}{2}\left(h_{j+2}^{k+1}-3h_{j+1}^{k+1}+3h_j^{k+1}-h_{j-1}^{k+1}\right)\right. \\ \left.-\frac{(h^3\tilde{f}_1)_j^k+(h^3\tilde{f}_1)_{j-1}^k}{2}\left(h_{j+1}^{k+1}-3h_j^{k+1}+3h_{j-1}^{k+1}-h_{j-2}^{k+1}\right)\right\} \quad (3.25)$$

and we use upwind difference for the transport part as the direction of the flow is downward. The fluxes f_i depend on $(\overline{\varphi})_j^k=\frac{\psi_j^k}{h_j^k}$ and

$$(p_x)_j^k=-\beta(h_{xxx})_j^k=-\beta\frac{h_{j+2}^k-2h_{j+1}^k+2h_{j-1}^k-h_{j-2}^k}{2\Delta x^3}.$$

Δx is the spatial grid and we choose it uniformly for simplicity; it can be directly generalized to nonuniform mesh if we want to refine the resolution at the wave front. The time step Δt is chosen adaptively according to some stability condition.

Next, for the particle transport (3.23b), although the fourth order diffusion is in h not in ψ, it cannot be considered as part of the flux or the source as it may render the scheme unstable. Instead, we should discretize $\beta\left(h^3\tilde{g}_1 h_{xxx}\right)_x$ in the same way as $\beta\left(h^3\tilde{f}_1 h_{xxx}\right)_x$ in (3.23a). More precisely, the scheme for (3.22b) reads

$$\frac{\psi_j^{k+1}-\psi_j^k}{\Delta t^k}+\frac{(h^3 g(\overline{\varphi},0))_j^k-(h^3 g(\overline{\varphi},0))_{j-1}^k}{\Delta x}= \\ -\frac{\beta}{\Delta x^4}\left\{\frac{(h^3\tilde{g}_1)_j^k+(h^3\tilde{g}_1)_{j+1}^k}{2}\left(h_{j+2}^{k+1}-3h_{j+1}^{k+1}+3h_j^{k+1}-h_{j-1}^{k+1}\right)\right. \\ \left.-\frac{(h^3\tilde{g}_1)_j^k+(h^3\tilde{g}_1)_{j-1}^k}{2}\left(h_{j+1}^{k+1}-3h_j^{k+1}+3h_{j-1}^{k+1}-h_{j-2}^{k+1}\right)\right\}. \quad (3.26)$$

As noticed in [WB14], one of the most important properties of the solution to the original hyperbolic system (the one without surface tension) is that $\overline{\varphi}(t,x)=\frac{\psi(t,x)}{h(t,x)}$ stays in the interval $[0,\phi_{\max}]$, even in the case of a singular shock. This is of particular importance for numerical simulation as the fluxes go to zero like $(\phi_m-\phi)^2$ as $\phi\to\phi_{\max}$, which leads to a degeneracy in the equations that must be handled with care (for the details see Lemma 6.2

of the Appendix). In what follows, we will show the reason for it and then explains how it inspires the discretization (3.26). First we have the following lemma.

Lemma 3.2. *The flux pairs* $(f_1(\overline{\varphi}),\ g_1(\overline{\varphi}))$ *and* $(f_0(\overline{\varphi}), g_0(\overline{\varphi}))$ *are non-negative and satisfy* $g_0(\overline{\varphi}) \leq \phi_{max} f_0(\overline{\varphi})$.

Proof. Since we always choose the physical solution to the equilibrium system (3.15) such that $0 \leq \phi \leq \phi_{\max}$, the averaged value $\overline{\varphi}$ also falls into the range $[0, \phi_{\max}]$. Since $I_0(s)$ in (3.6) is non-negative, from the definition of the fluxes in (3.7) we have

$$g_0(\overline{\varphi}) = \int_0^1 \phi(s) I_0(s) ds \leq \phi_{\max} \int_0^1 I_0(s) ds = \phi_{\max} f_0(\overline{\varphi}).$$

Similarly, $I_1(s)$ in (3.6) is non-negative and so $g_1(\overline{\varphi}) \leq \phi_{\max} f_1(\overline{\varphi})$. ■

To proceed, we consider a special case when $\beta = 0$, then $p_x \equiv 0$, and the fluxes $f_0(\overline{\varphi})$ and $g_0(\overline{\varphi})$ reduce to the original flux in [MPP13] without surface tension, and the system (3.22a)(3.22b) reduces to the conservation laws where a simple upwind difference scheme suffices to give the correct solution. For such a system, we have the following property.

Theorem 3.3. *If the time step* Δt^k *satisfies the CFL condition*

$$\frac{\Delta t^k}{\Delta x} \leq \min_j \left\{ \frac{1}{h^2 f_0(\overline{\varphi})},\ \frac{\overline{\varphi}}{h^2 g_0(\overline{\varphi})},\ \frac{\phi_m - \overline{\varphi}}{(\phi_m f_0(\overline{\varphi}) - g_0(\overline{\varphi})) h^2} \right\}_j^k, \tag{3.27}$$

then the solution to the system (3.25) (3.26) with $p_x \equiv 0$ *satisfies* $0 \leq \overline{\varphi}_j^k = \frac{\psi_j^k}{h_j^k} \leq \phi_{max}$.

Proof. Rewrite the upwind scheme in (3.25) and (3.26) as

$$\psi_j^{k+1} = \psi_j^k - \frac{\Delta t^k}{\Delta x} \left[(h^3 g)_j^k - (h^3 g)_{j-1}^k \right], \quad h_j^{k+1} = f_j^k - \frac{\Delta t^k}{\Delta x} \left[(h^3 f)_j^k - (h^3 f)_{j-1}^k \right].$$

Then positivity of h_j^{k+1} and ψ_j^{k+1} is guaranteed if Δt^k satisfies the CFL condition (3.27), so it is with $\overline{\varphi}_j^{k+1}$. Now let us consider the quantity $\phi_{\max} h_j^{k+1} - \psi_j^{k+1}$. Notice that

$$(\phi_{\max} h - \psi)_j^{k+1} = (\phi_{\max} h - \psi)_j^k - \frac{\Delta t^k}{\Delta x} \Big[(h^3 \phi_{\max} f - h^3 g)_j^k - (h^3 \phi_{\max} f - g)_{j-1}^k \Big],$$

thus it is easy to check that if $(\phi_{\max}h - n)_J^k = 0$ at one position x_J and a specific time t^k, $(\phi_{\max}h - \psi)_J^{k+1} = 0$ thanks to Lemma 1 and the fact $f(\phi_{\max}) = g(\phi_{\max}) = 0$. Now it is left to check that if $(\phi_{\max}h - \psi)_J^k > 0$ for any x_J and t^k, we have $(\phi_{\max}h - \psi)_J^{k+1} \geq 0$. This is readily followed by the third algebraic expression in the CFL constraint (3.27).

Remark 3.1. *The first two constraints in the CFL condition (3.27) are the common conditions to guarantee the positivity of the upwind solution, whereas the third one is an extra requirement to preserve the upper bound of $\overline{\varphi}$. However, this extra requirement is not restrictive at all. Indeed, we can check the ratio*

$$\frac{\phi_{max} - \overline{\varphi}}{\phi_{max} f_0(\overline{\varphi}) - g_0(\overline{\varphi})} \Big/ \frac{1}{f_0(\overline{\varphi})} = \frac{(\phi_{max} - \overline{\varphi}) f_0(\overline{\varphi})}{\phi_{max} f_0(\overline{\varphi}) - g_0(\overline{\varphi})}, \tag{3.28}$$

which is uniformly bounded with an $\mathcal{O}(1)$ upper bound (which is straightforward to verify; see Appendix).

Remark 3.2. *Analytically, for the hyperbolic system without surface tension ($\beta = 0$ in (3.22a) (3.22b)) if initially $h(x,0) < \phi_{max}\psi(x,0)$ and we assume the solution is sufficiently smooth, then $\overline{\varphi}(t,x) < \phi_{max}$ still holds. This can be seen following the characteristics of the system*

$$h_t + (h^3 f_0(\overline{\varphi}))_x = 0, \quad \xi_t + (h^3 \phi_{max} f_0(\overline{\varphi}) - h^3 g_0(\overline{\varphi}))_x = 0,$$

where $\xi = \phi_{max}h - \psi$ and $\overline{\varphi}$ is recovered via $\overline{\varphi} = \frac{\phi_{max}h - \xi}{h}$. However, once the shock or rarefaction forms, we need to resort to the Hugoniot locus or integral curve [WB14, MB14] to study the behavior of the solution. Indeed, in the interesting case when there is a singular shock, both h and n increase unboundedly at the wave front of the shock, but $\overline{\varphi} = \frac{\psi}{h}$ is always bounded by ϕ_{max}, which is seen from the fact that the Hugoniot locus in the $(h, \overline{\varphi})-$plane always stay below $\overline{\varphi} = \phi_{max}$ (see Fig. 4.1 and Theorem 4.1 in [WB14]). Therefore, in the case of double/singular shock, the volume concentration $\overline{\varphi}(t,x)$ is still bounded above by ϕ_{max}.

■

Therefore, in the absence of surface tension, the upper bound of $\overline{\varphi}$ is preserved both analytically and numerically. Inspired by the above argument, we notice that, in the presence

of surface tension, a good choice of discretization of the term $\beta h^3 g_1 h_{xxx}$ in (3.22b) is that it is discretized in the same manner as $\beta h^3 f_1 h_{xxx}$ in (3.22a). However, since the theory of the uniform boundedness in $\overline{\varphi}$ is still lacking for (3.22b) (3.22a), the rigorous estimate of numerical solution (3.25) (3.26) sharing the same property is beyond the scope of this paper, and we leave it to future work.

3.4 Numerical simulation

In this section, we conduct several numerical simulations to show how the model performs in the presence of surface tension. We first present the results starting from Riemann initial data representing a 'constant flux' setting. Motivated by physical experiments carried out on the experimental set-up in the Applied Mathematics Department at UCLA, we then investigate the numerical solutions for the 'constant volume' case and show some experimental results. All the simulations are carried out at an angle of $\alpha = 30\,\mathrm{deg}$. without special announcement.

3.4.1 Riemann initial data

Consider Riemann initial data

$$h(0,x) = h_R + \frac{1}{2}\left(h_L - h_R\right)\left(1 - \tanh(10x)\right), \tag{3.29}$$

and $n(0,x) = \phi_I h(0,x)$ where ϕ_I is the initial concentration, h_L and h_R are the height in the reservoir and precursor, respectively. Eq. (3.29) describes a step-like profile for the interfacial height, consistent with investigating slow flows down rectangular planes.

Settled case

We now turn our attention to the full model described by (3.22a,3.22b). First, we focus on a case where the concentration is low giving rise to the settled flow pattern, which corresponds to a double-shock solution when surface tension is neglected. We consider the following parameters $h_L = 1$, $h_R = 0.1$ and $\phi_I = 0.2$ in all simulations and investigate the effect of

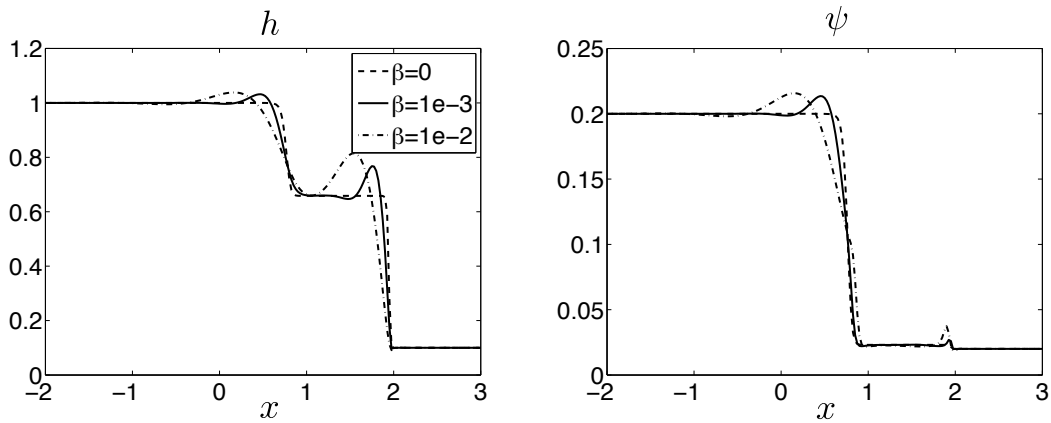

Figure 3.6: Computation of the full model given by Eqs. (3.22a) and (3.22b) with surface tension for different $\beta = 0, 1e-5, 1e-3, 1e-2$ at time $t = 15$. The left panel shows the film height solution and the right panel shows the solution of the product of the height and particle volume concentration. Here, $h_L = 1$, $h_R = 0.1$ and $\phi_I = 0.2$.

surface tension by varying the value of the parameter β. We compare the numerical solutions with $\beta = 0$, 10^{-3}, 10^{-2} at $t = 15$ in Fig. 3.6, where stronger surface tension effect results in more pronounced capillary ridge in both shocks. Here, we choose $\Delta x = 0.025$, $\Delta t = 0.01$. We observe that the previous, hyperbolic model captures the location of the front of the flow while surface tension leads to the development of two ridges: a trailing one, representing the particle-concentrated region and a leading ridge, representing the particle-free region. The leading wave forms at the contact line which we expect to be unstable to fingering. From experimental observations, the fingering is more visible at the front of the flow while, at the particle-fluid separation, the fingering appears to be more suppressed. In Fig. 3.7, we choose $\beta = 0.1$ corresponding to more distinct surface tension effects, and plot the profiles of h and ψ at different times, indicating that the solution is composed of two traveling waves. Again, $\Delta x = 0.025$, $\Delta t = 0.01$.

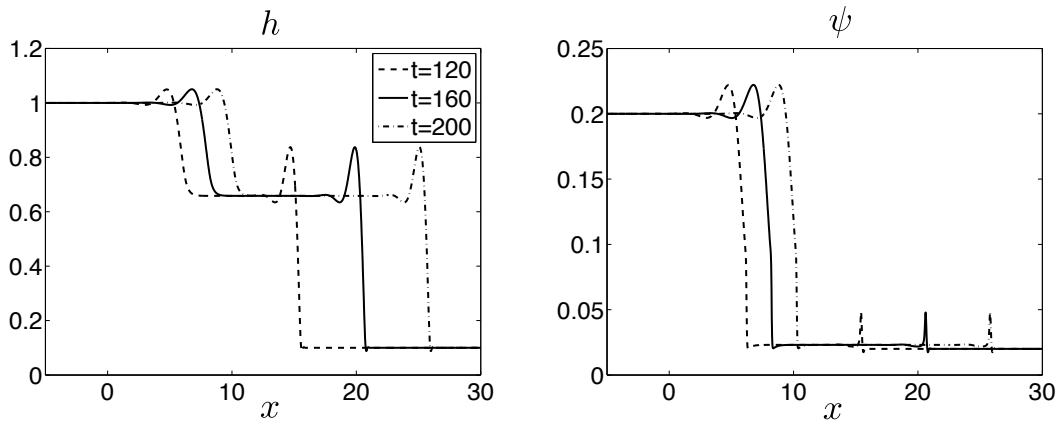

Figure 3.7: Computation of the full model given by Eqs. (3.22a) and (3.22b) with surface tension for $\beta = 1$ at different times. Here $h_L = 1$, $h_R = 0.1$ and $\phi_I = 0.2$.

Ridged case

We now explore the *double-shock* formation in the ridged regime. Consider the initial data (3.29) but with $h_L = 1$ and $h_R = 0.2$. $\phi_I = 0.5$. As shown in [WB14], this initial data will produce a double shock with intermediate height and concentration larger than the left and right states. Here we compare our results with $\beta = 0.1$ and without surface tension, i.e., $\beta = 0$. Here, we choose $\Delta x = 0.05$, $\Delta t = 0.01$. The results are gathered in Fig. 3.8 where the capillary ridge emerges in the second shock near the moving contact line in the presence of surface tension, as one would expect from experimental results.

Next, we investigate the singular shock. If we choose $h_L = 1$, $h_R = 0.02$ and $\phi_I = 0.5$, the solution to the original hyperbolic system is a singular shock. Here we first show a comparison of the solution with and without surface tension. The results are collected in Fig. 3.9 where we display the solutions at different times $t = 400$, 800, 1200, 1600, and 2000. Here the black solid curve is without surface tension, whose solution in H produces a singularity, while the blue dashed is for $\beta = 0.05$ where the profile in h has been regularized.

To further see this, we compare the maximum height of the fluid (h) for model (3.22a) (3.22b) by decreasing the mesh size, with $\beta = 0.1$ and $\beta = 0$, respectively. It is observed from Fig. 3.10 that surface tension ($\beta = 0.1$) successfully suppresses the singular shock,

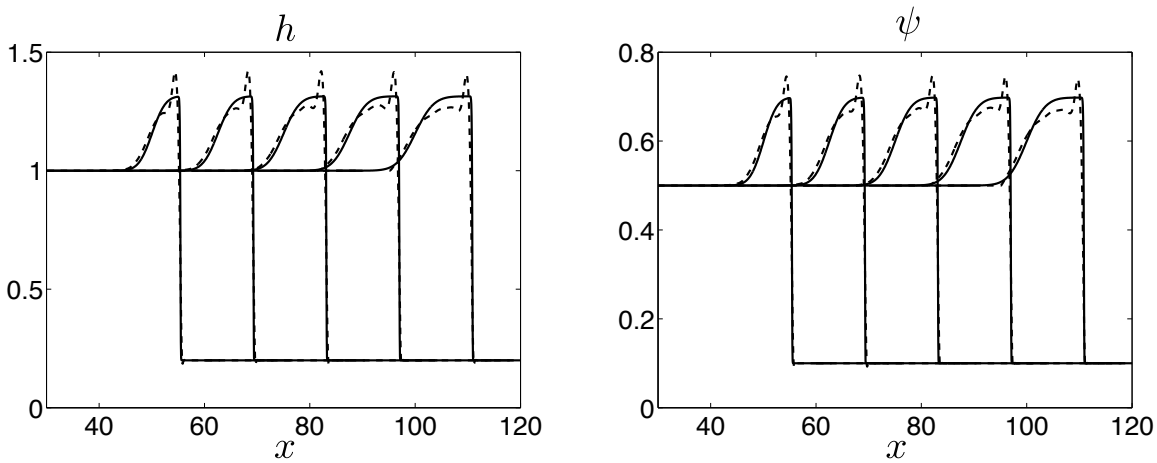

Figure 3.8: Comparison of $\beta = 0$ and $\beta = 0.1$ for different times $t = 2000$, 2500, 3000, 3500, and 4000. Blue dashed curve: $\beta = 0$. Black solid curve: $\beta = 0.1$. Here we used a moving mesh with speed $s = 0.0275$ computed from the initial data and reform the results according to the distance it should advance at the above times.

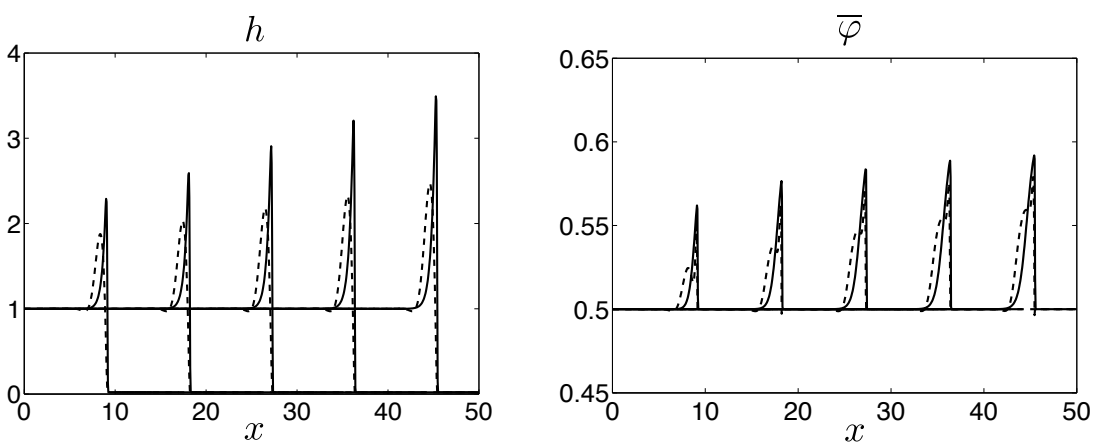

Figure 3.9: Comparsion of no surface tension (i.e., $\beta = 0$, black solid curve) and $\beta = 0.05$ (blue dashed curve) for different times $t = 400$, 800, 1200, 1600, 2000. $\Delta x = 0.05$, $\Delta t = 0.0025$.

resulting in a particle-rich ridge with uniformly bounded height for finite time. On the other hand, without surface tension the height does not have a uniform growth when we refine the mesh, indicating the presence of singularity.

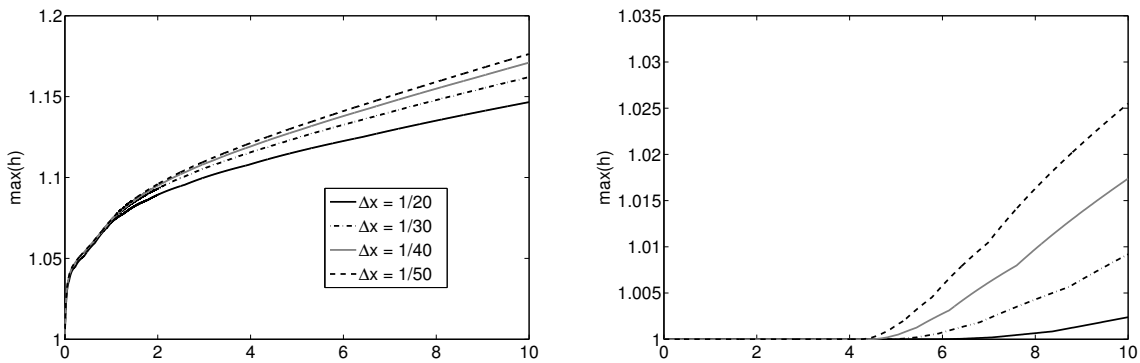

Figure 3.10: $\max_x h(t,x)$ versus t for different mesh grids for model (3.22a) (3.22b) with initial condition $h_L = 1$, $h_R = 0.02$ and $\phi_I = 0.5$. Left: $\beta = 0.1$, with surface tension. Right: $\beta = 0$, without surface tension.

3.4.2 Conserved volume initial data

In this section, we further demonstrate that the presence of surface tension will not affect the large-scale dynamics but only modify the wave front by using the laboratory parameters from recent experiments [BKK15]. In the experimental data obtained in [BKK15], height profiles for the suspension in the incline problem were obtained by use of a laser sheet, capturing the evolution of the capillary ridge. The suspension used was a viscous oil (PDMS with kinematic viscosity $\nu = 1000\,\mathrm{cSt}$ and surface tension $\gamma = 0.02\,\mathrm{N/m}$) with $0.2\,\mathrm{mm}$ particles and densities $\rho_\ell = 971\,\mathrm{kg/m^3}$ and $\rho_p = 3800\,\mathrm{kg/m^3}$, similar to previous experiments [MPP13].

With these parameters, $\beta = \frac{\epsilon^3}{Ca} = \frac{\gamma H}{L^3 \rho_l g \sin\alpha} = 0.042$. The Initial data is

$$h(0,x) = \begin{cases} \frac{110*0.75}{10*14}, & \text{for } -10 \le x \le 0 \\ \\ 0.02 * \frac{110*0.75}{10*14}, & \text{otherwise} \end{cases}, \tag{3.30}$$

$$\psi(0,x) = \phi_I h(0,x). \tag{3.31}$$

Figure 3.11 displays the comparison of solutions to model (3.22a)–(3.22b) with ($\beta = 0.042$, solid curve) and without surface tension ($\beta = 0$, dashed curve).

In Figure 3.12, we show two typical examples of measured height profiles. Varying the

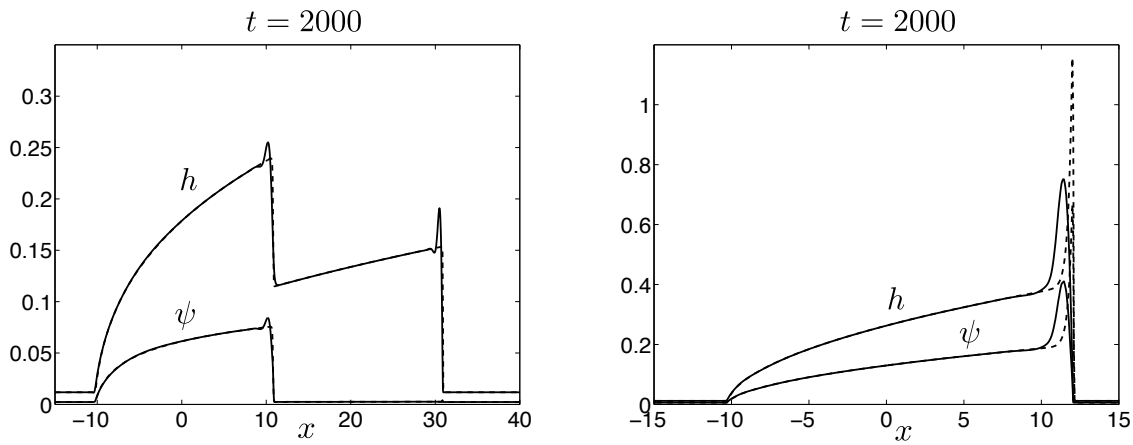

Figure 3.11: Comparison of no surface tension (i.e., $\beta = 0$, dashed curve) and $\beta = 0.042$ (solid curve) for models with initial data (3.30). Left: settled case with $\overline{\varphi} = 0.2$. Right: ridged case with $\overline{\varphi} = 0.5$.

total volume effectively changes the left and right states (as in (3.30)), thereby allowing for the possibility of detecting the transition between singular and double shocks. In the parameter regime tested, which is restricted by the equilibrium assumption, only a single, sharp ridge evolves (see Figure 3.12). Further experiments may better illuminate the behavior of the fronts (as singular shocks or otherwise) and the particle distribution therein. In addition, in the high concentration regime, non-Newtonian effects near the front may be important; this is evident, e.g. as the typical fingering instability evolves and the high-concentration 'fingers' will tend to solidify and/or break. The fingering instability also has an effect on the formation of the ridge, which makes quantitative comparison to the one-dimensional model of limited use. For these reasons, is difficult to determine whether the observed ridge corresponds to the singular shock solution (as the model would predict) or a double shock. Fully studying the physical model requires extending the model to two dimensions and including the effect of the normal component of gravity, which is beyond the scope of this work.

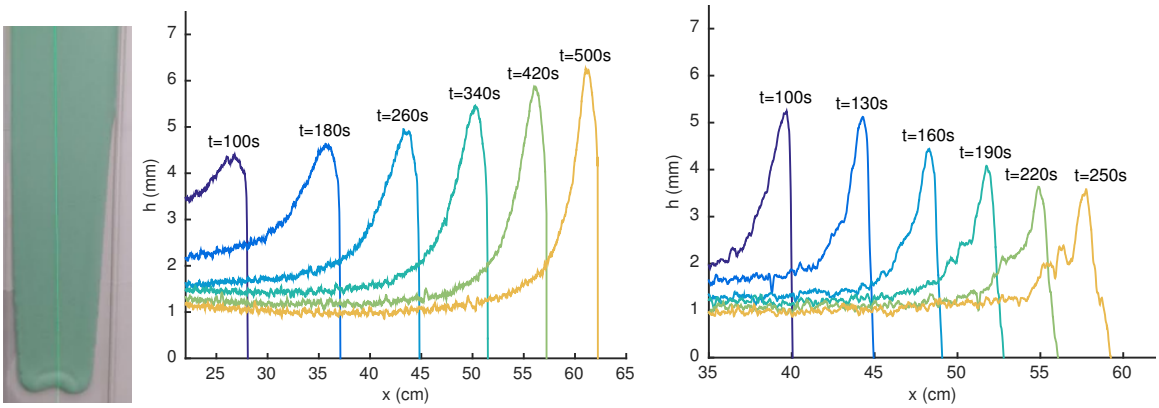

Figure 3.12: Left/center: An experimental picture and height profile near the front for $\overline{\varphi} = 0.5$ and $\alpha = 55\,\text{deg}$ (the bright green line in the left figure is the laser line from which the height profiles are measured). Right; experimental height profile for $\alpha = 45\,\text{deg}$ (right) with an initial volume of 110 ml.

3.5 Discussion

This work brings many challenging questions for future study. The model PDEs extend easily to two dimensions but the equilibrium problem becomes quite complicated. The typical fingering instabilities that arise and dependence on p_y further exacerbate the numerical difficulties we have discussed. In addition, from a physical perspective, it is not clear that the use of the total shear rate is a good approximation, as the behavior of shear-induced migration in more complicated geometries is not as straightforward and is the subject of ongoing research [RL08, MM06].

Similar equations have been studied in modeling of surfactant spreading [CM09]. These equations are also a fourth-order parabolic equation for the film height coupled to a particle transport equation which can be solved using semi-implicit methods. Mathematically, the model proposed here has some key differences which complicate the problem. The conserved form of the system is for the film height h and integrated concentration $h\phi$, while the fluxes still depend on the concentration ϕ. As a consequence, a numerical scheme in conserved form must be discretized carefully to ensure that the approximation for ϕ remains appropriately

bounded. In addition, the fluxes f, g that drive the bulk fluid motion, which are first-order in the absence of surface tension, gain a complicated non-linear dependence on h_{xxx}.

On the analysis side, the well-posedness of the system (3.22a) (3.22b) is of interest, which is of a complicated hyperbolic-parabolic type, especially in the case of a singular shock where the concentration may approach the maximum packing fraction. The degenerate diffusion term in the particle transport equation (3.8a) and dependence of the fluxes on $\overline{\varphi}$ and p_x make the problem of well-posedness (substantially) different from other thin-film models. Progress on analysis of the equations may also aid in developing numerical schemes with desirable properties, such as ensuring boundedness of the particle concentration.

CHAPTER 4

Bidensity equilibrium theory

The model readily extends to bidensity suspensions with particles of the same diameter d but different densities $\rho_{p,1}$ and $\rho_{p,2}$. We focus here on suspensions with negatively buoyant particles, in which the heavier particles are expected to settle to the substrate with the lighter particles above. Then, due to the increasing velocity profile in z, this stratification should cause the particles to separate into distinct fronts as the suspension flows down the incline. This separation is observed in experiments, as shown in Figure 4.1, and the flow also exhibits a transition between settled and ridged regimes similar to that for monodisperse suspensions. We will show here that the model does indeed predict this separation in the normal equilbrium as well as the settled/ridged bifurcation. The theory developed here is used as a foundation to study the separating fronts in the dynamic problem in Chapter 5. This chapter is a version of published work [LWB15]; see Acknowledgments.

4.1 Model

The derivation here follows [LWB15]; we return to dimensional variables and denote non-dim. quantities with a hat. Denote the particle concentrations by ϕ_1 and ϕ_2, let $\phi = \phi_1 + \phi_2$ be the total concentration of particles and let $\chi = \phi_1/\phi$ be the fraction of the first species. We employ the diffusive flux model over the suspension balance model due to the relative simplicity of the former. As shown in Chapter 2, the two models are comparable for incline flow. The setup described in Section 1.3 for the diffusive flux model is modified to account for the second particle species.

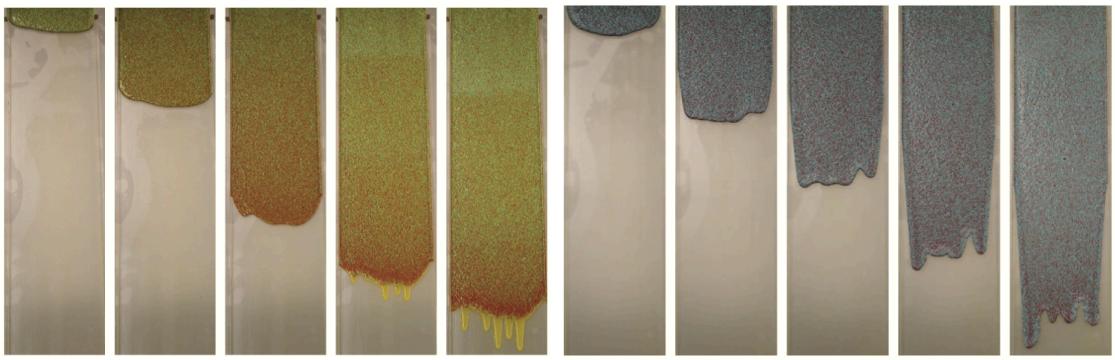

Figure 4.1: From [MLB14], a bidensity suspension of ceramic and glass beads flowing down an incline at $\alpha = 30\,\text{deg}$ (left) and $\alpha = 50\,\text{deg}$ (right). The fluid is yellow and the particles are blue (heavier) and red (lighter). The two particle types and fluid separate over time on the left, but the lighter particles collect at the leading edge on the right. Note the (unexpected) presence of heavier particles on the surface in the right figure.

The momentum equation (1.5) is the same, but the suspension density ρ is now given by

$$\rho(\phi_1, \phi_2) = \rho_\ell(1 - \phi) + \rho_{p,1}\phi_1 + \rho_{p,2}\phi_2$$

and there are now a pair of particle transport equations

$$\frac{D\phi_i}{Dt} = -\nabla \cdot \mathbf{J}_i, \qquad i = 1, 2. \tag{4.1}$$

for particle fluxes $\mathbf{J}_i$. We assume that the viscosity remains a function of ϕ only and use the same expression as in the single-species case. The sedimentation fluxes now depend on the influence of the other species; drawing upon a model for polydisperse settling [TA99] we use

$$\mathbf{J}_{i,grav} = \frac{2a^2\mathbf{g}\phi_i}{9\mu_\ell}\left(M_0(\rho_{p,i} - \rho_\ell) + M_I\sum_{j=1}^{2}(\rho_{p,j} - \rho_\ell)\frac{\phi_j}{\phi}\right)$$

where $M_0(\phi) = 1 - \phi/\phi_{\max}$ and $M_I(\phi) = f_h(\phi) - M_0(\phi)$ are self and interaction mobilities whose expressions are fitted from Stokesian dynamics simulations [RH92]. Following [TA99] we include the effect of shear induced migration for each species, along with an extra term modeling mixing between the two species in the shear flow:

$$\mathbf{J}_{i,shear} = -a^2\phi_i\left(K_c\phi\nabla(\dot\gamma\phi) - K_v\dot\gamma\phi\frac{\nabla\mu}{\mu}\right) - \dot\gamma a^2 D_{tr}(\phi)\phi\nabla(\phi_i/\phi)$$

where $D_{tr}(\phi) = K_t\phi^2$ with $K_t = 0.4$ (the coefficient here comes from numerical simulations, following [TA99]; there are some more precise forms that can be used but this is reasonable and convenient). Since $\nabla(\phi_1/\phi) + \nabla(\phi_2/\phi) = 0$, the total flux $\mathbf{J} = \mathbf{J}_1 + \mathbf{J}_2$ is

$$\mathbf{J} = -a^2\phi\left(K_c\phi\nabla(\dot{\gamma}\phi) - K_v\dot{\gamma}\phi\frac{\nabla\mu}{\mu}\right) + \frac{2a^2\mathbf{g}}{9\mu_\ell}f_h(\phi)\left(\sum_{j=1}^{2}(\rho_{p,j} - \rho_\ell)\phi_j\right).$$

Note that the mixing terms vanish. It is also useful to compute

$$(\phi_2\mathbf{J}_1 - \phi_1\mathbf{J}_2) = \frac{2a^2\mathbf{g}}{9\mu_\ell}\phi_1\phi_2 M_0(\rho_{p,1} - \rho_{p,2}) - \dot{\gamma}a^2\phi^2 D_{tr}(\phi)\nabla(\phi_1/\phi). \tag{4.2}$$

Under the equilibrium scaling assumption, the above and $\mathbf{J}$ are both zero to leading order. Setting (4.2) to zero, multiplying by $\hat{\mu}$ and using that $\hat{\mu}M_0 = (1 - \phi/\phi_{\max})^{-1}$ (with $\hat{\mu}$ given by the Krieger-Dougherty relation (1.4)) gives

$$|\hat{\mu}\hat{u}_{\hat{z}}|\frac{\mathrm{d}\chi}{\mathrm{d}\hat{z}} = \left(\frac{2(\rho_{p,2} - \rho_{p,1})\cot\alpha}{9\rho_\ell}\right)\frac{\chi(1-\chi)}{D_{tr}(\phi)(1 - \phi/\phi_{\max})}. \tag{4.3}$$

Here $\hat{\mu} = \mu/\mu_\ell$ and hats indicate non-dimensional quantities. Eq. 4.3 along with the familiar equations from the monodisperse problem,

$$\mathbf{J}^{(z)} = 0, \qquad (\hat{\mu}\hat{u}_{\hat{z}})_{\hat{z}} = -\hat{\rho}, \tag{4.4}$$

provides a system of three ODEs in z for u, ϕ, χ, furnishing an equilibrium solution $(\widetilde{u}, \widetilde{\varphi}_1, \widetilde{\varphi}_2)$ analogous to the monodisperse problem (refer to Eq. 1.10) that satisfies

$$u(x,z,t) = h^2\widetilde{u}(z/h; \overline{\varphi}_1, \overline{\varphi}_2), \quad \phi_i(x,z,t) = \widetilde{\varphi}_i(z/h; \overline{\varphi}_1, \overline{\varphi}_2) \tag{4.5}$$

where $\overline{\varphi}_1$ and $\overline{\varphi}_2$ are depth-averaged concentrations of each species, i.e.

$$\overline{\varphi}_i = \frac{1}{h}\int_0^h u\phi_i\,\mathrm{d}z, \qquad i = 1, 2.$$

Integrating the particle transport equations (4.1), keeping only leading order terms in ϵ and applying the boundary conditions as in Section 1.3 yields the system of conservation laws (in non-dimensional variables, dropping hats)

$$0 = h_t + (h^3 f)_x\,, \tag{4.6a}$$

$$0 = (h\overline{\varphi}_1)_t + (h^3 g_1)_x\,, \tag{4.6b}$$

$$0 = (h\overline{\varphi}_2)_t + (h^3 g_2)_x\,, \tag{4.6c}$$

where the fluxes are given by

$$f(\overline{\varphi}_1, \overline{\varphi}_2) = \int_0^1 \widetilde{u}\widetilde{\varphi}\,\mathrm{d}s, \qquad g(\overline{\varphi}_1, \overline{\varphi}_2 = \int_0^1 \widetilde{u}\widetilde{\varphi}_i\,\mathrm{d}s, \quad i = 1, 2$$

and are obtained by solving the equilibrium problem as detailed in the next section. We will analyze these conservations laws in detail in Chapter 5, and focus here on the properties of the equilibrium solution $(\widetilde{u}, \widetilde{\varphi}_1, \widetilde{\varphi}_2)$.

4.2 Equilibrium theory

To obtain the fluxes needed to study the dynamic problem (4.6), we first need to determine the solution (4.5) to the equilibrium problem. As with the monodisperse problem, define a scaled height $s = z/h$ and the scaled shear stress $\sigma = \mu\widetilde{u}_z$. For the remainder of the chapter, we will regard the quantities of interest as functions of s and leave (x, t) fixed; these variables are dropped as well as the tildes since then ϕ and $\widetilde{\varphi}$ do not need to be distinguished. In addition, define the fraction of lighter particles and integrated fraction

$$\overline{\chi} = \overline{\varphi}_1/\overline{\varphi}, \qquad \chi = \phi_1/\overline{\varphi}.$$

It will be convenient to search for solutions (ϕ, χ, σ) rather than the equivalent (u, ϕ_1, ϕ_2). To obtain a useful form of the equations, define the constants

$$\rho_{s,i} = \frac{\rho_{p,i} - \rho_\ell}{\rho_\ell}, \quad B := \frac{2\cot\alpha}{9K_c}, \quad c_t := \frac{2(\rho_{p,2} - \rho_{p,1})\cot\alpha}{9\rho_\ell K_t}, \quad c_v := 2\left(\frac{K_v}{K_c} - 1\right)$$

recalling that the mixing diffusion coefficient $D_{tr}(\phi) = K_t\phi^2$. Simplifying the system (4.3, 4.4) then leads to the ODEs

$$\sigma' = -\rho \tag{4.7a}$$

$$\chi' = c_t \frac{\chi(1-\chi)}{|\sigma|\phi^2(1 - \phi/\phi_{\max})} \tag{4.7b}$$

$$\phi' = \frac{M(\phi, \chi)}{|\sigma|A(\phi)} \tag{4.7c}$$

with $\rho = 1 + \rho_{s,1}\phi\chi + \rho_{s,2}\phi(1-\chi)$ and $M = -B(\rho_{p,1}\chi + \rho_{p,2}(1-\chi))(1-\phi) + \rho\phi$, subject to

$$\int_0^1 \phi\chi\,\mathrm{d}s = \overline{\varphi}\overline{\chi}, \quad \int_0^1 \phi(1-\chi)\,\mathrm{d}s = \overline{\varphi}(1-\overline{\chi}), \quad \sigma(1) = 0.$$

This is a boundary value problem with a region of rapid transition in χ when c_t is not small. Numerical solutions were computed via a straightforward shooting method.

Settled and ridged regimes

As before, we call solutions 'settled' if $\phi(s)$ reaches 0 at some $s < 1$ and 'ridged' otherwise (see Definition 2.2). The critical concentration is now a function but still separates settled and ridged solutions (note that there is no constant solution due to the χ equation):

Definition 4.1. The *critical concentration* $\phi_c(\overline{\chi})$ is (when it exists) the value of ϕ such that, for the ODE (4.7) with $\chi(s) = \overline{\chi}$, the solution for $\phi(s)$ is ridged when $\overline{\varphi} > \phi_c$ and settled when $\overline{\varphi} < \phi_c$.

The monodisperse solutions at their respective critical concentrations, $\chi \equiv 0, \phi \equiv \phi_c(0)$ and $\chi \equiv 1, \phi \equiv \phi_c(1)$ are also solutions to this extended system (4.7) as expected. Because (4.7c) is so similar to its monodisperse counterpart, we also have here that either $\phi(T) = 0$ for some $T < 1$ or $\phi \to \phi_{\max}$ as $s \to 1$ except for the critical solution. The denominator of the χ equation (4.7b) goes to zero as $\phi \to 0$ or $\phi \to \phi_{\max}$. But χ is bounded between 0 and 1 and non-decreasing, so it follows that $\chi(T) = 1$ for settled solutions and $\chi(1) = 1$ for ridged solutions. Physically, this means that the upper portion of the particle layer will contain mostly lighter particles, and that the heavier species will never aggregate at the surface.

It is still desirable, however, to have a sense of when shear-induced migration acts to push the heavier particles upward, counteracting the settling effect (as it does in the single-species problem), even if they never quite reach the surface. Motivated by this, we define some sub-regimes of note within the ridged regime:

a) Ridged A: $\phi_2' < 0$ (heavier particles collect at the substrate; lighter particles move towards the surface),

b) Ridged B: $\phi' > 0$ (solutions are monotonic),

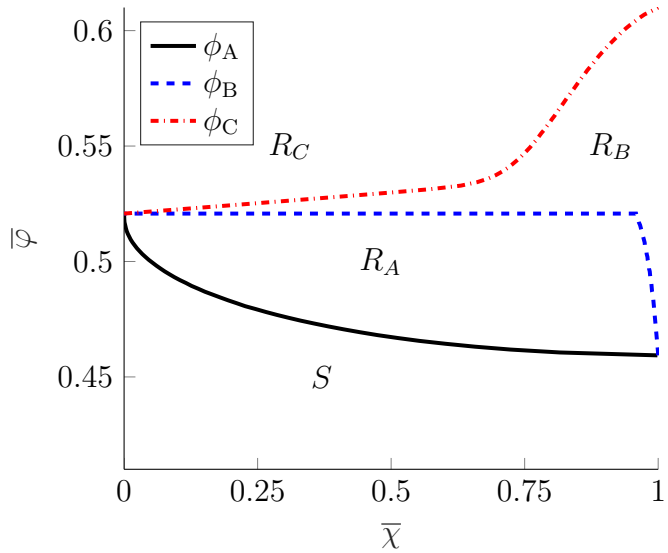

Figure 4.2: Bidensity phase diagram; see Figure 4.3 for solutions in each region. The critical concentration $\phi_A(\overline{\chi})$ separates 'settled' and 'ridged' solutions (above ϕ_A the lighter particles aggregate at the surface).

c) Ridged C: $\phi_2' > 0$ (i.e. the heavier particles are pushed somewhat away from the substrate).

The phase diagram for this is shown in Figure 4.2 and solution profiles in each regime are shown in Figure 4.3. From a physical perspective, regions R_A and R_C differ in that the heavier particles are discouraged from settling in the latter region (above the critical concentration for the heavier particles), so although they do not migrate to the surface, the particles are pushed upwards by the shear-induced migration effect.

4.2.1 Extent of mixing

One can estimate the width w_m of the transition layer (where both particle species are present in significant amounts; defined arbitrarily to be the set $\{s : p \leq \chi(s) \leq 1 - p\}$ with $p = 0.1$) in the limit where $w_m \ll 1$. In this case, the outer solutions on either side of the

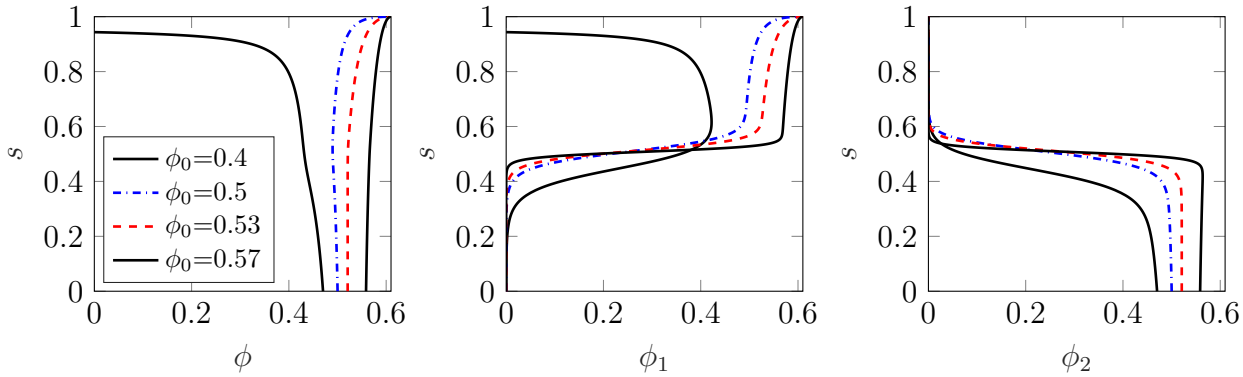

(a) Total ϕ (b) Lighter particles (ϕ_1) (c) Heavier particles (ϕ_2)

Figure 4.3: Bidensity concentration profiles in the regimes S, R_A, R_B and R_C as illustrated in the phase diagam of Figure 4.2.

transition layer are $\chi \equiv 0$ and $\chi \equiv 1$. Within the transition layer, ϕ is constant and so

$$\phi \approx \phi(s^*), \quad \chi \approx 1 - \left[1 + \exp\left(\frac{\phi_{\max} c_t (s - s^*)}{\sigma \phi^2 (\phi_{\max} - \phi)}\right)\right]^{-1} \qquad \text{for } |s - s^*| = O(w_m)$$

where s^* is the center of the transition region and $\sigma \approx \sigma(s^*)$. This gives

$$w_m \approx \frac{\sigma \phi^2 (1 - \phi/\phi_{\max})}{c_t} \ln\left(\frac{1-p}{p}\right). \tag{4.8}$$

with ϕ, σ are evaluated at s^*. In particular, ignoring the effect on $\phi(s^*)$ and $\sigma(s^*)$, the width scales with $\tan\alpha$ (see Figure 4.4) and with the reciprocal of the density difference. Thus our assumption that $w_m \ll 1$ is valid if (estimating $\phi(s^*)$ by the average)

$$9\sigma\overline{\varphi}^2(1 - \overline{\varphi}/\phi_{\max}) K_t \tan\alpha \ll \frac{\rho_{p,1} - \rho_{p,2}}{\rho_\ell}.$$

For typical values ($K_t = 0.4$ and $\overline{\varphi} \approx 0.4$) and experimental parameters (from [LMU14]) the left side is $0.2 \tan\alpha$ and $(\rho_{p,1} - \rho_{p,2})/\rho_\ell \approx 1.3$ so the above is plausible if $\alpha < 45\,\text{deg}$. The particles will tend to separate except at large angles. It is interesting to note that some heavier particles do find their way to the surface (the layer of blue particles in the right panel of Figure 4.1); their presence indicates some effects near the surface that allow the heavier particles to persist there.

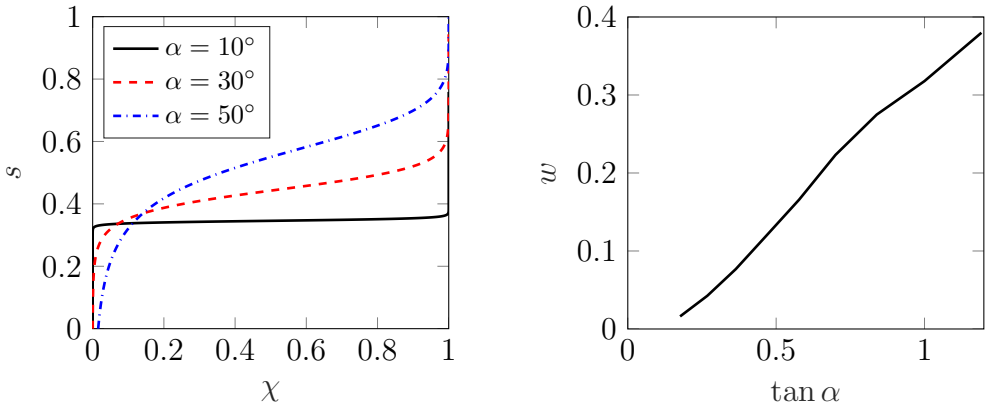

Figure 4.4: Left: Example profiles as a function of angle. Right: the mixing width w right defined in Eq 4.8, showing the nearly linear dependence on $\tan\alpha$.

Note that estimating s^* is not necessary here; one can do so easily in the ridged regime when $w_m \ll 1$ by assuming $\phi \approx \overline{\varphi}$ and taking $s^* \approx \overline{\chi}$. Otherwise, for settled solutions, one would need a better estimate for ϕ (accounting for the fluid layer). If s^* is very close to the edge of the domain then the solution for χ may be different.

4.2.2 Experiments

The bidensity equilibrium exhibits separation of the phases into layers: heavier particles always settle, while the lighter particles either separate from the fluid (leaving a clear layer on top) or migrate up to the surface. For large concentrations, even when shear-induced migration would push the heavier particles to the surface were they the only species, the lighter phase will displace them away. The clearest transition to observe is the one where the lighter particles change from settled to ridged, i.e. the critical concentration $\phi_c(\overline{\chi})$ (the black line in Figure 4.2), which gives us a relatively straightforward point of comparison to experiments (the more subtle behavior, such as the amount of mixing, requires more involved imaging and has not yet been observed experimentally).

As it is easier to adjust inclination angle than concentration, the data used here fixes

a mixture concentration and varies the angle. As with increasing $\overline{\varphi}$, an increase in α has the effect of altering the balance of fluxes to favor shear-induced migration, in this case by reducing the normal component of gravity [MHH11]. The previous discussion applies to the (χ, α) plane as well, and, in particular, there is a critical $\alpha_A(\chi)$, analogous to $\phi_A(\chi)$, separating settled and ridged solutions. The predicted bifurcation is shown in Figure 4.5 along with experimental results from Lee et. al. [LMU14] identifying settled or ridged behavior. Experiments to date have not measured the particle concentrations inside the thin film and thus do not distinguish between different theoretically predicted types of ridged behavior. Overall, the current theory captures the bifurcation curve obtained experimentally, although the critical angles predicted by the model are greater than what is measured in the experiment by about five degrees. This discrepancy can be attributed primarily to the value of the empirical parameter K_c; for the sake of comparison, the curve using K_c as a fitting parameter is shown in the figure. The need to choose a fitting parameter here for such limited data is, of course, not ideal, so it would not be fair to claim the model to have any quantitative value. While we based the value of K_c on prior work [MPP13], the types of beads used in the experiments differ slightly in size and texture from previous work and warrant further experiments to better estimate K_c or to adjust the model in other ways.

4.3 Discussion

Our model predicts bifurcation behavior analogous to that observed for monodisperse suspensions [MHH11] - between 'setttled' and 'ridged' regimes, where the lighter species either settles below the surface or aggregates at the surface. We only compare the model to experiments through this critical value $\phi_c(\overline{\chi})$, which is affected only indirectly by the second species. The distinction between the ridged sub-regimes and the separation between particle species would be interesting to explore in future experiments, which would require more precise experimental techniques to measure the volume concentration of different particle species through the layer.

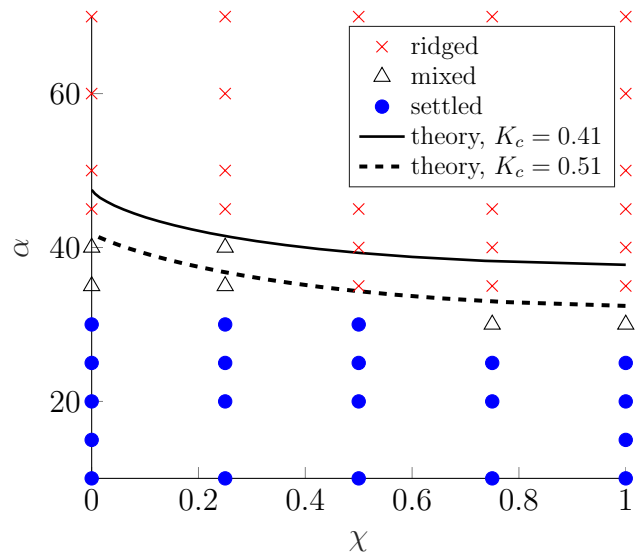

Figure 4.5: Critical concentration $\phi_c(\chi)$ compared to experimental data from [LMU14]. The solid line uses the value $K_c = 0.41$ consistent with prior work [PAB92]. The dashed line shows the theory with K_c as a fitting parameter for the sake of comparison.

This equilibrium theory provides a foundation for many avenues of further inquiry, such as studying polydisperse suspensions (of more than two particle species) or flow in a helical geometry. This is of practical interest in the design of spiral sepators used for extracting valuable materials from slurries. Recently, [LSB14, Arn16] the equilibrium model for monodisperse slurries on an incline has ben transferred to spiral geometries and shown to lead to a variety of interesting phenomena - a corresponding result for polydisperse slurries could be of great utility for understanding the dynamics of spiral separators. More fundamentally, there are ways the model could be improved. We have employed the diffusive flux model to describe particle migration and utilized a simple model for mixing between species within the diffusive flux framework [TA99]. An improved model based on more recent theory, such as the suspension balance model (applied to monodisperse incline flow in Chapter 2), could provide greater insight into the dynamics of bidensity suspensions.

CHAPTER 5

Constant volume and bidensity dynamic theory

In this chapter we study the hyperbolic system derived in Chapter 4 for the bulk flow of a bidensity suspension down an incline. For monodisperse suspensions, prior work has developed the theory for the Riemann problem [MB14, WB14] and the constant-volume problem in the ridged regime ($\phi > \phi_c$) [WMB15]. The main goal of this chapter is to understand how the additional particle type affects shock and rarefaction solutions to the conservation law model, and to show how these solutions can be used to describe the evolution of the particle and fluid fronts observed in experiments. We also complete the analysis of the constant volume problem in the settled regime for monodisperse suspensions, which provides some intuition for the more complicated bidensity problem.

A few basic properties of the fluxes will be assumed. Exact expressions will be difficult to come by since the fluxes are solutions to a boundary value problem without an exact solution; for the most part, the results herein rely only a few key properties and some reasonable assumptions (so they apply equally to the DFM and SBM approaches, for instance). We will for the most part obtain qualitative results (in some case without total rigor). Some results in this chapter will make assumptions based on the numerically computed 'physical' fluxes (which are qualitative rather than rigorous observations) that may not generalize to parameter ranges outside the experimental values of interest.

5.1 Properties of the hyperbolic system

For studying the constant-volume problem (and comparison to the two-species case), we describe some of the basics of the system and state some useful results, reviewing prior work [WB14, WMB15]. Recall that under the equilibrium assumption (1.10), the equations reduce to a first-order system of conservation laws for the film height h and integrated concentration $\psi = h\phi = \int_0^h \phi \, \mathrm{d}z$. For a single particle species, these are (refer to Section 1.3)

$$h_t + (h^3 f(\phi))_x = 0, \tag{5.1a}$$

$$(h\phi)_t + (h^3 g(\phi))_x = 0. \tag{5.1b}$$

The initial conditions are taken to be

$$h(x,0) = \begin{cases} h_L & x < 0, \\ h_R & x > 0 \end{cases} \quad \text{and} \quad \phi(x,0) = \begin{cases} \phi_L & x < 0, \\ \phi_R & x > 0 \end{cases}$$

with $h_L = 1$ for simplicity (this can be done without loss of generality although the symbol h_L will sometimes be used to emphasis). For comparison to physical solutions, of course, h_L will be rescaled appropriately. Defining $U = (h, h\phi)$ and $Q(U) = h^3(f(\phi), g(\phi))$, the system can be written in the general form

$$U_t + (Q(U))_x = 0. \tag{5.2}$$

It will be useful also to define $q = (f, g)$ so that $Q = h^3 q$. The Jacobian is

$$J = h^2 \begin{pmatrix} 3f - \phi f' & f' \\ 3g - \phi g' & g' \end{pmatrix} = h^2 \tilde{J}(\phi) \tag{5.3}$$

with eigenvalues $\lambda_1 = h^2 \Lambda_1(\phi)$, $\lambda_2 = h^2 \Lambda_2(\phi)$ and right eigenvectors r_1, r_2 (which can also be written as functions only of ϕ).

Key assumptions

The fluxes are assumed to have the properties described in Chapter 2 (the limits as $\phi \to 0$ and $\phi \to \phi_{\max}$ are described in the Appendix, Section 6.1). A mixture of concentration

ϕ_M will be referred to as 'settled' if $\phi_M < \phi_c$ and 'ridged' if $\phi_M > \phi_c$. We are particularly interested in the case where ϕ_c is non-trivial, but will also consider the settling-dominated regime where $\phi_c = \phi_{\max}$. A useful characterization of ϕ_c is the following:

Lemma 5.1 (see [WB14])**.** *The critical concentration ϕ_c (when it exists) is the unique value of ϕ in $(0, \phi_{max})$ such that $g(\phi) - \phi f(\phi) = 0$. In particular, $g - \phi f < 0$ for $0 < \phi < \phi_c$ and $g - \phi f > 0$ for $\phi_c < \phi < \phi_{max}$.*

The analysis will require a few additional assumptions as made in [MPP13] (with some adjustments):

Assumption 5.1 (1-species fluxes)**.** The fluxes $f(\phi)$ and $g(\phi)$ in (5.1) satisfy:

i) $f, g \in C^1([0, \phi_{\max}])$

ii) $f' < 0$ for $0 < \phi < \phi_{\max}$

iii) $(g/f)' > 0$ for $0 < \phi < \phi_{\max}$

iv) $(3f + g' - \phi f')^2 > 12 f^2 (g/f)'$ for $\phi_c \leq \phi < \phi_{\max}$.

Condition (i) is only a concern at ϕ_c where solutions jump from settled to ridged; the calculations of f, g near ϕ_c in the Appendix, Section 6.2 verify that (i) should hold. Conditions (ii) and (iii) imply (iv) when $0 < \phi < \phi_c$ so (iv) does not need to be assumed in that range.

Remark. *Condition (iii) is notable in that the system is hyperbolic with positive eigenvalues for $\phi < \phi_c$ if and only if (iii) holds. Unlike the purely technical condition (iv), It has a physical interpretation as well: if $\widetilde{\varphi}(s; \overline{\varphi})$ and $\widetilde{u}(s; \overline{\varphi})$ are the equilibrium particle/velocity profiles given $\int_0^1 \widetilde{\varphi} \, \mathrm{d}s = \overline{\varphi}$ then (iii) says that*

$$\frac{\int_0^1 \widetilde{\varphi}\widetilde{u} \, \mathrm{d}s}{\int_0^1 \widetilde{u} \, \mathrm{d}s} \text{ is increasing in } \overline{\varphi}.$$

Since $\widetilde{u}$ is larger near the surface, the condition should hold if the particle distribution grows more towards the surface as the total concentration is increased. This is indeed true of the equilibrium system we consider here due to the upwards shear-induced migration.

Assumptions (iii) and (iv) are the condition used in [MHH11] to guarantee hyperbolicity; there the significance of (iii) is not noted so their assertion is based purely on numerical calculations. The value of $\Lambda_2(\phi_c)$ is a Lemma in [MWW16] but the inequalities for $\phi \neq \phi_c$ are not included. The assumptions made guarantee the system is strictly hyperbolic and provide some useful bounds for the eigenvalues.

Lemma 5.2. *Under Assumption 5.1, the system* (5.1) *is strictly hyperbolic in* $\{0 < \phi < \phi_{max}\} \cap \{h > 0\}$, *with eigenvalues* $\lambda_1 = h^2\Lambda_1(\phi), \lambda_2 = h^2\Lambda_2(\phi)$ *satisfying*

$$0 < \lambda_1 < \lambda_2.$$

In addition, $\Lambda_2 > 3f$ *for* $\phi < \phi_c$ *and* $\Lambda_2 < 3f$ *for* $\phi > \phi_c$ *and* $\Lambda_2 = 3f$ *at* $\phi = \phi_c$.

Proof. First, the determinant of the scaled Jacobian $\tilde{J}$ (Eq. 5.3) is

$$\det \tilde{J} = 3(g'f - f'g) = 3f^2(g/f)' > 0.$$

Now define the characteristic polynomial $p(\lambda) = \det(\tilde{J} - \lambda I)$ and note that

$$p(3f) = -3f'(g - \phi f).$$

By the assumptions and Lemma 5.1, $3f$ is an eigenvalue exactly at $\phi = \phi_c$. Now p is convex and $\phi < \phi_c$, we have $p(3f) < 0$ which further implies that the eigenvalues are real and $\Lambda_2 > 3f > \Lambda_1$. Since the determinant is positive, $\Lambda_1 > 0$ as well. The technical condition (iv) in Assumption 5.1 directly ensures that the eigenvalues are real and distinct when $\phi \geq \phi_c$, establishing hyperbolicity.

For the second part, the (unique) zero of $\Lambda_2(\phi) - 3f(\phi)$ at ϕ_c has degree one by the above. Since $f, g \in C^1$ the eigenvalue Λ_2 varies continuously, so it must be that $\Lambda_2 < 3f$ for $\phi < \phi_c$. ■

There is one more technical assumption to make (the genuine non-linearity assumption) for considering rarefaction solutions later. The fields are not genuinely non-linear everywhere, i.e. $\nabla\lambda \cdot r$ may equal zero. The best that can be assumed for the physical fluxes is the following:

Assumption 5.2. The fields for (5.1) are (almost) genuinely non-linear in the sense that there exists $\phi_{NL} < \phi_c$ such that

$$\nabla \lambda_k \cdot r_k \neq 0$$

for $k = 1, 2$ in the regions $\{\phi > \phi_c\} \cap \{h > 0\}$ and $\{\phi < \phi_{NL}\} \cap \{h > 0\}$.

Unless otherwise noted, when considering rarefactions we refer to the 'settled' regime as the set $\{\phi < \phi_c\}$ with the understanding that we are really considering $\{\phi < \phi_{NL}\}$ instead and ignoring the exceptional cases that cross the degeneracy. This technical point (not noted in prior work) is only significant when the left and right states lie on opposite sides of ϕ_c and the connecting rarefaction would have to cross ϕ_{NL}, a case that is not explored here.

5.2 Solution types (monodisperse)

Following standard notation [Lax73], a k-shock connecting a left state U_L to a right state U_R with speed s satisfies the Rankine-Hugoniot condition

$$Q(U_L) - Q(U_R) = s(U_L - U_R) \tag{5.4}$$

and the Lax entropy condition

$$\lambda_k(U_L) > s > \lambda_k(U_R), \qquad \lambda_{k-1}(U_L) < s < \lambda_{k+1}(U_R). \tag{5.5}$$

We define the shock set $S^+(U_L)$ to be the set of right states U_R satisfying (5.4) and (5.5) and $S^-(U_R)$ to be the set of left states U_L satisfying the same. Rarefaction solutions $u(x,t) = U(\xi)$ (with $\xi = x/t$) satisfy the ODE

$$U' = \frac{1}{\nabla \lambda_k \cdot r_k} r_k. \tag{5.6}$$

For a given state and k, we define the k-rarefaction curves $R^{\pm}(U) = \{U(\xi) : \pm\xi > 0\}$ (so $R^+(U_L)$ gives the set of right states for which we can construct a rarefaction from U_L to U_R).

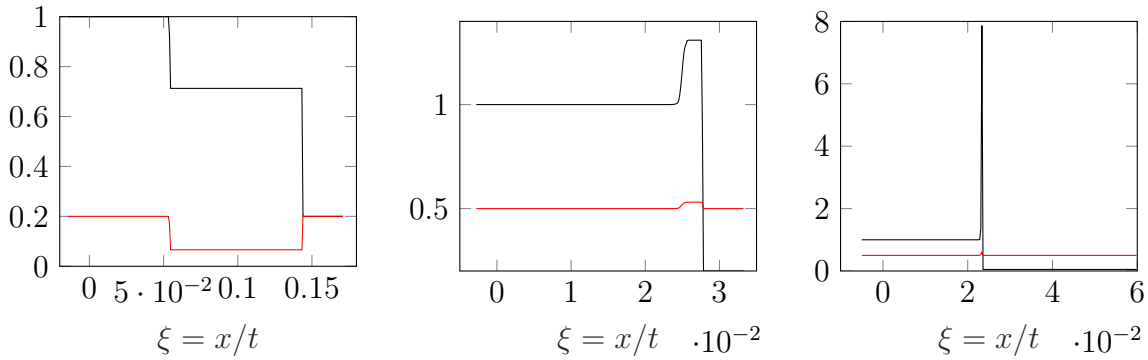

(a) Left to right: Settled, ridged double shock and singular shock solutions.

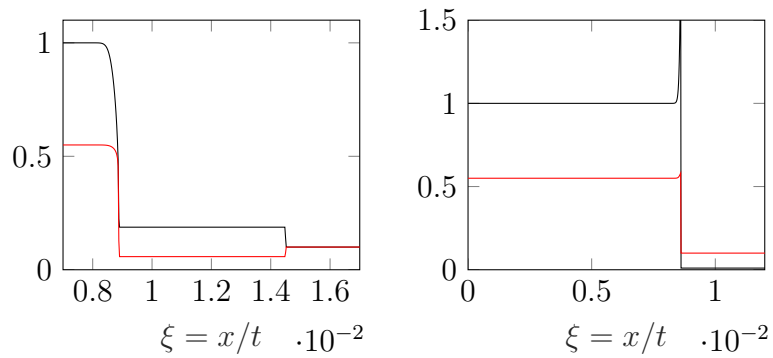

(b) Special cases where $\phi_L > \phi_c > \phi_R$: rarefaction/shock and singular shock solutions.

Figure 5.1: Typical shock solutions for the bidensity Riemann problem. The black/red lines are the height h and integrated particle density ψ.

Shock solutions

To begin we briefly review the typical solutions of interest that arise when $h_L > h_R$ (see [WB14]). There are five types of solutions when $h_L > h_R$, depending on the left/right state concentration and the size of h_R. For certain threshhold values h^* and h^{**} depending on ϕ^L and ϕ^R, the possibilities are:

- Settled ($\phi_L, \phi_R < \phi_c$): a pair of shocks, with an intermediate height $h_I \in [h_R, h_L]$.
- Widening ridge ($\phi_L, \phi_R > \phi_c$, $h_R > h^*$): A pair of shocks with $h_I > h_L, h_R$.
- Singular shock ($\phi_L, \phi_R > \phi_c$, $h_R < h^*$): A singular shock.

- Settled, crossing ϕ_c ($\phi_L > \phi_c$ and $\phi_R < \phi_c$, $h_R > h^{**}$): A rarefaction with $\phi > \phi_c$ followed by a shock, connecting to $h_I < h_L$, then a second shock.

- Ridged-to-settled singular shock ($\phi_L > \phi_c$ and $\phi_R < \phi_c$, $h_R < h^{**}$): A singular shock with a similar structure as in the previous case.

The value of h^* is computed explicitly in [WB14]. The settled crossing case is a rarefaction-shock due to the failure of the general non-linearity condition (see Assumption 5.2). The last two regimes are not explored in earlier work and introduce a new technicality, which we will ignore and leave to future work. Solutions in each case are shown in Figure 5.1. The details of the theory for constructing these solutions can be found in [WB14, MB14].

As discussed in [WB14] for the incline problem, singular shocks are non-classical solutions with delta functions of linearly growing mass added to a shock (first noted in [KK90]). The singular shock satisfies the generalized Rankine-Hugoniot condition

$$F(U_L) - F(U_R) = s(U_L - U_R) + E$$

where $E_2/E_1 = \phi_{\max}$ (if ψ/h is bounded then both h, ψ must be singular). This allows us to solve for the singular shock speed:

$$\frac{h_L^3 g_L - h_r^3 g_R - s(\psi_L - \psi_R)}{h_L^3 f_L - h_R^3 f_R - s(h_L - h_R)} = \phi_{\max} \implies s = \frac{h_L^3(\phi_{\max} f_L - g_L) - h_R^3(\phi_{\max} f_R - g_R)}{h_L(\phi_{\max} - \phi_L) - h_R(\phi_{\max} - \phi_R)}$$

which, incidentally, would be the regular (Rankine-Hugoniot) speed for a solution to

$$(\phi_{\max} h - \psi)_t + (h^3(\phi_{\max} f - g))_x = 0.$$

Interestingly, if we approximate $\phi_{\max} f - g \sim C(\phi_{\max} - \phi)^3$ (from the asymptotics) and set $v = \sqrt{C}(\phi_{\max} h - \psi)$ then the above is the scalar conservation law

$$v_t + (v^3)_x = 0,$$

the same as the height equation for a simple fluid. If $h_R = \psi_R = 0$ then

$$s = h_L^2 \frac{\phi_{\max} f_L - g_L}{\phi_{\max} - \phi_L}.$$

Note that $\phi_{\max} f - g \sim C(\phi_{\max} - \phi)^3$ as $\phi \to \phi_{\max}$ so $s \to 0$ in that limit.

Rarefactions

The rarefaction ODE can written in terms of the scaled eigenvalue $\Lambda(\phi) = h^{-2}\lambda$ using (5.3):

$$h^{-1}\nabla\Lambda \cdot r = (2\lambda - \phi\Lambda', \Lambda') \cdot (-f', 3f - \phi f' - \Lambda) = (3f - \Lambda)\Lambda' - 2\Lambda f'$$

so the rarefaction ODE (5.6), written out explicitly, is

$$h' = \frac{1}{h}\frac{-f'}{(3f-\Lambda)\Lambda' - 2\Lambda f'}, \qquad (h\phi)' = \frac{1}{h}\frac{3f - \phi f' - \Lambda}{(3f-\Lambda)\Lambda' - 2\Lambda f'}. \tag{5.7}$$

Solving for ϕ' gives (using that $\xi = h^2\Lambda$) the scalar ODE

$$\phi'(\xi) = \frac{1}{\xi}\frac{\Lambda(3f-\Lambda)}{(3f-\Lambda)\Lambda' - 2\Lambda f'}. \tag{5.8}$$

By Lemma 5.2 and the genuine nonlinearity condition in Assumption 5.2, solutions to the rarefaction ODE exist for $\phi > \phi_c$ (and do not cross ϕ_c) and also exist for ϕ sufficiently smaller than ϕ_c. Rarefactions arise (in the entropy solution) when $h_L < h_R$, so they are important in the constant volume problem for which the solution is comprised of rarefaction-shock pairs. Solutions in the ridged regime - which are rarefaction-singular shock pairs instead - were studied by Wang et. al. [WMB15]. Here we complete the study of the constant volume by exploring the settled regime, where particle layer and fluid will separate into rarefaction-shocks, and study the long-time behavior of the solutions in detail.

5.3 Constant volume: Asymptotics for front positions

The initial conditions, motivated by parallel experimental work, are a finite reservoir of a suspension of uniform concentration ϕ_M:

$$h(x,0) = h_p + (1-h_p)\mathbb{I}_{[0,1]}(x), \qquad \psi(x,0) = \phi_M h(x,0)$$

where $\mathbb{I}_S$ is the indicator function for the set S. The height can be taken to be 1 without loss of generality; the width is taken to be 1 for simplicity. Here h_p is the height of the precursor layer; for the bulk flow in the settled regime, this value is not particularly important and

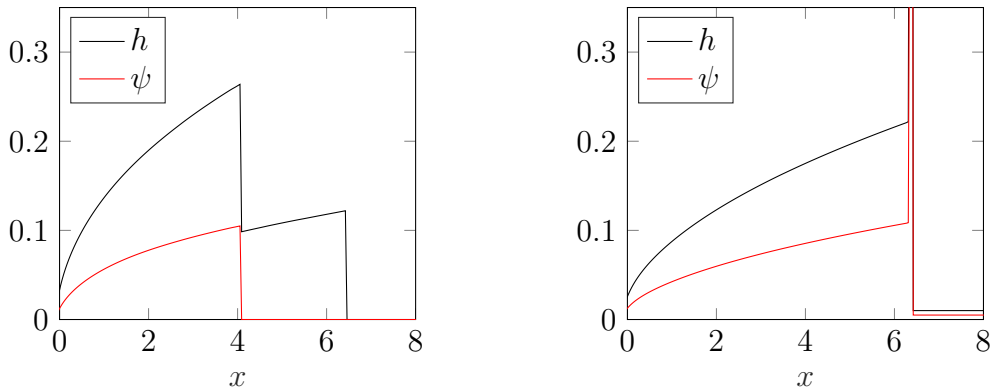

(a) Settled: $\alpha = 30\,\text{deg}, \phi_M = 0.3$.

(b) Ridged: $\alpha = 30\,\text{deg}, \phi_M = 0.5$.

Figure 5.2: Typical constant volume solutions for the monodisperse equations (5.1).

thus it is taken to be zero. Since we take $h_p = 0$, the value of ϕ outside the reservoir is not significant either (and is set to be constant over the whole domain). Typical solutions (including $\phi > \phi_c$ for comparison) are shown in Figure 5.2.

In this section we will denote by $\Lambda(\phi)$ the scaled larger eigenvalue of the Jacobian (previously Λ_2 in Lemma 5.2); the other eigenvalue will not be useful so it is convenient to drop the subscript here. Let $x_p(t)$ and $x_f(t)$ be the position of the particle fronts (i.e. the first point to the right of zero where $\psi = 0$ or $h = 0$, respectively). Assume also that as $\phi \to \phi_{\max}$, the fluxes satisfy

$$\phi f - g \sim \frac{b}{6}(\phi_{\max} - \phi)^3 + O((\phi_{\max} - \phi)^4) \tag{5.9}$$

$$f \sim \frac{a}{2}(\phi_{\max} - \phi)^2 + O((\phi_{\max} - \phi)^3) \tag{5.10}$$

(the values of a and b for the DFM are computed in Section 6.1). Note that other than this and the existence of ϕ_c, the details of the model are not particularly important to the derivation. The main result is the following:

Claim 5.3 (Convergence to ϕ_c)**.** *With the above assumptions, if the inclination angle is not too small, there is a constant η with $0 < \eta < 1/2$ depending on the equilibrium parameters such that the following holds:*

Define the constant

$$\gamma = \begin{cases} 1/3 & \phi_c < \phi_{max} \\ \frac{1-2\eta}{3-2\eta} & \phi_c = \phi_{max} \end{cases}$$

The concentration satisfies

$$\max_{x\in[0,x_p(t)]} |\phi(x,t) - \phi_c| \sim ct^{-\eta(1-\gamma)}$$

as $t \to \infty$ *and the front positions are*

$$x_f(t) \sim (c_f t)^{1/3} + O(t^{1/3-\eta(1-\gamma)}), \qquad x_p \sim (c_p t)^{\gamma} + O(t^{\gamma-\eta(1-\gamma)}).$$

With $A_p := \frac{1}{6f(\phi_c)}$, *the fluid constant is*

$$c_f = \frac{9}{4}\left(1 - \frac{\phi_M}{\phi_c}(1-\sqrt{2A_p})\right)^2$$

and if $\phi_c < \phi_{max}$ *then the particle constant is* $c_p = \frac{9\phi_M^2}{4A_p\phi_c^2}$.

The constant η is not specified above but can be computed explicitly from the equilibrium theory (formulas are noted in the discussion below). Plots of η and γ as a function of angle are shown in Figure 5.4 for typical experimental parameters. Note that the above yields an explicit approximate solution (h_0, ϕ_0) by using the leading term for x_p, x_f and setting $\phi \equiv \phi_c$ for $x < x_p$, given by

$$h_0(x,t) = \begin{cases} \sqrt{A_p x/t} & x < x_p(t) \\ \sqrt{2x/t} & x_p(t) < x < x_f(t) \\ 0 & x > x_f(t) \end{cases}, \qquad \phi_0(x,t) = \begin{cases} \phi_c & x < x_p(t) \\ 0 & x > x_p(t) \end{cases} \tag{5.11}$$

with $x_p = (c_p t)^{1/3}$ and $x_f = (c_f t)^{1/3}$. Plots of the approximation vs. numerical solution at different times are shown for a typical solution in Figure 5.3. For the limiting solution above, the constants c_f, c_p given in the claim are obtained easily from the particle and fluid conservation equations

$$\phi_M = t\int_0^{x_p(t)/t} h(\xi)\phi(\xi)\,\mathrm{d}\xi, \tag{5.12}$$

$$1 = t\int_0^{x_p(t)/t} h(\xi)\,\mathrm{d}\xi + t\int_{x_p(t)/t}^{x_f(t)/t} \sqrt{\xi}\,\mathrm{d}\xi \tag{5.13}$$

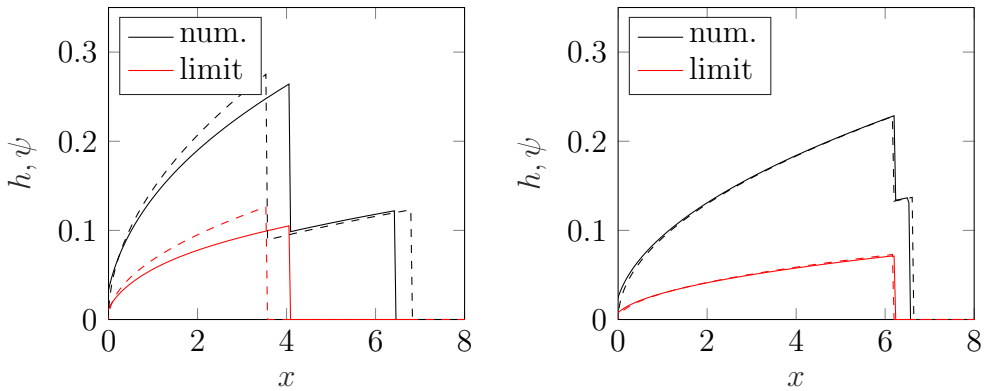

(a) $\alpha = 30\,\text{deg}$. (b) $\alpha = 50\,\text{deg}$.

Figure 5.3: Leading order approximation (5.11) (dashed line) to the monodisperse constant volume problem compared to the numerical solution at $t = 350$.

which we will also use to obtain the next-order corrections for x_p and x_f. To do so, we must first determine an approximation to the concentration $\phi(\xi)$ and then use it to obtain an expression for the height $h(\xi)$.

Linearization, $\phi_c < \phi_{\mathbf{max}}$

To show the claim, we linearize the ODE (5.8) about ϕ_c. Assume

$$\phi(\xi) = \phi_c + p(\xi)$$

where p is uniformly small for sufficiently small ξ. Defining $R(\phi) = \phi f - g$, the scaled eigenvalue Λ from is (from the Jacobian (5.3))

$$\Lambda = 3f - \frac{R' + 2f}{2} + \frac{1}{2}\sqrt{(R' + 2f)^2 - 12f'R}$$

and so to leading order,

$$\Lambda - 3f = -3f'(\phi_c)\frac{R'(\phi_c)}{R'(\phi_c) + 2f(\phi_c)}p + O(p^2).$$

The linearization of (5.8) is then

$$p' = \eta\frac{p}{\xi} + O(p^2) \qquad \text{with } \eta := -\frac{3}{2}\frac{R'(\phi_c)}{R'(\phi_c) + 2f(\phi_c)}. \tag{5.14}$$

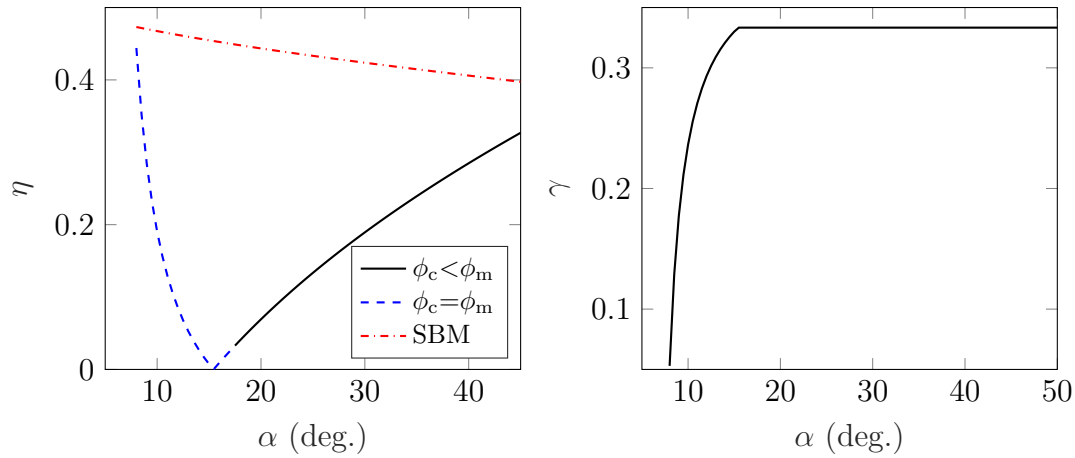

Figure 5.4: Exponents η and γ from Theorem 5.3 as a function of angle, with η given by (5.15) when $\phi_c < \phi_{\max}$ (black, solid) and (5.17) when $\phi_c = \phi_{\max}$ (blue, dashed). The corresponding values of η for the SBM are shown in red; here $\phi_c < \phi_{\max}$ for all values shown so there is only one branch.

It follows that

$$\phi \sim \phi_c + K_p \xi^\eta$$

for a constant K_p. This constant would be determined by the constraint $\phi(1) = \phi_M$; this is problematic since the ODE is only tractable to solve near $\phi = \phi_c$. We do, however, have the simple approximation $K_p \approx \phi_M - \phi_c$ (a more refined approximation is not pursued here).

Because the concentration profile is constant at the critical value in the equilibrium problem, the value of η can be computed in terms of the physical parameters (see Eq. (6.5) in the Appendix). The result is

$$\eta = -\frac{\nu}{2(2-\nu)}, \qquad \nu := \frac{1 + 2\rho_s\phi_c + B\rho}{(1 + c_v \frac{\phi_{\max}}{\phi_{\max}-\phi_c})(1+\rho_s\phi_c)} \tag{5.15}$$

for the DFM and the same form for the SBM with a different value of ν (see (6.5) for details). Notably, $\eta \to 0$ as $\phi_c \to \phi_{\max}$ since then $\nu \to 0$, so the particle concentration will converge more slowly as ϕ_c increases (or as the inclination angle decreases).

Linearization, $\phi_c = \phi_{\max}$

The calculation is the same, except that the fluxes near $\phi_{\max}$ now satisfy (5.9). The eigenvalue satisfies

$$\Lambda = \left(\frac{3a}{2} - \frac{b}{2}\right) p^2 + \cdots$$

assuming that $b/2 < a$ (one can check from the calculations in Section 6.1 that the physical fluxes always satisfy this condition, so it is safe to assume). This leads to the linearization

$$p' = \eta \frac{p}{\xi}, \qquad \eta := -\frac{b}{4a - 2b} \tag{5.16}$$

with solution $\phi \sim \phi_{\max} - K_p \xi^\eta$ as before. The exponent η can again be written in terms of physical parameters via the equilibrium theory using Lemma 6.2:

$$\eta = -\frac{\nu}{2(2+\nu)}, \qquad \nu := \frac{\phi_{\max}(1 + \rho_s \phi_{\max}) + B(\phi_{\max} - 1)}{c_v \phi_{\max}(1 + \rho_s \phi_{\max})} \tag{5.17}$$

for the DFM. Despite the somewhat different asymptotics near $\phi_{\max}$, the calculation for the SBM is similar using Lemma 6.3; the assumption (5.9) on f, g is replaced by

$$\phi f - g \sim b p^{7/2}, \qquad f \sim a p^{5/2}$$

which leads to the same ODE but with

$$\eta = -\frac{d}{5d/2 - 5a}, \qquad d = -\frac{c}{2} + \frac{1}{2}\sqrt{c^2 - 30ab}$$

and $c = 7b/2 + 5a$. If the values from the Lemma are used ($a = b$) then one obtains $d = a$ as well and so $\eta = 2/15$ is constant and independent of physical parameters.

Front positions, $\phi_c < \phi_{\max}$

We obtain the height profile by expanding $h^2 \Lambda = \xi$ to first order in p using (5.14):

$$h(\xi) = \frac{\xi^{1/2}}{\sqrt{\Lambda(\phi_c)}} - \frac{K_p \Lambda'(\phi_c)}{2\lambda(\phi_c)^{3/2}} \xi^{1/2+\eta} + O(p^2).$$

The particle conservation equation (5.12), keeping the first two terms, is

$$\phi_M = t \int_0^{x_p(t)/t} \frac{\phi_c}{\Lambda(\phi_c)} \xi^{1/2} + K_1 \xi^{1/2+\eta} \, \mathrm{d}\xi + \cdots$$

where $K_1 = \frac{K_p}{\sqrt{\Lambda(\phi_c)}}\left(\frac{3f(\phi_c)-g'(\phi_c)}{R'(\phi_c)+2f(\phi_c)}\right)$. This yields the desired expression for the particle front:

$$x_p(t) \sim (c_p t)^{1/3} + c_{1,p} t^{\frac{1-2\eta}{3}}, \qquad C_{1,p} := -K_1 \frac{\sqrt{3f(\phi_c)} C_p^{(1+\eta)/3}}{\phi_c(\eta + 3/2)}.$$

The fluid front, from fluid conservation (5.13), is then

$$x_f(t) \sim (c_f t)^{1/3} + O(t^{(1-2\eta)/3})$$

and in particular the ratio of the front positions is

$$x_p/x_f \sim (C_p/C_f)^{1/3} + O(t^{-2\eta/3}).$$

The leading order behavior is unaffected by the exponent η (the fronts both evolve like $\sim Ct^{1/3}$), but the value of η tells us how fast the solution converges to this limiting behavior. If η is close to 0, then the convergence will be quite slow, so the critical approximation is only a good one when ϕ_c is not too close to $\phi_{\max}$ (for instance, in Figure 5.3, the leading order solution is quite close for $\alpha = 50\,\text{deg}$ but not as good for $\alpha = 50\,\text{deg}$).

Front positions, $\phi_c = \phi_{\max}$

Because the denominator of the rarefaction ODE (5.8) vanishes at $\phi_{\max}$, the asymptotic behavior of h is now different:

$$h = \frac{\sqrt{\xi}}{\sqrt{\Lambda}} \sim \frac{1}{|K_p|\sqrt{3b/2 - a/2}} \xi^{1/2-\eta}.$$

The square-root shape of the rarefaction is therefore deflected somewhat as $\xi \to 0$. Solving for the leading order behavior from particle conservation (5.12), we obtain

$$x_p(t) \sim (C_p' t)^{\gamma} + \cdots, \qquad \gamma := \frac{1-2\eta}{3-2\eta}$$

for a constant C_p'. However, by fluid conservation (5.13), the fluid front position still satisfies

$$x_f(t) \sim (C_f t)^{1/3} + \cdots$$

which implies that $x_p/x_f \to 0$ as $t \to \infty$. This phenomenon is similar to the predictions of the model in the high-concentration (ridged regime), where singular shock solutions have a

single front whose position scales like $x(t) \sim Ct^{\gamma}$ with $\gamma < 1/3$ [WMB15]. The slowdown there is due to mass accumulation at the singular shock; here it is due to mass accumulation (to $\phi_{\max}$) near the position of the reservoir.

Curiously, the approximation is only valid when $\eta < 1/2$, which is not satisfied automatically. In fact, for the DFM, for very small angles, η may reach 1/2 (e.g. $\alpha \approx 7°$ for typical experimental parameters and using the DFM). For the SBM, we had that $\eta = 2/15$ when $\phi_c = \phi_{\max}$ (and consequently $\gamma = 11/41 \approx 1/4$). The inconsistencies suggest a different analysis would have to be conducted to explore the system in this regime; because the model is dubious at asymptotically small angles anyway, we leave the shallow-angle case to future investigation.

5.4 Riemann problem: bidensity system

The second main result of this chapter is a (qualitative) description of the Riemann problem for the bidensity model, in the spirit of the analysis carried out for the monodisperse case [MB14, WB14]. Recall from Chapter 4 that the equations describing the bulk flow are

$$h_t + (h^3 f(\phi, \overline{\chi}))_x = 0 \tag{5.18a}$$

$$(h\phi_1)_t + (h^3 g_1(\phi, \overline{\chi}))_x = 0 \tag{5.18b}$$

$$(h\phi_2)_t + (h^3 g_2(\phi, \overline{\chi}))_x = 0 \tag{5.18c}$$

with $\phi = \phi_1 + \phi_2$ and $\overline{\chi} = \phi_1/\phi$. One could also write the fluxes f, g_1 and g_2 in terms of ϕ_1 and ϕ_2 but using $\overline{\chi}$ turns out to be more useful.

Remark 5.1. *It is important to note that in* (5.1) *and* (5.18) *the conserved variables are* $(h, h\phi)$ *and* $(h, h\phi_1, h\phi_2)$, *respectively. However, due to the dependence of the fluxes on* ϕ *it is often convenient to show solutions in terms of the non-conserved variables* (h, ϕ) *or* $(h, \phi, \overline{\chi})$. *In this chapter, we will often switch between the two.*

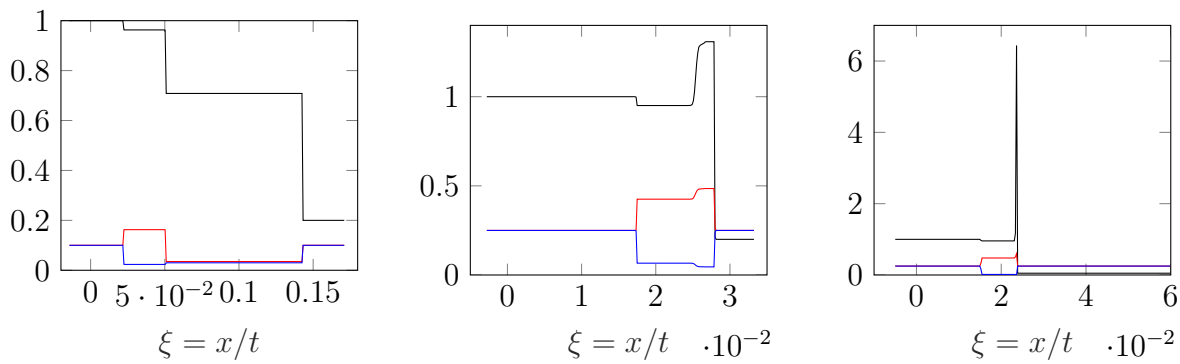

Figure 5.5: Typical shock solutions for the bidensity Riemann problem; settled triple shock (left), ridged triple shock (center) and ridged singular shock (right) when h_R is small enough. The black line is the film height h and the blue/red lines are the integrated heavier/lighter particle densities ψ_2, ψ_1.

The initial conditions are

$$h(x,0) = \begin{cases} h_L & x < 0 \\ h_R & x > 0 \end{cases}, \qquad \psi_i(x,0) = \begin{cases} \psi_{i,L} & x < 0 \\ \psi_{i,R} & x > 0 \end{cases}.$$

for $i = 1, 2$. We could also write the above in terms of $\phi_{L,R}$ and $\overline{\chi}_{L,R}$. Denote by U a state (h, ψ_1, ψ_2) and $\tilde{U}$ the same state in the form $(h, \phi, \overline{\chi})$.

For simplicity, we will focus (mostly) the case where $\chi_L = \chi_R$ and $\phi_L = \phi_R$ (which is enough to illustrate the main structures that appear in solutions). In addition, without loss of generality we take $h_L = 1$. The shock solutions of interest still fall into the categories of the first three regimes of the previous section (again, ignoring the other cases), now with the addition of a shock containing a jump in the concentration ϕ_2 of the heavier species. Some solutions in each of the cases are shown in Figure 5.5.

The Jacobian of the flux $Q = h^3 q$ with $q = q(\phi, \chi) = (f, g_1, g_2)$ is (written by column)

$$J = h^2 \left(3q - \phi q_\phi \middle| q_\phi + \tfrac{1-\chi}{\phi} q_\chi \middle| q_\phi - \tfrac{\chi}{\phi} q_\chi . \right) \tag{5.19}$$

If χ is constant then the problem reduces to the monodisperse case with effective particle density parameter $\rho_s = \chi\rho_{s,1} + (1-\chi)\rho_{s,2}$. We cannot find a nice expression for the eigenvalues. However, there is one useful observation that will help to guide the study of the system:

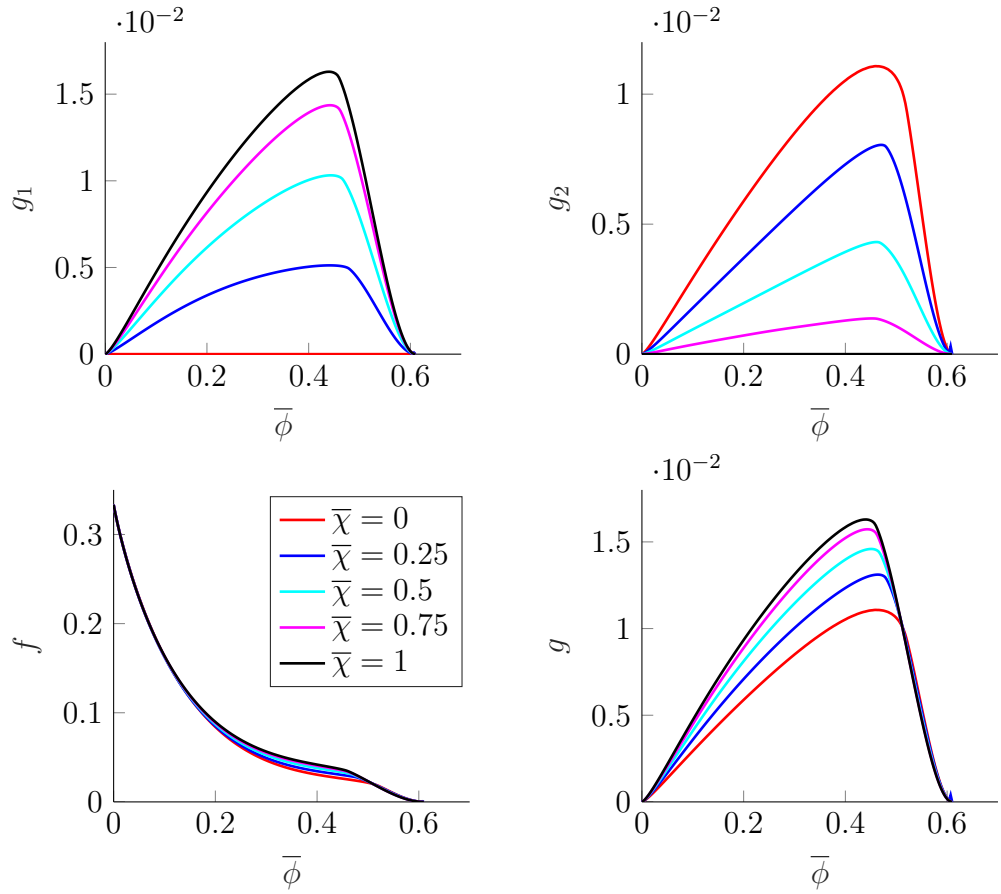

Figure 5.6: Bidensity fluxes for $\alpha = 30°$ as a function of ϕ for various values of χ, showing the fluid flux, total particle flux, and flux of the lighter/heavier particles (f, g, g_1 and g_2 respectively). Note that f, g are insensitive to changes in χ.

Claim 5.4. *The fluxes f, g can be reasonably approximated by functions only of ϕ.*

Plots of the fluxes f (fluid) and g_i (particle i), along with $g = g_1 + g_2$, are shown in Figure 5.6 as functions of ϕ and χ. As can be seen, the fluid flux f is insensitive to changes in χ; it only varies a small amount up to moderate ϕ and is nearly constant in χ for when $\phi > \phi_c(0)$, the critical concentration for the heavier particles from the monodisperse theory [MHH11]. Similarly, the total particle flux g is nearly constant in χ for $\phi > \phi_c(0)$ as well, although it varies considerably with X below this threshold (as do the fluxes for each species).

For the fluxes of the equilibrium model, we can look at $\frac{\partial f}{\partial \chi}$ in more detail to try to

understand why it tends to be small, although are more precise estimate is currently lacking. Consider a solution $(\widetilde{\varphi}, \tilde{\chi}, \tilde{\sigma})$ to (4.7) with a given total concentration ϕ and $\overline{\chi}$. The density difference $\Delta\rho$ is not small, so one might expect there to be a significant dependence on ρ. According to the equilibrium theory (as a consequence of the equation for χ In the system) the ODE for $\tilde{\chi}$), the particle layers are mostly stratified in equilibrium, so we can approximate

$$\tilde{\chi}(s) = \begin{cases} 0 & s < s_t \\ 1 & s > s_t \end{cases}$$

for some transition point s_t (past which there are no heavier particles). The change in shear stress with χ is then

$$\frac{d\tilde{\sigma}}{d\chi}(s) = \begin{cases} (\rho_1 - \rho_2)\phi & s < s_t \\ 0 & s > s_t \end{cases}.$$

The change in f is given by the expression

$$\frac{\partial f}{\partial \chi} = -\Delta\rho\phi \int_0^{s_t} (1-s)\left(1 - \frac{\widetilde{\varphi}(s)}{\phi_{\max}}\right)^2 ds - \frac{2}{\phi_{\max}} \int_0^1 (1-s)\left(1 - \frac{\widetilde{\varphi}}{\phi_{\max}}\right) \sigma \frac{\partial \widetilde{\varphi}}{\partial \chi}\, \mathrm{d}s.$$

The first term is due to the change in shear stress and is negative. The second term represents the change in f due to the concentration profile change (which affects the viscosity). The sign of $\frac{\partial \phi}{\partial \tilde{\chi}}$ is negative for $s < s_t$ (an increase in the number of lighter particles will lead to a smaller total concentration near the substrate). While neither term is particularly small in general, they tend to oppose each other. In the ridged regime, where ϕ is increasing, we expect $\frac{\partial f}{\partial \tilde{\chi}}$ to be small (as is evident in Figure 5.6) because μ^{-1} and $d(\mu^{-1})/d\phi$ will both be small by to the viscosity relation.

Shocks

Our main claim is an extension of the monodisperse result, with the addition of an extra shock ahead of the other two:

Claim 5.5. *If $h_R < 1$ and $0 < \chi_L < 1$ then there is an h^* (depending on $\phi_{L,R}$ and $\chi_{L,R}$) such that if $h_R > h^*$ then a classical (weak) solution exists (satisfying the Lax entropy condition)*

as a sequence of three shocks

$$U_0 \to U_1 \to U_2 \to U_3$$

with $U_L = U_0$ *and* $U_3 = U_R$*. For* $h_R < h^*$*, the solution is instead a shock from* U_0 *to* U_1 *followed by a singular shock connecting* U_1 *to* U_R *with the same structure as in the monodisperse case. In addition*

i) If ϕ_L, ϕ_R *are in the ridged regime then* $h_1, h_2 > h_L, h_R$ *and* $\phi_1, \phi_2 > \phi_L$ *(i.e. the intermediate states form a ridge with high concentration).*

ii) If ϕ_L, ϕ_R *are in the settled regime then* $h_L > h_1, h_2$ *and* $\phi_1, \phi_2 < \phi_L$ *(i.e. the particles and fluid separate in the intermediate state).*

Rather than prove this rigorously, we will study the Riemann problem qualitatively and argue that it should be the case (note that as in prior work, we do not prove that a singular shock exists, but rather show that a classical solution does not exist and demonstrate its presence numerically. The key assumption we make to simplyify the problem is the following:

Claim 5.6. *The shock curves* S_2^+ *and* S_3^+ *are only weakly dependent on* χ*.*

This is due to the assumption that f, g do not depend much on χ as addressed in Claim 5.4. For the Riemann problem, we only need the fluxes to be 'weakly dependent' enough that the shapes, projected onto the (h, ϕ) plane, are similar to their monodisperse counterparts. We then find that S_1^+ provides the jump in χ and the remaining two shocks have a similar structure to the monodisperse case. The following detailed discussion is adapted from published work in [WB16].

First shock

We consider now in detail the 1-shock for the bidisperse system. Exact results for the solutions are somewhat difficult to obtain due not only to the equilibrium ODE, but also to the three-equation system, so we rely on numerically computed shock curves to construct

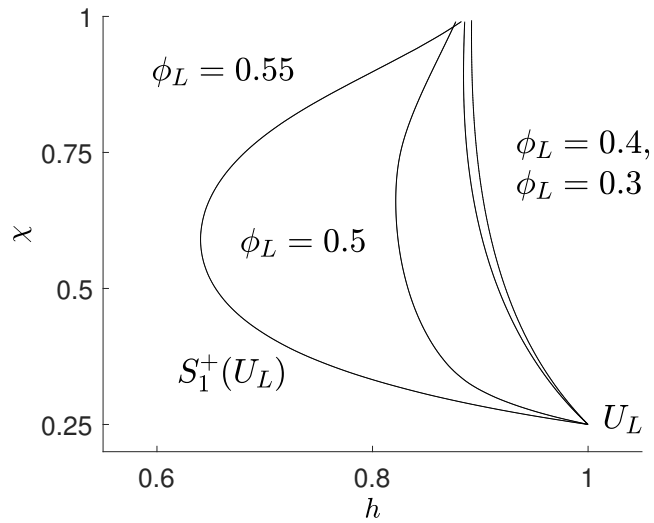

Figure 5.7: 1-shock curves for initial states (h_L, ϕ_L, χ_L) with h_L fixed, $\chi_L = 0.5$ and varying ϕ_L in the (h, ϕ, χ) phase plane.

the solution. A family of numerically computed shock curves S_1^+ with different left-state concentrations ϕ_L are shown in Figure 5.7. To a good approximation, the curve for small ϕ_L represents a jump only in χ, with h and ϕ constant. There is only a small variation in h (representing a small downward jump in film height that can be seen in Figure 5.5). Note that the admissible states $U^{(1)}$ along the shock curve have $\chi > \chi_L$, an increase in the concentration of lighter particles. Physically, this represents the lighter particles and fluid separating from the slower front of heavier particles which lags behind while keeping the total concentration across the jump approximately constant. However, as evident in Figure 5.7, there is some variation in h, which is quite prominent as ϕ_L becomes large. When $\chi \neq 0$, the curve S_1^+ will never be exactly parallel to the X axis. This can be seen by noting that $U = (0, 1, -1)$ in conserved variables points in the χ-direction and is a right eigenvector of the Jacobian of (5.19) only if $\frac{\partial f}{\partial \chi}$ and $\frac{\partial g}{\partial \chi}$ are both zero (the case in which there is only one particle species). While $\frac{\partial f}{\partial \chi}$ is small (see Figure 5.6), the same is not true of the latter, so the 1-shock curve cannot only be a jump in χ and must have some change in h or ϕ.

Interestingly, the deviation in the h (and ϕ) directions increases considerably near and beyond the critical concentration. This can be seen by assuming a formal expansion $h =$

$h_L + h_1 + \cdots$, $\phi = \phi_L + \cdots$ with $h_1 \ll h_L$ where $h_1 \ll h_L$ and the ellipses indicate higher order terms. In this case the Rankine-Hugoniot condition gives an estimate for the shock speed:

$$\frac{s}{h_L^2} \approx \frac{1}{\phi_L} \frac{g_1(\phi_L, \chi) - g_1(\phi_L, \chi_L)}{\chi - \chi_L}. \tag{5.20}$$

Notably, g_1 is approximately quadratic in χ, which implies that s scales almost linearly with the proportion of lighter particles. Solving for h_1 gives the simple approximation

$$\frac{h_1}{h_L} \approx \frac{1}{3} \frac{(\phi f - g)\big|_{\chi_L}^{\chi}}{(\phi f - g)|_{\chi_L}},$$

so h_1 depends on the jump in $\phi f - g$ from the left to right state. The effect can be seen in Figure 4 (plotting the 1-curve for varying ϕ_L and fixed $\chi_L = 0.5, h_L = 1$). As ϕ_L comes close to the ridged regime, the shock curves begin to bend considerably in h due to a large relative change in $\phi f - g$ (which is zero in the transition from settled to ridged).

Second and third shocks

Next, we consider the structure of the remaining two shocks. This is made straightforward by projecting onto the (h, ϕ) plane. To construct a solution, we look at the surface of intermediate states $U^{(2)}$ that lie on 2-shock curves S_2^+ emanating from states $U^{(1)} \in S_1^+(U^L)$. The desired solution is then obtained by intersecting the 3-curve $S_3^-(U^R)$ with this surface, which is shown in Figure 5.8). We also show the non-entropy half S_2^- of the 2-curves for later comparison with the ridged regime.

If the left state lies in the settled regime, S_2^+ connects states $U^{(1)} \in S_1^+ U_L$ to a second intermediate state with a smaller height and total concentration. If ϕ_R is small (or χ_R is large), i.e. there are few heavy particles downstream, then χ_1 must be near one, so that the last intermediate state U_2 has $\phi_{0,2}$ sufficiently small (note that $\phi_{0,2} \to 0$ as $\chi_1 \to 1$).

To complete the solution, we look at the 3-curve; we see that so long as χ_R is not too large, the 3-curve will indeed intersect the surface. From the (h, ϕ) projection (see Figure 5.8), it is clear that (h_R, ϕ_R) is required to be within a certain region, in agreement with the

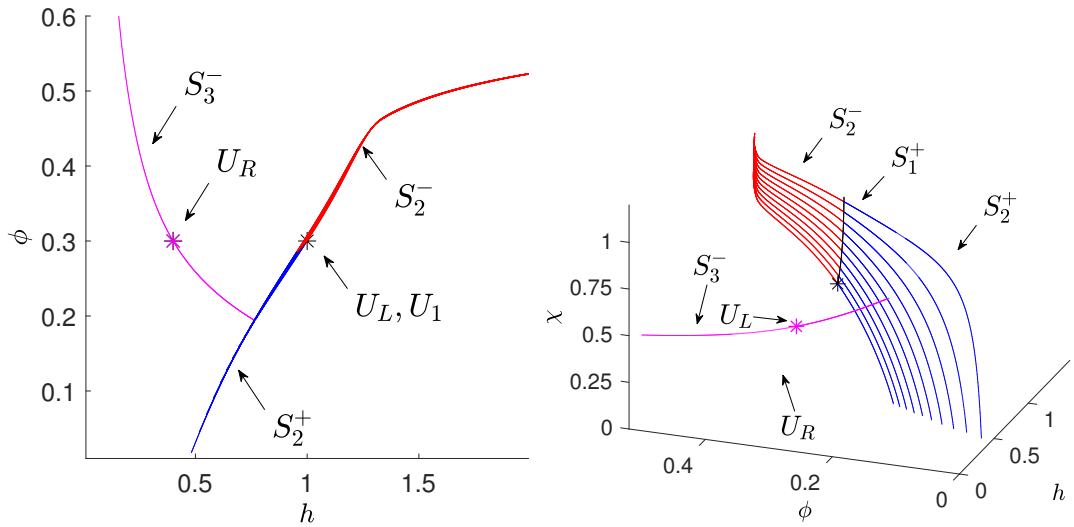

Figure 5.8: Bidensity Riemann problem for the settled regime, showing the 2-shock connections $\cup_{U \in S_1^+(U_L)} S_2^+(U)$ from a given given left state and connection to right state. The left panel shows the projection onto (h, ϕ) (note that the S_2 curves collapse to nearly a single curve).

monodisperse theory [MB14]. If (h_R, ϕ_R) lies outside this region, then the 3-connection is instead a rarefaction.

In the case of a ridged left state, the 2-curves satisfying the entropy condition (5.5) instead have h increasing rather than decreasing; the change in sign of $\phi f - g$ changes which branch of the 2-curve satisfies the entropy condition (this is illustrated in Figure 5.8, where both S_2^- and S_2^+ are shown). The structure of the curves is somewhat more interesting (see [WB14]) and the asymptotic form is known in the limit as $\phi \to \phi_{\max}$. The shock curves are shown in Figure 5.9 (right). As ϕ increases, the value of h_L increases and diverges to ∞, and for sufficiently large ϕ, the 2 and 3− curves no longer intersect as $h \to \infty$, which leads to a singular shock. The monodisperse theory applies in this context because the curves in the bidisperse problem collapse almost exactly onto the (h, ϕ) plane. Again, as in the settled case, the 2-curves form a surface in the (ϕ, χ) plane, so that the existence of an intersection (h^*, ϕ^*) in the (h, ϕ) plane implies there exists some state U_1 (by choosing the appropriate χ_1) such that this is actually an intersection in the full three-dimensional system. Also, we

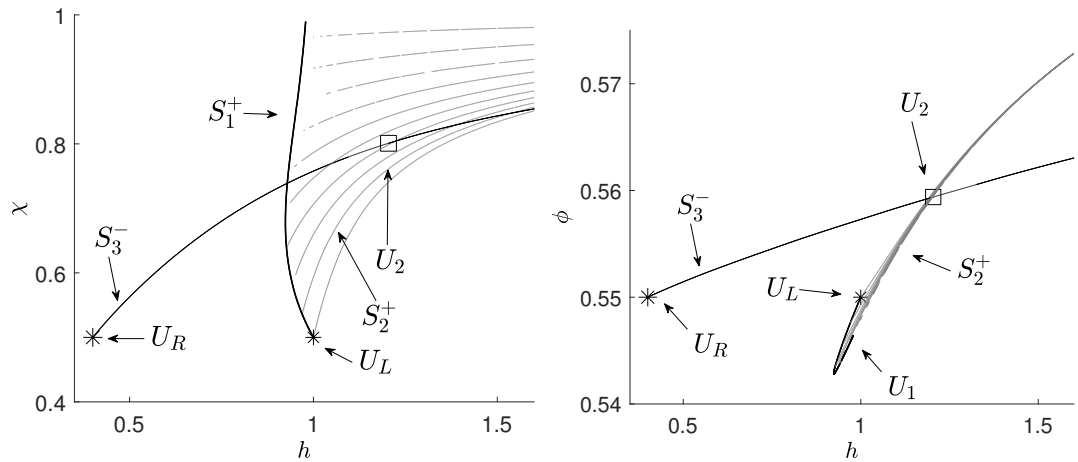

Figure 5.9: Bidensity Riemann problem for the ridged regime illustrating the construction of a solution with three shocks; the shock curves are shown projected onto (h, χ) (left) and (h, ϕ) (right).

can see that $\chi \to 1$ as $\phi \to \phi_{\max}$ for the 2 and 3-curves; this implies that only lighter particles aggregate at the singular 'front' (to be expected due to the increased tendency to settle of the heavier particles discussed in Chapter 4).

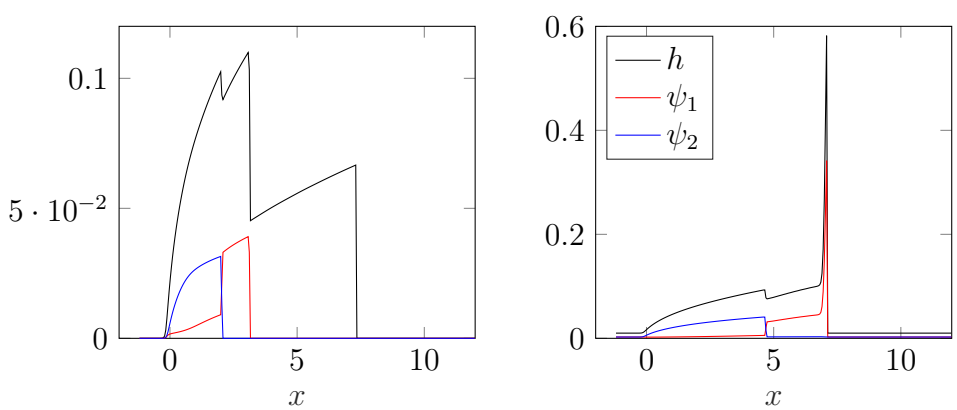

Figure 5.10: Examples of constant volume, bidensity solutions.

5.5 Constant volume: bidensity system

With the basic structure of the shocks determined, we can proceed to studying the constant volume problem and show that a similar separation of particle types occurs. The initial conditions are similar to the monodisperse case:

$$h(x,0) = h_p + (1-h_p)\mathbb{I}_{[0,1]}(x), \qquad \psi_i(x,0) = \phi_{M,i}h(x,0), \text{ for } i = 1,2.$$

Example solutions are shown in Figure 5.10. Let $\phi_M = \phi_{M,1} + \phi_{M,2}$ and $\chi_M = \phi_{M,1}/\phi_M$ as well. Also let $x_{p,i}$ and x_f be the particle fronts for species i and the fluid. Let $\phi_{c,1} = \phi_c(1)$ and $\phi_{c,2} = \phi_c(0)$ be the critical concentrations when there are only lighter/heavier particles, respectively. The main claim is that

Claim 5.7 (Approximate solution, bidisperse)**.** *For $\phi_M < \phi_{c,1}, \phi_{c,2}$ the solution is a sequence of three rarefaction/shocks with front positions $x_{p,2}, x_{p,1}$ and x_f. The solution has $\psi = 0$ for $x > x_{p,1}$ (i.e. no particles) and*

$$\phi \to \phi_c(0), \quad \chi \to 0 \text{ in } [0, x_{p,2}]$$

and

$$\phi \to \phi_c(1), \quad \chi \to 1 \text{ in } [x_{p,2}, x_{p,1}]$$

uniformly as $t \to \infty$. The front $x_f \sim c_f t^{1/3}$ and if $\phi_c(0) < \phi_{max}$ then $x_{p,i} \sim c_{p,i}t^{1/3}$ for constants $c_{p,i}$.

The approximate solution is now

$$h_0(x,t) = \begin{cases} \sqrt{A_{p,2}x/t} & x < x_{p,2}(t) \\ \sqrt{A_{p,1}x/t} & x_{p,2}(t) < x < x_{p,1}(t) \\ \sqrt{2x/t} & x_{p,1}(t) < x < x_f(t) \\ 0 & x > x_f(t) \end{cases} \tag{5.21}$$

with $A_1 = \frac{1}{6f(\phi_{c,1},1)}$, $A_2 = \frac{1}{6f(\phi_{c,2},0)}$ and $\phi \equiv \phi_c(0)$ or $\phi \equiv \phi_c(1)$ in the appropriate regions. By enforcing conservation, the constants for the front positions are

$$
\begin{aligned}
c_{p,1} &= \frac{9\phi_{M,1}^2}{8A_1\phi_{c,1}^2}\left(1 + \frac{\phi_{c,1}}{\phi_{c,2}}\sqrt{\frac{A_1}{A_2}}\frac{(1-\chi_M)}{\chi_M}\right)^2 \\
c_{p,2} &= \frac{9\phi_{M,2}^2}{8A_2\phi_{c,2}^2} \\
c_f &= \frac{9}{4}\left(1 - \sum_{i=1}^{2}\frac{\phi_{M,i}}{\phi_{c,i}}(1-(2A_i)^{-1/2})\right)^2
\end{aligned}
$$

where $\phi_{c,1} = \phi_c(1)$ and $\phi_{c,2} = \phi_c(0)$. The ratio of the front positions between the particle species is predicted to approach a constant:

$$
\lim_{t\to\infty}\frac{x_{p,2}(t)}{x_{p,1}(t)} = \left(1 + \frac{\chi_M}{1-\chi_M}\frac{\phi_{c,2}}{\phi_{c,1}}\sqrt{\frac{f(\phi_{c,1},1)}{f(\phi_{c,2},0)}}\right)^{-2/3}.
$$

recalling that we have written the flux $f = f(\phi,\chi)$. As in the monodisperse case, if $\phi_{c,i} = \phi_{\max}$ then the behavior is expected to be different (with the ratio approaching zero). Unfortunately, the convergence rate is much slower than in the monodisperse case; in addition the added complexity of the equations (e.g. there is no nice ODE for ϕ) makes obtaining a precise asymptotic result more difficult. Some numerical results and the limiting approximation are shown in Figure 5.11.

5.6 Comparison to experiments

Because it is difficult to reproduce the Riemann initial conditions, experiments testing this model have instead focused on the case of fixed volume initial conditions. Previous experimental investigations have explored the transition between settled and ridged regimes [LMU14], testing the equilibrium theory for the bidensity model. Here we present a qualitative comparison of the predicted front positions to the dynamic model to experiments, the details of which can be found in [MLB14]. Because the experiments begin with a well-mixed suspension, some time is required for equilibrium to be reached. This introduces a parameter t^*, the time at which the particles reach their equilibrium state. While an estimate can be

obtained from a scaling argument, we estimate t^* directly, essentially using it as a fitting parameter. The suspension is evolved as well mixed until t^*, (which is within the range of 20 to 40 seconds) and the equilibrium model is used thereafter. A more thorough understanding of the transient phase would be necessary to obtain both a better comparison, and is of interest for future work.

A series of plots comparing the front positions are shown in Figure 5.12. Solutions to (5.18) were computed numerically using an upwind scheme, with the fluxes pre-computed from the equilibrium equations (4.7). As expected, the three fronts can be observed in the experimental data, and the speed of the fronts is greater for larger angles and concentrations. The fluid front is predicted reasonably well. However, the model appears to somewhat under-predict the particle fronts in most cases, particularly for larger angles where the transient phase is expected to be longer. This may be particularly true for multiple species, as the two types of particles must separate from each other as well as from the fluid. While t^* is estimated to be on the order of one minute (so we would hope the model compares well over most of the data), a second transient time might be much later. A suspension that remains partly mixed would behave differently, and for instance might explain the increased speed of the observed front of heavier particles.

5.7 Discussion

In the constant-volume case, we have derived the asymptotic behavior of the front positions for the monodisperse model in the settled regime and applied this to find the leading order behavior for bidisperse suspensions. The front positions are shown to evolve as $t^{1/3}$ except at small angles, where the concentration approaches the maximum packing fraction in the rarefaction and ratio of particle to fluid fronts tends to zero. The slow rate of convergence, however presents a significant challenge for experimental comparison, as the time scale at which the asymptotic behavior becomes dominant is large (perhaps prohibitively so) except at large angles $\alpha \approx 40\,\mathrm{deg}$). It would be interesting, though, to see if this transition or

asymptotic rate of convergence could be observed in experiments. Since the suspension balance model predicts rather different rates of convergence than the diffusive flux model (as illustrated in Figure 5.4), it may provide a way to distinguish between the otherwise similar models.

Motivated by experiments, we have considered constant-volume solutions in the settled regime, which correspond to experiments where a fixed volume of a mixture is released down the incline. In the model, solutions are three rarefaction-shock pairs with mostly heavier particles, then lighter particles, then clear fluid. Preliminary comparison to experimental data shows reasonable qualitative agreement; the general structure of three shocks separating the two particle species and the fluid front is observed in the settled regime, but the front positions are consistently under-predicted by the model. Because the model relies on the assumption that particles are in equilibrium, it cannot be compared to the experimental data at early to moderate times where the suspension may still be partly mixed. A model appropriate to the transient phase may be necessary to better understand the system at early times, and make comparison easier at later times when the model should be applicable. The discrepancies between the current bidisperse model and experiments seem to suggest that the model could be improved; a long transient time due to mixing between the two species is a significant concern. Relaxing the equilibrium assumption leads to a more complicated set of PDEs with an additional spatial dimension and both hyperbolic (in the x-direction) and parabolic (in the z-direction) structure, which is could be a challenging problem to study for future work.

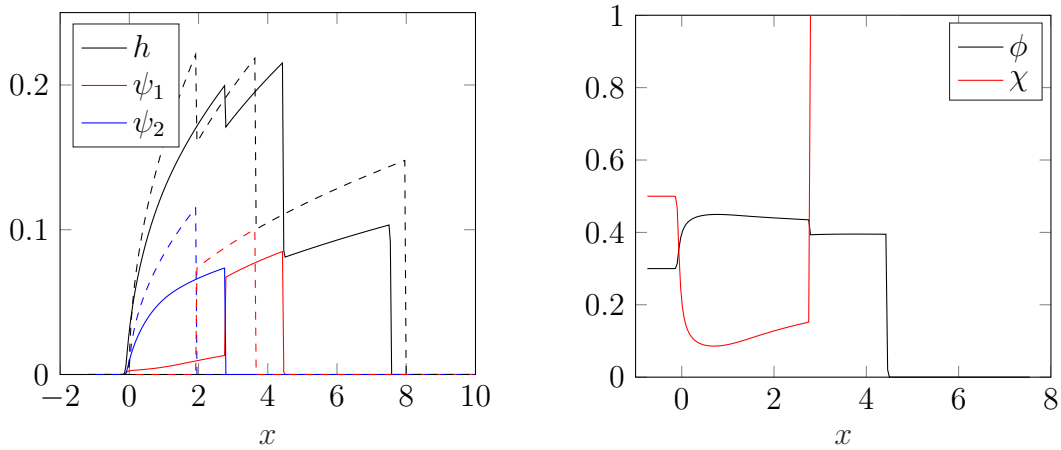

(a) $\alpha = 30\,\mathrm{deg}$

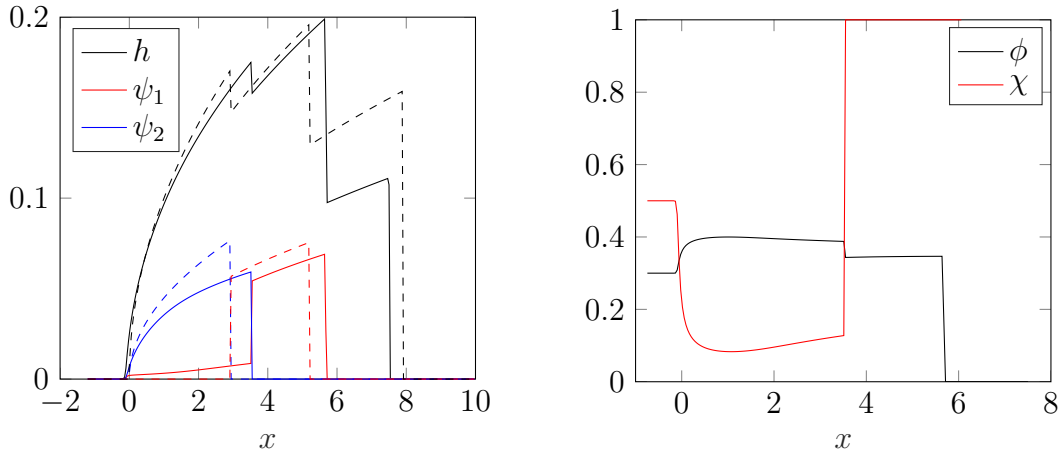

(b) $\alpha = 40\,\mathrm{deg}$

Figure 5.11: Examples of constant volume, bidensity solutions with $\phi_{M,1} = \phi_{M,2} = 0.15$ compared to the proposed limiting solution (5.21) (dashed lines) at $t = 600$. On the right, ϕ and χ; note that they are approximately piecewise constant.

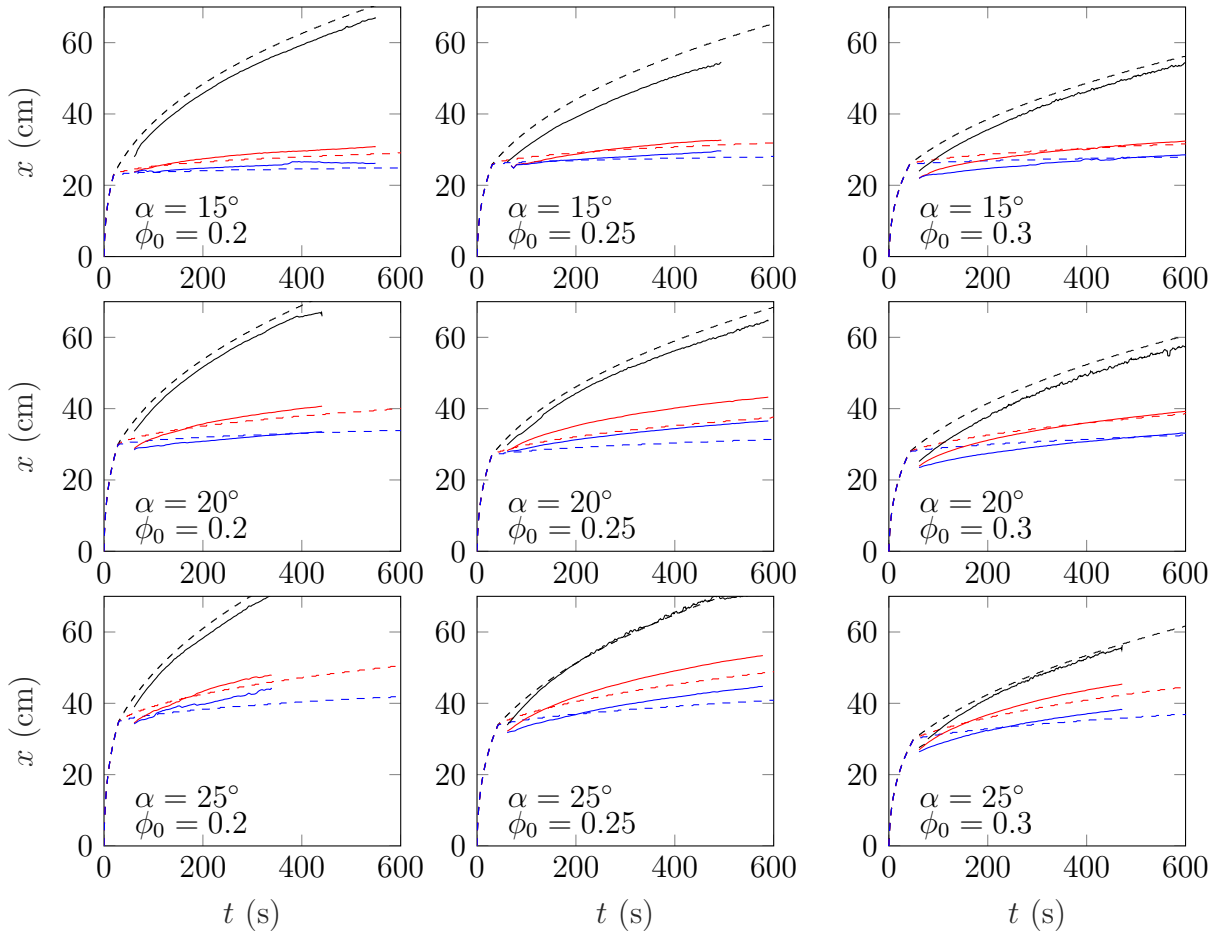

Figure 5.12: Comparison of measured (solid) to numerically computed (dashed) front positions for the bidensity problem. The heavier/lighter particle fronts $x_{p,2}, x_{p,1}$ are blue/red and the fluid front x_f is in black. Simulations were run for a mixed fluid up to a time t^* used as a fitting parameter.

CHAPTER 6

Appendix

6.1 Dilute/packed limits of particle and fluid fluxes

The fluxes f_i, g_i defined in (3.7) and the gravity flux g_{grav} from (3.9) (DFM) and Remark 6.1 (SBM) do not have a closed form as they depend on the equilibrium solution $\phi(s)$. We can, however, derive expressions for the fluxes in the dilute limit ($\phi \to 0$) and in the packed limit ($\phi \to \phi_{\max}$) and at the critical concentration ϕ_c. These calculations are useful for various calculations throughout.

Note that for the simpler model of previous work (i.e. the fluxes f_0 and g_0), these limits are derived in [MPP13] and [WB14], respectively. The derivation presented here is somewhat different and includes the new fluxes as well as the corresponding results for the suspension balance model. The viscosity is assumed to obey

$$\mu(\phi) \sim \begin{cases} 1 + m\phi & \text{as } \phi \to 0 \\ \frac{1}{c_m}\left(\phi_{\max} - \phi\right)^{-2} & \text{as } \phi \to \phi_{\max} \end{cases}$$

for constants m and c_m, e.g. $m = \frac{2}{\phi_m}$ and $c_m = \phi_{\max}^{-2}$ for the Krieger-Dougherty model (1.4). The analytical value of $m = 5/2$ [Ein06] could also be used instead. The approximations computed in this section are the following:

Lemma 6.1 (Dilute limit, DFM or SBM)**.** *The fluxes* (3.7) *have the following behavior as* $\phi \to 0$*:*

$$f_i(\phi) \sim \frac{1}{3} - m\phi, \qquad i = 0, 1, 2$$

$$g_i(\phi) \sim \frac{2^{1/2}}{3\tilde{B}^{1/2}}\phi^{3/2}, \qquad i = 0, 1, 2$$

$$f_3 \sim \frac{\beta}{3\tilde{B}}\phi, \qquad g_3 \sim \frac{\beta}{5\tilde{B}}\phi^2$$

with $\tilde{B} = -\lim_{\phi\to 0} M(\phi)/A(\phi)$ *(either* $\tilde{B} = B$ *for the DFM or* $\tilde{B} = B\phi_m^2/2K_n$ *for the SBM). The gravity flux is either*

$$g_{grav} \sim \frac{2\beta}{9}\phi, \qquad or \qquad g_{grav} \sim \frac{2^{3/2}m}{9\tilde{B}^{1/2}}\phi^{1/2}$$

in the DFM/SBM cases, respectively .

Lemma 6.2 (Packed limit, DFM)**.** *For the DFM, the fluxes satisfy*

$$f_i(\phi) \sim c_m a_i(\phi_{max} - \phi)^2, \qquad g_i \sim \phi f_i + c_m b_i(\phi_{max} - \phi)^3$$

as $\phi \to \phi_{max}$*. Setting* $K := \frac{M(\phi_{max})}{c_v\phi_{max}(1+\beta\phi_{max})}$*, the constants are*

$$a_0 = \frac{(1+\beta\phi_{max})(K+1)^2}{2K+3}, \quad a_1 = \frac{a_0}{1+\beta\phi_{max}}, \quad a_3 = \frac{\beta(K+1)^2}{(K+2)(3K+4)}$$

and $a_2 = a_0 - \phi_{max}a_3$ *along with*

$$b_0 = \frac{K(K+1)(1+\beta\phi_{max})}{3(2K+3)}, \quad b_1 = \frac{b_0}{1+\beta\phi_{max}}, \quad b_3 = \frac{\beta K(K+1)}{4(K+2)(3K+4)}$$

and $b_2 = b_0 - \phi_{max}b_3$*. If* $\phi_{max} > 3/8$*, the constants are strictly positive. In addition,*

$$g_{grav} \sim \frac{2\beta}{9}c_m(1-\phi_{max})\frac{(K+1)^2}{2K+1}(\phi_{max} - \phi)^2.$$

Lemma 6.3 (Packed limit, SBM)**.** *For the SBM, the fluxes satisfy*

$$f_i(\phi) \sim a_i(\phi_{max} - \phi)^{5/2}, \qquad g_i \sim \phi f_i + b_i(\phi_{max} - \phi)^{7/2}$$

as $\phi \to \phi_{max}$ *for constants* $a_i, b_i > 0$ *where in particular*

$$a_0 = b_0 = K^{1/2}\frac{2^{3/2}c_m(1+\beta\phi_m)}{3}$$

with $K = M(\phi_{max})/((1+\beta\phi_{max})A(\phi_m))$*.*

Dilute limit, $\phi \to 0$ (DFM or SBM)

The approach here is adapted from [MPP13]. The solution for very small ϕ is a thin settled layer near $s = 0$. Assume the (regular) expansion

$$\phi = \epsilon^{1/2}\phi_1 + \epsilon\phi_2 + \cdots, \qquad \sigma = 1 - s + \epsilon\sigma_1 + \cdots$$

solving (2.14) with $\phi = \epsilon$ and $\epsilon \ll 1$. Set $\epsilon^{1/2}S = s$. Then where $S = O(1)$,

$$\frac{\mathrm{d}\sigma_1}{\mathrm{d}S} = -\beta\phi_1 \tag{6.1}$$

$$\frac{\mathrm{d}\phi_1}{\mathrm{d}S} = -B + O(\epsilon^{1/2}) \tag{6.2}$$

for the DFM. In the SBM case, instead note that $M \sim -B\phi$ and $A \sim 2K_n\phi/\phi_m^2$ as $\phi \to 0$ so B can be replaced by $B\phi_m^2/2K_n$ and the derivation is the same. The boundary conditions require $\sigma_1(0) = \beta$ and $\epsilon^{1/2}\int \phi_1 \,\mathrm{d}s = \epsilon$. Solving for ϕ_1 and σ_1, we obtain

$$\phi = B(T - s)_+ + O(\epsilon), \qquad T := \sqrt{\frac{2\epsilon}{B}}, \tag{6.3a}$$

$$\sigma = 1 - s + \beta\left(\epsilon - \frac{B(T-s)_+^2}{2}\right) + O(\epsilon^{3/2}) \tag{6.3b}$$

where $(x)_+ = \max\{x, 0\}$. From here one can compute the various integrals and fluxes. First compute

$$\begin{aligned} I_0 &= \int_0^s \mu(\phi)^{-1}\sigma \,\mathrm{d}\tau \\ &= \int_0^s (1 - m\phi + O(\epsilon))(1 - \tau + O(\epsilon)) \,\mathrm{d}\tau + O(\epsilon^{3/2}) \\ &= \frac{1}{2}(1 - (1-s)^2) - m\int_0^s B(T-\tau)_+ \,\mathrm{d}\tau + O(\epsilon^{3/2}) \end{aligned}$$

noting that $1 - \tau = 1 - O(\epsilon^{1/2})$ when $\tau < T$. This gives

$$f_0(\epsilon) = \int_0^1 I_0 \,\mathrm{d}s = \frac{1}{3} - m\epsilon + O(\epsilon^{3/2}).$$

By a similar calculation,

$$g_0(\epsilon) = \int_0^1 \phi I_0 \,\mathrm{d}s = \int_0^T B(T-s)s \,\mathrm{d}s + O(\epsilon^2) = \frac{2^{3/2}}{6B^{1/2}}\epsilon^{3/2} + O(\epsilon^2).$$

The calculations for the other fluxes are similar. It is enough to compute the auxiliary integrals in (3.6); the rest is straightforward. We have

$$I_1 = \int_0^s \mu^{-1}(1-\tau)\,\mathrm{d}\tau = \int_0^s (1-m\phi)(1-\tau)\,\mathrm{d}\tau = I_0(s) + O(\epsilon)$$

with I_0 as given earlier, so the dilute limit of I_1 is the same as I_0 to leading order. The integral I_2 requires more work. To leading order,

$$\begin{aligned}\int_s^1 \left(\tau\phi + \int_\tau^1 \phi(\tau')\,\mathrm{d}\tau'\right)\mathrm{d}\tau &= B\int_s^1 \left(\tau(T-\tau)_+ + \frac{1}{2}(T-\tau)_+^2\right)\mathrm{d}\tau \\ &= B\left(\frac{T^3}{6} - \frac{T}{2}s^2 + \frac{1}{3}s^3\right)_+ + \frac{B}{6}(T-s)_+^3\end{aligned}$$

which yields (taking $\mu^{-1} = 1 + O(\epsilon^{1/2})$)

$$\frac{I_2(s)}{B\beta} = \frac{1}{24}\left(T^4 - (T-s)_+^4\right) + \frac{T^4}{12} - \left(\frac{T^4}{12} - \left(\frac{sT^3}{6} - \frac{Ts^3}{6} + \frac{1}{12}s^4\right)\right)_+.$$

When integrating from 0 to 1, the dominant contribution is from the T^4 terms that do not vanish for $s > T$, so

$$\int_0^1 I_2\,\mathrm{d}s = \frac{B\beta}{8}T^4 + O(\epsilon^{5/2})$$

and

$$\int_0^1 \phi I_2\,\mathrm{d}s \sim B^2\beta\int_0^T \frac{T^4}{8}(T-s)\,\mathrm{d}s = \frac{B^2\beta}{16}T^6 + O(\epsilon^{7/2}).$$

Now recall that $f_2 = \int_0^1 (I_1 + I_2)\,\mathrm{d}s - \phi f_3$ and $g_2 = \int_0^1 (\phi I_1 + \phi I_2)\,\mathrm{d}s - \phi g_3$. The effect of the I_2 term on f_2 and g_2 only enters at $O(\epsilon^2)$ and $O(\epsilon^3)$, respectively, so it can be omitted in deriving the leading-order behavior.

The last integral, I_3, requires differentiating ϕ with respect to $\phi = \epsilon$:

$$\frac{\partial\phi}{\partial\epsilon}(s) = B\frac{\partial T}{\partial\epsilon}\mathbb{I}_{\{s<T\}} = T^{-1}\mathbb{I}_{\{s<T\}}$$

and so

$$I_3 = \beta\int_0^s (1 - m\phi + \cdots)\frac{1}{2T}(T-\tau)_+^2\,\mathrm{d}\tau$$

from which f_3, g_3 are easily computed to give the results in 6.1:

$$f_3 = \beta\int_0^1 \frac{T^2}{6}\,\mathrm{d}s + O(T^3) \sim \frac{\beta T^2}{6}$$

and

$$g_3 = \frac{B}{6\beta}\int_0^T T^2(T-s) - T^{-1}(T-s)^4\,\mathrm{d}s + O(\epsilon^{5/2}) \sim \frac{B}{20\beta}T^4.$$

Since $f_h(\phi) \sim 1$ to leading order, the extra gravity flux (with h scaled out) is simply

$$g_{grav} = \frac{2\beta}{9}\int_0^1 \phi f_h(\phi)\,\mathrm{d}s = \frac{2\beta}{9}\epsilon + O(\epsilon^{3/2}).$$

In the SBM case, the flux (see Remark 6.1) includes $u_{ss}+1$, which satisfies

$$u_{ss} + 1 = (\sigma/\mu)_s + 1 \sim \frac{\mu-1}{\mu} - \frac{\mu'}{\mu^2}(1-s)\phi_s + \cdots .$$

Using $\mu \sim 1 - m\phi$ and the solutions for σ, ϕ:

$$u_{ss} + 1 = m\phi - m(1-s)\phi_s + O(\epsilon)$$

This gives $g_{grav} \sim \frac{2}{9}m\sqrt{2/B}\epsilon^{1/2}$. Note that the $m\phi$ term contributes an $O(\epsilon)$ sized quantity and is omitted here. The dependence on β would show up at the $O(\epsilon)$ level.

Packed limit, $\phi \to \phi_{\mathbf{max}}$ (DFM)

In this limit we instead consider solutions for $\phi = \phi_{\max} - \epsilon$ with $\epsilon \ll 1$. The approach is adapted from [WB14] (with some differences in the derivation). Assume the expansions

$$\phi \sim \phi_{\max} - \epsilon\phi_1 - \epsilon^2\phi_2 + \cdots, \qquad \sigma \sim \sigma_0 + \epsilon\sigma_1 + \cdots$$

and substitute to obtain the leading order equations

$$\sigma_0' = -(1+\beta\phi_{\max})$$
$$\phi_1' = \frac{M(\phi_{\max})}{\sigma_0 c_v \phi_{\max}}\phi_1$$

Solving the above with $\sigma_0(1) = 0$ and $\int_0^1 \phi_1 = 1$, we get $\sigma_0 = \rho_m(1-s)$ and

$$\phi_1 = (K+1)(1-s)^K, \qquad K := \frac{M(\phi_{\max})}{c_v\phi_{\max}\rho_m} \tag{6.4}$$

where $\rho_m = 1 + \beta\phi_m$ (the maximum density). Then

$$I_0(s) \sim \int_0^s \mu^{-1}(\phi)\sigma\,\mathrm{d}\tau = \epsilon^2 c_m\rho_m\int_0^s \phi_1^2(1-\tau)\,\mathrm{d}\tau = \epsilon^2\frac{c_m\rho_m(K+1)^2}{2K+2}\Big(1-(1-s)^{2K+2}\Big)$$

and, verifying the result in [WB14], the fluxes f_0, g_0 are given by

$$f_0(\phi_{\max} - \epsilon) = \int_0^1 u \, \mathrm{d}s = \epsilon^2 \frac{c_m \rho_m (K+1)^2}{2K+3} + O(\epsilon^3)$$

$$g_0(\phi_{\max} - \epsilon) = \int_0^1 \phi u \, \mathrm{d}s = \phi_{\max} f(\phi_{\max} - \epsilon) + O(\epsilon^3)$$

The remainder of the fluxes are computed in the same way. We have

$$I_1 \sim c_m \epsilon^2 \int_0^s \phi_1^2 (1-\tau) \, \mathrm{d}\tau$$

which is exactly I_0 to leading order, yielding $f_1 \sim f_0/\rho_m$ and $g_1 \sim g_0/\rho_m$. For I_2, the integral greatly simplifies to leading order:

$$\frac{I_2}{\beta c_m \epsilon^2} \sim \phi_{\max} \int_0^s \phi_1^2 (1-\tau) \, \mathrm{d}\tau$$

so $I_2 = \beta \phi_{\max} I_1$ which will be used for f_2 later. For I_3, note that $\frac{\partial \phi}{\partial \phi} = -\frac{\partial \phi}{\partial \epsilon} = \phi_1$ and

$$\int_s^1 \int_{s'}^1 (K+1)(1-\tau)^K \, \mathrm{d}\tau \, \mathrm{d}s' = \frac{1}{K+2}(1-s)^{K+2}$$

which leads to

$$\frac{I_3(s)}{\beta c_m \epsilon^2} = \frac{(K+1)^2}{K+2} \int_0^s (1-\tau)^{3K+2} \, \mathrm{d}\tau = \frac{(K+1)^2}{(K+2)(3K+3)} \left(1 - (1-s)^{3K+3}\right),$$

$$f_3(\phi_{\max} - \epsilon) \sim \beta c_m \epsilon^2 \frac{(K+1)^2}{(K+2)(3K+4)}.$$

Finally, f_2 is computing by looking at $\int (I_1 + I_2) \, \mathrm{d}s - \phi_{\max} f_3$:

$$f_2(\phi_{\max} - \epsilon) \sim \epsilon^2 c_m (K+1)^2 \left(\frac{1 + \beta \phi_{\max}}{2K+3} - \frac{\beta}{(K+2)(3K+4)} \right).$$

Because $\frac{3}{8}(K+2)(3K+4) \geq 2K+3$ for $K > 0$, the above coefficient is always positive as long as $\phi_{\max} > 3/8$ (which is more than reasonable). Finally, using $f_h \sim c_m(1-\phi_{\max})(\phi_{\max} - \phi)^2$, the gravity flux is easily checked to be

$$g_{grav} \sim \frac{2\beta}{9} \frac{c_m (1-\phi_{\max})(K+1)^2}{2K+1} \epsilon^2.$$

For the difference $g - \phi f$ it is most straightforward to compute (with $\phi = \phi_{\max} - \epsilon$)

$$g_0 - \phi f_0 = \int_0^1 (\phi - \phi) u \, \mathrm{d}s \sim \epsilon^3 \frac{c_m \rho_m (K+1)^2}{2K+2} \int_0^1 (1 - (K+1)(1-s)^K)(1 - (1-s)^{2K+2}) \, \mathrm{d}s$$

which gives $b_0 = \frac{c_m \rho_m K(K+1)}{3(2K+3)}$. The others are similar; $b_1 = b_0/\rho_m$ is immediate. For b_3, compute

$$\int_0^1 (1-(K+1)(1-s)^K)(1-(1-s)^{3K+3})\,\mathrm{d}s = \frac{3K}{4(3K+4)}$$

to obtain $b_3 = \beta c_m \frac{K(K+1)}{4(K+2)(3K+4)}$. Lastly, by the definition of f_2 and the results computed for I_1, I_2 and I_3,

$$b_2 = (1+\beta\phi_m)b_1 - \phi_{\max} b_3.$$

Packed limit (SBM)

In this case, $A(\phi_{\max} - \epsilon) = A_m + O(\epsilon)$ as $\epsilon \to 0$ with $A_m = K_n/K_s$, which suggests using the expansion from the settled case instead and extending ϕ via $\phi \equiv \phi_{\max}$ (this is evident in the profiles shown in Figure 6.1b). The leading order equations, with $\epsilon^{1/2} S = s$ and

$$\phi \sim \phi_{\max} - \epsilon^{1/2}\phi_1 - \cdots, \quad \sigma \sim \rho_m(1-s) + \epsilon\sigma_1 + \cdots,$$

are given in the region where $S = O(1)$ by

$$\frac{\mathrm{d}\sigma_1}{\mathrm{d}S} = -\beta\phi_1$$
$$\frac{\mathrm{d}\phi_1}{\mathrm{d}S} = -K$$

where $K = M(\phi_{\max})/(\rho_m A_m)$ where $\rho_m = 1 + \beta\phi_m$. The solution is

$$\sigma_0 = \rho_m(1-s) + O(\epsilon), \quad \phi = \phi_{\max} - K(T-s)_+ + O(\epsilon^{1/2})$$

with $T = \sqrt{2\epsilon/K}$. Now to compute the velocity:

$$u(s) \sim \epsilon c_m \rho_m \int_0^s K^2 (T-\tau)_+^2\,\mathrm{d}\tau = \epsilon c_m \rho_m \frac{K^2}{3}(T^3 - (T-s)_+^3)$$

and finally

$$f_0(\phi_{\max} - \epsilon) = \int_0^1 u(s)\,\mathrm{d}s = \epsilon^{5/2} K^{1/2} \frac{2^{3/2} c_m (1+\beta\phi_m)}{3} + O(\epsilon^3)$$

along with

$$g_0 - \phi f_0 = \int_0^1 (\phi - \phi) u\,\mathrm{d}s = \epsilon^2 c_m \rho_m \frac{K^2}{3} \int_0^1 (1 - K(T-s)_+)(T^3 - (T-s)_+^3)\,\mathrm{d}s$$

so $f_0 \sim a_0 \epsilon^{5/2}$ and $g_0 - \phi f_0 \sim a_0 \epsilon^{7/2}$. The remainder of the integrals can be (tediously) computed in the same way; the exact values are not important and are not calculated here.

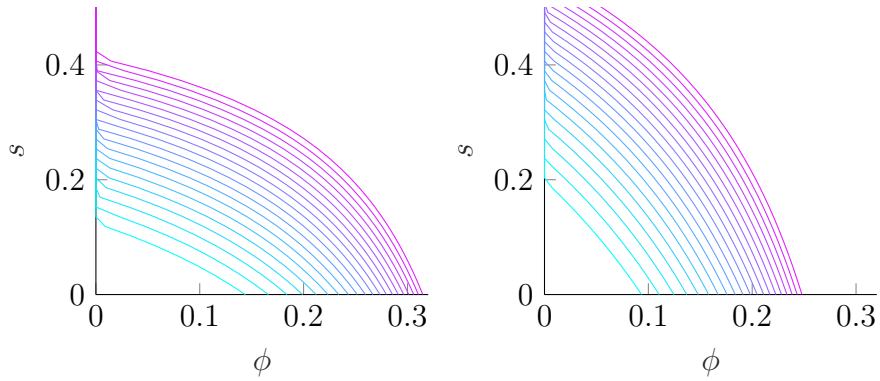

(a) Solutions $\phi(s)$ for DFM/SBM (left/right) as $\phi \to 0$.

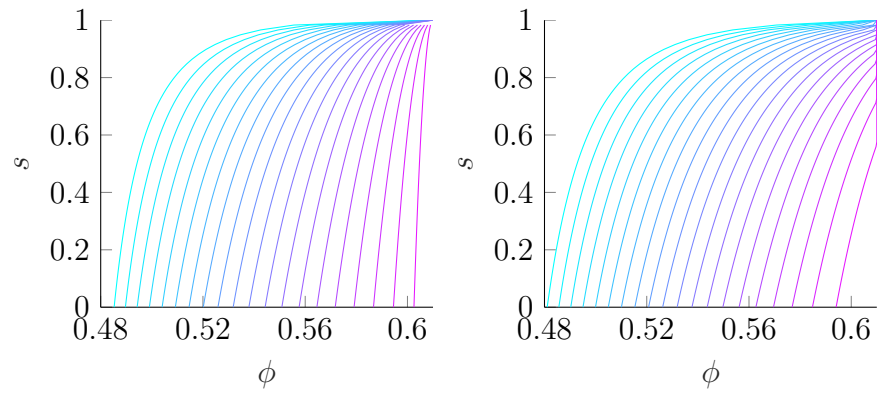

(b) Solutions $\phi(s)$ for DFM/SBM (left/right) as $\phi \to \phi_{\max}$.

Figure 6.1: Equilibrium profiles at $\alpha = 30\,\text{deg}$ in the dilute and large-phi limits for the diffusive flux and suspension balance models (ϕ ranges from 0.01 to 0.09 in the dilute and 0.5 to 0.605 in the packed limit, both from blue to purple).

6.2 Fluxes at the critical concentration

Since the solution is constant when $\phi = \phi_c$, the fluxes and their derivatives have a relatively simple form. This expansion is used in considering the constant volume problem in Chapter 5. Set $v = \phi_\phi$ and $w = \sigma_\phi$ (subscript indicating derivative); assuming smoothness of solutions and differentiating the ODE (2.14) yields

$$v' = -\frac{w}{\sigma^2}\frac{M(\phi_c)}{A(\phi_c)} + \frac{v}{\sigma}\frac{AM' - MA'}{A^2}\bigg|_{\phi_c}$$

$$w' = -\beta v$$

with $\int_0^1 v\,\mathrm{d}s = 1$ and $w(0) = \beta$. When $\phi = \phi_c$ we have $\phi \equiv \phi_c$ and $M(\phi) = 0$ so the above greatly simplifies and has an explicit solution

$$v = (1-K)(1-s)^{-K}, \qquad K := \frac{M'(\phi_c)}{A(\phi_c)(1+\beta\phi_c)}$$

and $w = \beta(1-s)^{K+1}$, valid so long as $0 < K < 1$. From this we can compute (at $\phi = \phi_c$)

$$(\phi f - g)' = \frac{\mathrm{d}}{\mathrm{d}\phi}\int_0^1 (\phi - \phi)u\,\mathrm{d}s = \int_0^1 (1-v)u\,\mathrm{d}s.$$

The velocity profile is simply $u = \frac{1+\beta\phi_c}{2\mu(\phi_c)}(1-(1-s)^2)$, so

$$\begin{aligned}(\phi f - g)'\Big|_{\phi=\phi_c} &= \frac{1+\beta\phi_c}{2\mu(\phi_c)}\int_0^1 (1-(1-K)(1-s)^{-K})(1-(1-s)^2)\,\mathrm{d}s \\ &= -\frac{1+\beta\phi_c}{\mu(\phi_c)}\frac{K}{3(3-K)}. \end{aligned} \tag{6.5}$$

As expected, this value is negative. The other derivatives, f', g' and so on could also be computed but will not be used. Also observe that

$$f(\phi_c) = \frac{(1+\beta\phi_c)}{3\mu(\phi_c)}, \qquad g(\phi_c) = \phi_c f(\phi_c).$$

6.3 Suspension balance with surface tension

For completeness, the thin-film PDEs for the surface tension model are derived here for the suspension balance model (SBM), analogous to the equations derived in Section 3.1.1. The derivation is similar but with the additional normal stress term, and the resulting equations have the same structure. The setup is exactly the same as for the SBM without surface tension derived in Section 2.2, except that we include surface tension in the surface stress boundary condition. To leading order the normal stress balance for Σ at the surface is then

$$p - \hat{\Sigma}_N^{zz} = p_a + \gamma\kappa \text{ at } z = h$$

since the normal components of the fluid part of Σ are small relative to Σ_N^{zz} (which scales with the largest shear component). Here $\kappa \approx h_{xx}$ is the (leading order) mean curvature. Eq. (2.9) yields the pressure

$$\hat{p} = \hat{\Sigma}_N^{zz} + \epsilon^2 \mathrm{Ca}^{-1}\hat{\kappa} + \cot\alpha \int_z^h \hat{\rho}\,\mathrm{d}z'. \tag{6.6}$$

where $\hat{\kappa} = (\epsilon/L)\kappa$ (the appropriate thin film scaling). However, the fluid equation (2.11) gives a simpler form for the pressure in equilibrium:

$$\hat{p} = \epsilon^2 \mathrm{Ca}^{-1}\hat{\kappa} + \cot\alpha(h - z). \tag{6.7}$$

Using this in the momentum equation, we get

$$(\mu_s u_{\hat{z}})_{\hat{z}} = \hat{\gamma}_s \kappa_{\hat{x}} + \epsilon \cot\alpha h_{\hat{x}} - \epsilon \partial_{\hat{x}} \hat{\Sigma}_N^{xx} - \hat{\rho} \tag{6.8}$$

to leading order. From the equilibrium equation (2.12b) we get

$$\partial_{\hat{x}} \hat{\Sigma}_N^{xx} = \lambda_1 \partial_{\hat{x}}(\mu_n(\phi)\dot{\gamma}) = -\frac{\lambda_1 \rho_s}{\lambda_2} \cot\alpha \frac{\partial}{\partial x}\left(\int_z^h \phi \,\mathrm{d}z'\right)$$

which reduces (6.8) to terms that are familiar from the DFM (section 1.3). The rest of the derivation is then standard, yielding

$$u = h^2 \tilde{I}_0 + (\hat{\gamma}_s \kappa_{\hat{x}}) h^2 \tilde{I}_1 - \epsilon \cot\alpha \left[h^2 h_x \left(\tilde{I}_1 + \frac{\lambda_1}{\lambda_2}\tilde{I}_2\right) + \lambda_1 h^3 \phi_{\hat{x}} \tilde{I}_3\right].$$

The fluxes are as before in (3.7) except for $i = 2$, where instead

$$f_2 = \int_0^1 \tilde{I}_1 + \frac{\lambda_1}{\lambda_2}\tilde{I}_2 \,\mathrm{d}s - \phi \tilde{I}_3$$

and similarly for g_2.

The conservation equations are slightly different (but the same to leading order). From incompressibility of the suspension (Eq. (2.1) in the general model) and the kinematic condition,

$$\frac{\partial h}{\partial t} + \frac{\partial}{\partial x}\left(\int_0^h u \,\mathrm{d}z\right) = 0.$$

From the particle transport equation (2.3) and the kinematic condition,

$$\frac{\partial}{\partial t}(h\phi) + \frac{\partial}{\partial x}\left(\int_0^h \phi u \,\mathrm{d}z\right) = -\frac{\partial}{\partial x}\left(\int_0^h J^{(x)} \,\mathrm{d}z\right)$$

which differs from the DFM because the suspension is exactly incompressible here. One then obtains the conservation PDEs in the same way as before. It is interesting to note, however, that the second order diffusion terms in the resulting PDE system (3.8) can be interpreted as migration due to normal stresses from the particle phase, i.e. the $\partial_{\hat{x}} \hat{\Sigma}_N^{xx}$ terms, which are the key mechanism for particle migration in the suspension balance model [NB94].

Remark 6.1. *The gravity term at $O(a^2/H^2)$ is also somewhat different; it is now present in the particle but not suspension equation. From* (2.10)*, we find that, to leading order,*

$$\frac{\partial}{\partial t}(h\phi) + \frac{\partial}{\partial x}\left(\int_0^h \left(\phi u + \frac{2a^2}{9H^2} f_h(\phi)(u_{zz}+1)\right) \mathrm{d}z\right) = 0.$$

Once scaled, the result is (omitting the higher order terms)

$$\frac{\partial}{\partial t}(h\phi) + \frac{\partial}{\partial x}\left(h^3 g_0 + \frac{a^2}{H^2} h g_{grav}\right) = 0$$

for $g_{grav} = \frac{2}{9}\int_0^1 f_h(\widetilde{\varphi})(\tilde{u}_{ss}+1)\,\mathrm{d}s$.

In two dimensions

Under the simplifying assumption that the flow is primarily in the $\hat{x}$ direction, the flow-aligned tensor $\mathbf{Q}$ is in coordinates $(\hat{x}, \hat{z}, \hat{y})$. In this case the derivation for the 2d equations is the same in the $\hat{x}$ direction and differs in the $\hat{y}$ direction only by replacing λ_2 with λ_3 (which accounts for the anisotropy in the shear-induced migration effect since $\lambda_2 > \lambda_3$). In this case the resulting PDEs are almost the same as (3.13). Define $a = \frac{\lambda_1}{\lambda_3} - \frac{\lambda_1}{\lambda_2}$. Then

$$h_t + (h^3 f_0)_x = -\hat{\gamma}_s \nabla \cdot (h^3 f_1 \nabla\nabla^2 h) + \epsilon \cot\alpha \left[\nabla \cdot \left(h^3(f_2 \nabla h + f_3 \nabla\psi)\right) + a(h^3 f_4 h_y)_y\right] \quad (6.9a)$$

$$\psi_t + (h^3 g_0)_x = -\hat{\gamma}_s \nabla \cdot (h^3 g_1 \nabla\nabla^2 h) + \epsilon \cot\alpha \left[\nabla \cdot \left(h^3(g_2 \nabla h + g_3 \nabla\psi)\right) + a(h^3 g_4 h_y)_y\right] \quad (6.9b)$$

where (with a regrettable choice of indexing) $f_4 = \int_0^1 \tilde{I}_2\,\mathrm{d}s$. In reality, if the $x-$ and $y-$ velocities u, v have comparable magnitudes then $\mathbf{Q}$ will no longer be aligned with the coordinate system, in which case the anisotropy requires more work to handle correctly; the two directions are now coupled together. However, we do not pursue this extension here.

6.4 Dilute limit with $p_x \approx 1$

Here we fill in the details for the calculation of the dilute particle flux when the added (non-dimensional) pressure gradient $p_x \approx 1$ from Section 3.2.1. Given the approximate solution

(3.17) with $|p - \phi_c| = O(\delta)$ and T, T_0 given by (3.18), the shear stress, velocity and the flux G can be computed under the simplifying assumption that

$$\mu = \begin{cases} \mu(\phi_c) & s < S_0 \\ 1 & s > S_0 \end{cases} \tag{6.10}$$

to leading order. For the shear stress,

$$\sigma = \sigma_a + \sigma_b$$

where

$$\sigma_a = \delta(s-1), \qquad \sigma_b(s) = \begin{cases} \rho_s(\phi_0 - \phi_c s) & s < S_0 \\ \frac{B}{2|\delta|}(S-s)^2 & S_0 < s < S \\ 0 & S < s. \end{cases} \tag{6.11}$$

First compute

$$u_a(s') = \int_0^{s'} \mu^{-1}\sigma_a \,\mathrm{d}s = \begin{cases} \frac{\delta}{2\mu_c}((s'-1)^2 - 1) & s' < S_0 \\ u_a(S_0) + \delta \int_{S_0}^{s'} (s-1)\,\mathrm{d}s & s' > S_0 \end{cases}.$$

Multiplying by ϕ and integrating from 0 to 1:

$$G_a = \int_0^{S_0} \phi_c u_a(s)\,\mathrm{d}s + \frac{B}{|\delta|}\int_{S_0}^{S} (S-s)u_a(s)\,\mathrm{d}s \tag{6.12}$$

$$= \frac{\phi_c \delta}{2\mu_c}\int_0^{S_0} ((s-1)^2 - 1)\,\mathrm{d}s + \frac{B\phi_c|\delta|}{2}u_a(S_0) + \frac{B\delta}{2|\delta|}\int_{S_0}^{S}(S-s)((S_0-1)^2 - (s-1)^2)\,\mathrm{d}s \tag{6.13}$$

$$= -\frac{\phi_c}{2\mu_c}\delta S_0^2 + O(\delta S_0^3) - \frac{B\phi_c|\delta|\delta}{2\mu_c}S_0 + O(\delta^2\phi_0^2) - \frac{B(S_0+1)\delta}{6|\delta|}(S-S_0)^3 + O(\delta^4) \tag{6.14}$$

$$= -\frac{\phi_c}{2\mu_c}\delta S_0^2 - \frac{B\phi_c}{2\mu_c}\delta|\delta|S_0 - \frac{\phi_c^3}{6B^2}\delta|\delta|^2 + O((\phi_0 + |\delta|)^4) \tag{6.15}$$

The higher order terms are $\phi_0^k|\delta|^\ell$ with $k + \ell \geq 4$. For the σ_b part,

$$G_b = \int_0^{S_0} \phi_c u_b \,\mathrm{d}s + \int_{S_0}^{S} \phi u_b \,\mathrm{d}s.$$

Evaluating the two contributions separately:

$$\text{1st term}: \quad \int_0^{S_0} \phi_c \int_0^{s'} \mu_c^{-1} \rho_s (\phi_0 - \phi_c s)\, \mathrm{d}s\, \mathrm{d}s' = \frac{\rho_s \phi_c}{2\mu_c} \left(\phi_0 S_0^2 - \phi_c S_0^3/3 \right)$$

$$\begin{aligned} \text{2nd term:} \quad \int_{S_0}^{S} \phi u_b \, \mathrm{d}s &= \int_{S_0}^{S} \frac{B}{2|\delta|}(S - s') \left(u_b(S_0) + \int_{S_0}^{s'} \frac{B}{2|\delta|}(S-s)^3 \, \mathrm{d}s \right) \mathrm{d}s' \\ &= \frac{B}{4|\delta|\mu_c}(\phi_0 S_0 - \phi_c S_0^2/2)(S - S_0)^2 + \frac{B^2}{40|\delta|^2}(S - S_0)^5. \end{aligned}$$

Adding everything together (note that $S, S_0 \sim \phi_0$ and $S - S_0 \sim |\delta|$), we find that

$$G = \sum_{k+\ell=3} C_{k,\ell} \phi_0^k |\delta|^\ell + K_2 \delta \phi_0 |\delta| + O((\phi_0 + |\delta|)^4), \qquad \delta \to 0^- \tag{6.16}$$

for certain constants that can be found explicitly.

References

[Arn16] David Arnold. *Thin-film flow in helical channels.* PhD thesis, University of Adelaide, 2016.

[ASG17] D. J. Arnold, Y. M. Stokes, and J. E. F. Green. "Thin-film flow in helically wound shallow channels of arbitrary cross-sectional shape." *Physics of Fluids*, **29**(1):013102, 2017.

[BB97] Andrea L. Bertozzi and Michael P. Brenner. "Linear stability and transient growth in driven contact lines." *Physics of Fluids (1994-present)*, **9**(3):530–539, 1997.

[BF90] Francisco Bernis and Avner Friedman. "Higher order nonlinear degenerate parabolic equations." *Journal of Differential Equations*, **83**(1):179–206, 1990.

[BJL11] A. L. Bertozzi, N. Ju, and H. Lu. "A biharmonic-modified forward time stepping for fourth order nonlinear diffusion equation." *Discrete and Continuous Dynamical Systems*, **29**:1367–1391, 2011.

[BKK15] S. Burnett, J. Kreger, H. Kristensen, and A. Stocker. "Dynamics of particle-Laden thin films: viscous fluid on an incline." `ftp://ftp.math.ucla.edu/pub/camreport/cam15-70.pdf`, 2015.

[BPG11] François Boyer, Olivier Pouliquen, and Élisabeth Guazzelli. "Dense suspensions in rotating-rod flows: normal stresses and particle migration." *Journal of Fluid Mechanics*, **686**:5–25, 2011.

[CAB09] Benjamin Cook, Oleg Alexandrov, and Andrea Bertozzi. "Linear stability of particle-laden thin films." *The European Physical Journal-Special Topics*, **166**(1):77–81, 2009.

[CBH08] B. P. Cook, A. L. Bertozzi, and A.E Hosoi. "Shock Solutions for Particle-Laden Thin Films." *SIAM J. Appl. Math.*, **68**(3):760–783, 2008.

[CM09] R.V. Craster and O.K. Matar. "Dynamics and stability of thin liquid films." *Reviews of modern physics*, **81**(3):1131, 2009.

[Coo08] B. P. Cook. "Theory for particle settling and shear-induced migration in thin-film liquid flow." *Phys. Rev. E.*, **78**:045303, 2008.

[Ein06] Albert Einstein. "Calculation of the viscosity-coefficient of a liquid in which a large number of small spheres are suspended in irregular distribution." *Ann. Phys. Leipzig*, **19**:286–306, 1906.

[Fow90] Christine Mary Rutherford Fowler. *The solid earth: an introduction to global geophysics.* Cambridge University Press, 1990.

[Hup82] Herbert E. Huppert. "Flow and instability of a viscous current down a slope." *Nature*, **300**(5891):427–429, 1982.

[KBL96] Gokul P. Krishnan, Shannon Beimfohr, and David T Leighton. "Shear-induced radial segregation in bidisperse suspensions." *Journal of Fluid Mechanics*, **321**:371–393, 1996.

[KG12] Amit Kumar and Michael D. Graham. "Mechanism of margination in confined flows of blood and other multicomponent suspensions." *Physical Review Letters*, **109**(10):108102, 2012.

[KK90] Herbert C. Kranzer and Barbara Lee Keyfitz. *A strictly hyperbolic system of conservation laws admitting singular shocks*. Springer, 1990.

[LA87] D. Leighton and A. Acrivos. "Shear-induced migration of particles in concentrated suspensions." *Journal of Fluid Mechanics*, **181**:415, 1987.

[Lax73] Peter D. Lax. *Hyperbolic systems of conservation laws and the mathematical theory of shock waves*, volume 11. SIAM, 1973.

[LMU14] Sungyon Lee, Aliki Mavromoustaki, Gilberto Urdaneta, Kaiwen Huang, and Andrea L Bertozzi. "Experimental investigation of bidensity slurries on an incline." *Granular Matter*, **16**(2):269–274, 2014.

[LSB14] Sungyon Lee, Yvonne Stokes, and Andrea L Bertozzi. "Behavior of a particle-laden flow in a spiral channel." *Physics of Fluids*, **26**(4):043302, 2014.

[LWB15] Sungyon Lee, Jeffrey Wong, and Andrea L. Bertozzi. "Equilibrium theory of bidensity particle-laden flows on an incline." In *Mathematical Modelling and Numerical Simulation of Oil Pollution Problems*, pp. 85–97. Springer, 2015.

[MB99] Jeffrey F. Morris and Fabienne Boulay. "Curvilinear flows of noncolloidal suspensions: The role of normal stresses." *Journal of Rheology (1978-present)*, **43**(5):1213–1237, 1999.

[MB11] Matthew R. Mata and Andrea L. Bertozzi. "A Numerical Scheme for Particle-Laden Thin Film Flow in two dimensions." *J. Comp. Phys.*, **230**(16):6334–6353, 2011.

[MB14] A. Mavromoustaki and A. L. Bertozzi. "Hyperbolic systems of conservation laws in gravity-driven, particle-laden thin-film flows." *Journal of Engineering Mathematics*, **88**(1):29–48, 2014.

[MHH11] N. Murisic, J. Ho, V. Hu, P. Latterman, T. Koch, K. Lin, M. Mata, and A. L. Bertozzi. "Particle-laden viscous thin-film flows on an incline: experiments compared with an equilibrium theory based on shear-induced migration and particle settling." *Physica D*, **240**(20):1661–1673, 2011.

[MLB14] Matthew Molinaire, Andrew Li, Sarah Burnett, and Katherine Varela. "Gravity driven particle-laden flow." `ftp://ftp.math.ucla.edu/pub/camreport/cam15-11.pdf`, 08 2014.

[MM06] Ryan M. Miller and Jeffrey F. Morris. "Normal stress-driven migration and axial development in pressure-driven flow of concentrated suspensions." *Journal of non-newtonian fluid mechanics*, **135**(2):149–165, 2006.

[MPP13] Nebojsa Murisic, Benoit Pausader, Dirk Peschka, and Andrea L Bertozzi. "Dynamics of particle settling and resuspension in viscous liquid films." *Journal of Fluid Mechanics*, **717**:203–231, 2013.

[MWW16] Aliki Mavromoustaki, Li Wang, Jeffrey T. Wong, and A. L. Bertozzi. "Modeling and simulation of particle-laden flow with surface tension." (submitted to Nonlinearity), 2016.

[NB94] Prabhu R. Nott and John F. Brady. "Pressure-driven flow of suspensions: simulation and theory." *Journal of Fluid Mechanics*, **275**:157–199, 1994.

[NGP11] Prabhu R. Nott, Elisabeth Guazzelli, and Olivier Pouliquen. "The suspension balance model revisited." *Physics of Fluids (1994-present)*, **23**(4):043304, 2011.

[PAB92] Ronald J. Phillips, Robert C. Armstrong, Robert A. Brown, Alan L. Graham, and James R. Abbott. "A constitutive equation for concentrated suspensions that accounts for shear-induced particle migration." *Physics of Fluids A: Fluid Dynamics*, **4**(1):30–40, 1992.

[RH92] J. M. Revay and J. L. Higdon. "Numerical simulation of polydisperse sedimentation: equal-sized spheres." *Journal of Fluid Mechanics*, **243**:15–32, 1992.

[RL08] Arun Ramachandran and David T. Leighton. "The influence of secondary flows induced by normal stress differences on the shear-induced migration of particles in concentrated suspensions." *Journal of Fluid Mechanics*, **603**:207–243, 2008.

[TA99] Anubhav Tripathi and Andreas Acrivos. "Viscous resuspension in a bidensity suspension." *International journal of multiphase flow*, **25**(1):1–14, 1999.

[WB03] Thomas P. Witelski and Mark Bowen. "ADI schemes for higher-order nonlinear diffusion equations." *Applied Numerical Mathematics*, **45**(2):331–351, 2003.

[WB14] Li Wang and Andrea L. Bertozzi. "Shock solutions for high concentration particle-laden thin films." *SIAM Journal on Applied Mathematics*, **74**(2):322–344, 2014.

[WB16] Jeffrey T. Wong and Andrea L. Bertozzi. "A conservation law model for bidensity suspensions on an incline." *Physica D: Nonlinear Phenomena*, **330**:47–57, 2016.

[WMB15] Li Wang, A. Mavromoustaki, A. L. Bertozzi, G. Urdaneta, and K. Huang. "Rarefaction-singular shock dynamics for conserved volume gravity driven particle-laden thin film." *Physics of Fluids (1994-present)*, **27**(3):033301, 2015.

[WWG09] Thomas Ward, Chi Wey, Robert Glidden, AE Hosoi, and AL Bertozzi. "Experimental study of gravitation effects in the flow of a particle-laden thin film on an inclined plane." *Physics of Fluids*, **21**(8):083305, 2009.

[XKL16] Feng Xu, Jungchul Kim, and Sungyon Lee. "Particle-induced viscous fingering." *Journal of Non-Newtonian Fluid Mechanics*, **238**:92–99, 2016.

[ZDB05] Junjie Zhou, B Dupuy, A. L. Bertozzi, and A. E. Hosoi. "Theory for shock dynamics in particle-laden thin films." *Physical Review Letters*, **94**(11):117–803, 2005.